SEISMOLOGICAL CONSTRAINTS ON THE MECHANICS OF INTERMEDIATE-DEPTH EARTHQUAKES IN THE BUCARAMANGA NEST

A DISSERTATION
SUBMITTED TO THE DEPARTMENT OF GEOPHYSICS
AND THE COMMITTEE ON GRADUATE STUDIES
OF STANFORD UNIVERSITY
IN PARTIAL FULFILLMENT OF THE REQUIREMENTS
FOR THE DEGREE OF
DOCTOR OF PHILOSOPHY

Sarah Anne Barrett

August 2015

I certify that I have read this dissertation and that, in my opinion, it is fully adequate in scope and quality as a dissertation for the degree of Doctor of Philosophy.

Gregory Beroza, Primary Adviser

I certify that I have read this dissertation and that, in my opinion, it is fully adequate in scope and quality as a dissertation for the degree of Doctor of Philosophy.

Jesse Lawrence

I certify that I have read this dissertation and that, in my opinion, it is fully adequate in scope and quality as a dissertation for the degree of Doctor of Philosophy.

Jessica Warren

Approved for the Stanford University Committee on Graduate Studies.

Patricia J. Gumport, Vice Provost for Graduate Education

This signature page was generated electronically upon submission of this dissertation in electronic format. An original signed hard copy of the signature page is on file in University Archives.

Preface

For all the progress that seismology has made in the last century, intermediate-depth earthquakes are a relatively poorly understood phenomenon. They occur at depths 50-300 km, where high temperatures and pressures prohibit traditional brittle shear failure. Intermediate-depth earthquakes frequently occur in concentrated regions of seismicity called "earthquake nests". One such nest, the Bucaramanga Nest, beneath northern Colombia, is the focus of this work. It is the smallest and densest cluster of intermediate-depth seismicity in the world. This clustered region of seismicity produces thousands of events each year. While the nest does not pose the hazard other intermediate-depth earthquake nests might (e.g. the Vrancea Nest, Romania), the nest is capable of producing moderate shaking such as in the M 6.2 event that occurred in the nest in early 2015. This high level of seismicity provides an opportunity to study characteristics of the nest and its earthquakes as a natural laboratory.

This dissertation utilizes the tools of observational seismology to expand on processes of intermediate-depth seismicity with particular emphasis on constraining the underlying failure mechanism. To maximize the observations of nest seismicity, I develop a new and novel earthquake detection method that bridges the gap between general and specific earthquake detection algorithms. Through observations of these events, I find repeating and reverse-polarity repeating signals and explain how the timing and relative locations of these earthquakes are indicative of subduction

processes at intermediate-depths. I am also able to perform a comprehensive search for small magnitude earthquakes and find the Bucaramanga Nest deviates from traditional Gutenberg-Richter magnitude-frequency distributions at the small end magnitude of the magnitude spectrum. I find multiple lines of evidence that support a thermal shear instability failure mechanism for these intermediate-depth nest earthquakes.

Acknowledgments

I am extremely fortunate to be able to work on this dissertation with my advisor, Greg Beroza. Under his mentorship, I developed the skills necessary to be an independent scientist. Over the years I valued the freedom Greg gives me, to “just give it a try” or to talk through a crazy plot of seemingly meaningless parameters, that turns out to be something interesting. His ability to foster both creativity and meaningful scientific contributions is truly a gift.

Germán Prieto is like a second advisor to me. Throughout the years he provided data, feedback and the opportunity to visit Colombia and learn from the scientists who produce the data used in this thesis. His ability to make large problems feel accomplishable made an overwhelming task feel manageable.

My reading committee worked with me every step of the way. Jesse Lawrence and Jessica Warren were always available to help me see how my contributions fit into the larger scope of geophysics and geology. Their feedback and support is invaluable. Jesse has especially been nurturing of my development as a seismologist; from supervising my second project, to allowing me to join a seismic field team in the Atacama, I thank him for helping me develop applied geophysical skills.

The Servicio Geológico Colombiano (CGS) Working Group at the Colombian Seismic Network and Germán Prieto generously provided the data from the Bucaramanga Nest

and Colombian seismic network. Patricia Pedraza was particularly helpful in providing data and details about network operations.

Much of this thesis was completed through the use of generously shared, freely available software. Specific contributions are noted throughout the text of this dissertation. Maps were made using the Generic Mapping Tools (GMT). Data for the Big Bear sequence in Chapter 2 was acquired using the Standing Order for Data (SOD), downloaded from the IRIS Data Management Center (DMC). Seismograms throughout this work were processed using the Seismic Analysis Code (SAC). Relocations of earthquakes in Chapter 3 were performed using HYPODD. Several schematics and cartoons were modified or inspired by icons designed by freepik and made available through the Creative Commons license.

For two years I was generously supported by a fellowship from the Achievement Rewards for College Scientists. This organization truly stands behind the students they fund. I have always felt like the representatives from the Kimball Foundation are some of my biggest cheerleaders. The Bucaramanga Nest research is supported by NSF grant EAR-1045684.

The Beroza group during my time at Stanford taught me more than I can put in print. Their constant quest to be the best seismologists they can be, in all aspects, has help shape me into the scientist I am today. It is an honor to be colleagues and peers with this group of scientists; I know they will be both contacts and friends for life. I am especially fortunate to have learned so much from Marine Denolle, Cyndi Kelly and Clara Yoon while we shared an office. I cannot image a stronger (or more fun) group of scientists to debug codes or bounce ideas with.

While at Stanford, I have been surrounded by so many wonderful friends. The graduate student community here is truly special. Kelcie, Randi, Beth, Cyndi and Meredith made my time here a little brighter. Their friendship brought so much joy

into my life. I'm lucky to have them (literally) running through life beside me. So many members of the Geophysics department put a smile on my face over the years. My cohort is especially stellar; they are always able to take my mind off the seriousness of life and remind me to live a little. A big thanks to all involved with our football tailgates, those Saturdays were certainly some of my favorite days at Stanford.

The love, patience and support I received from Brian are more than I deserve. His confidence in me always exceeds the confidence I have in myself. I feel blessed to have a companion who continues to see the best in me, help me to exceed my own potential, and to realize this is just the beginning… the adventure continues …

Finally, I have to thank my family for encouraging and believing in me, and to help me push the boundaries of what I think is possible. I would not be here without your guidance and nurturing spirit. I never imagined all this could happen to me, but your support and faith made it so.

Contents

List of Tables

List of Figures

CHAPTER ONE:

Introduction

The Characteristics of Intermediate-Depth Earthquakes

While much is understood about the failure mechanism and parameters of shallow seismicity, intermediate-depth and deep earthquakes are less well understood. This population of earthquakes accounts for nearly 25% of the global seismic catalog (Frohlich 2006, Figure 1-1). Traditionally these earthquakes are known to be less damaging than their shallow counterparts; however, some intermediate-depth earthquakes in the last 100 years have proved very damaging causing the destruction of cities and loss of many lives. The 1977 Romania and 1939 Chile earthquakes both caused substantial damage and loss of life. The problem of how these earthquakes occur remains largely unanswered. These earthquakes occur at temperatures and pressures, which do not support the hypothesis of traditional brittle failure, thus another failure mechanism must be employed. The spatial distribution of intermediate-depth earthquakes is especially curious. In addition to illuminating Wadoti-Benioff zones, earthquakes at depths 60-300 km sometimes form dense clusters of seismic activity, or "earthquake nests". Unlike the case of shallow earthquakes, there is not a framework by which these events occur in space or recur in time. This chapter will review the current understanding of intermediate-depth earthquakes, especially those that occur in the Bucaramanga earthquake nest, and pose questions about less well-understood topics.

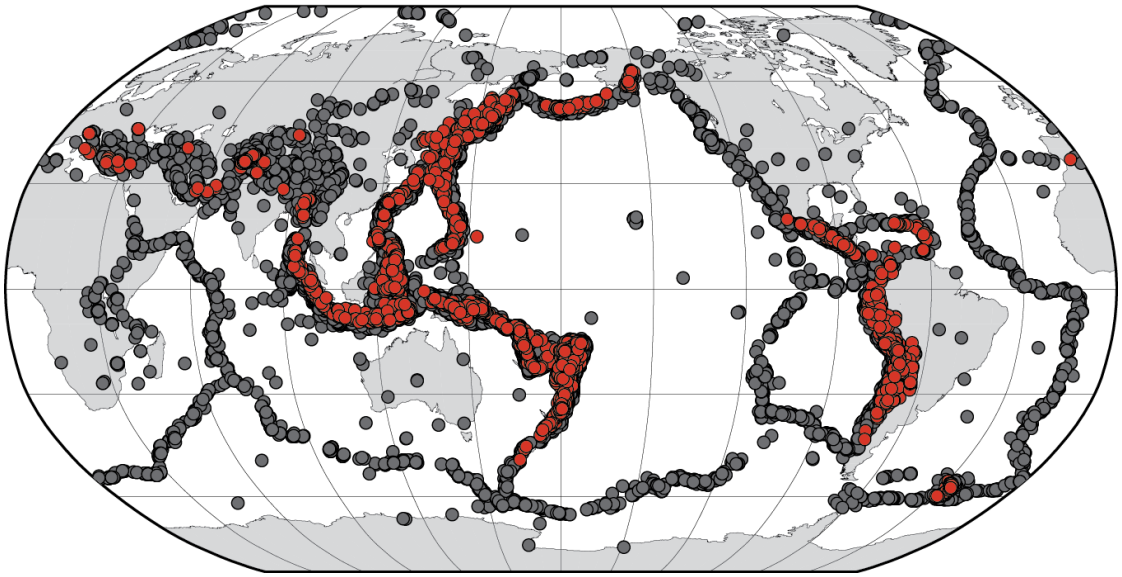

Figure 1-1. Global seismicity from the NEIC for events M > 5 for one year (2014). Intermediate-depth earthquakes (depths 60-300km) are highlighted in red.

The Destructive Nature of Intermediate-Depth Earthquakes

Earthquakes that occur at intermediate-depths do not excite damaging surface waves. In addition, their hypocentral distance from the surface means that energy is not concentrated near the epicenter to the extent as in shallow earthquake shaking due to geometric spreading. Nevertheless, a lack of strong waves at the surface does not limit the impact of large magnitude events, especially in regions of poor building construction. The 1939 M_S 7.8 Chillan earthquake is estimated to have a focal-depth of up to 100 km (Beck et al., 1998). Nearly 97% of structures in Chilean were damaged (del Canto et al., 1940), resulting in 25,000 deaths (Saita, 1940). A similarly sized and more recent intermediate-depth event was the 1977 M_W 7.5 Vrancea earthquake. This earthquake struck the city of Bucharest, killing more than 1500 and displacing 200,000 people (Fattal et al., 1977). Intermediate-depth earthquakes, while located farther from the surface still pose a substantial natural hazard.

An Unknown Model of Recurrence

Intermediate-depth earthquakes lack a consistent pattern in their behavior of aftershocks. Most have few, if any, events that can be considered aftershocks. Shallow

earthquakes typically follow an Omori-type aftershock decay (Omori, 1895), where the number of aftershocks decreases exponentially with time. It is also typical to observe an aftershock approximately 1.2 magnitude units less than the mainshock (Båth's law). In general, intermediate-depth earthquakes are deficient in developed aftershock sequences when compared to their shallow counterparts. Notable exceptions do exist, including the 1977 Vrancea event discussed previously (~140 aftershocks; Fuchs et al., 1979) and several of the Hindu-Kush Nest earthquakes (Pavlis and Hamburger, 1991). One aspect of these observations to consider is that intermediate and deep-focus earthquakes often occur in regions with sparse station spacing and a sampling bias of smaller magnitude (aftershocks) may exist.

It is probably that a sampling bias for large, potentially damaging intermediate-depth earthquakes also exists. The instrumental record of seismology is only ~120 years long and may not accurately describe the long-term potential of earthquakes at intermediate (and deep) depths. The spatial distribution of non-brittle earthquakes is not well understood. It is uncertain why intermediate and deep earthquakes occur in some places, but not others. Strange and curious examples such as the 1954 M 7.9 Spain deep earthquake (~630 km) remain enigmas. This sampling time period of just over a century might not be representative of seismic activity at these depths, especially when considering the failure mechanism of these events is uncertain.

Spatial Clustering: Earthquake Nests

Intermediate-depth seismicity often occurs in dense clusters of seismicity, or "nests". Charles Richter made reference to these tectonic features in his seminal textbook *Elementary Seismology*:

> *"An earthquake nest is a volume of intense seismic activity that isolated from nearby activity"*

We expand upon this definition further to limit our discussion of earthquake nests to exclude shallow events ($z < 60$ km) and those with volcanic association. The nest differs from a traditional seismic swarm by its prolonged release of seismic moment for decades and centuries. Under these criteria there are three loci of nest seismicity that are widely discussed in the literature: the Hindu-Kush Nest (Afghanistan), the Vrancea Nest (Romania) and the focus of this work, the Bucaramanga Nest (Colombia).

There are several slab or slab fragment configurations suggested by previous studies (Figure 1-2). A nest is proposed to be the termination of a slab (e.g. Corredor, 2003), a tear within a slab (e.g. Cortes & Angelier, 2005), or the result of slab contortion (e.g. Nowroozi, 1971). Scenarios with multiple slabs have also been suggested as a nest generation mechanism, including overlap between two slabs (e.g. van der Hilst & Mann, 1994) or the collision of two slabs (e.g. Zarifi et al., 2007). Some configurations, such as slab tears or contortions, might be a rather common process or feature in subducting slabs. These situations each require an intense concentration of strain, relative to other areas of the slab. This could suggest a failure mechanism with underlying strain-rate dependence. As the global seismic network grows and improves, more earthquake nests might be identified, pointing to one of these options as a likely situation. The three primary nests are discussed in terms of their tectonic setting, test geometry and seismic activity.

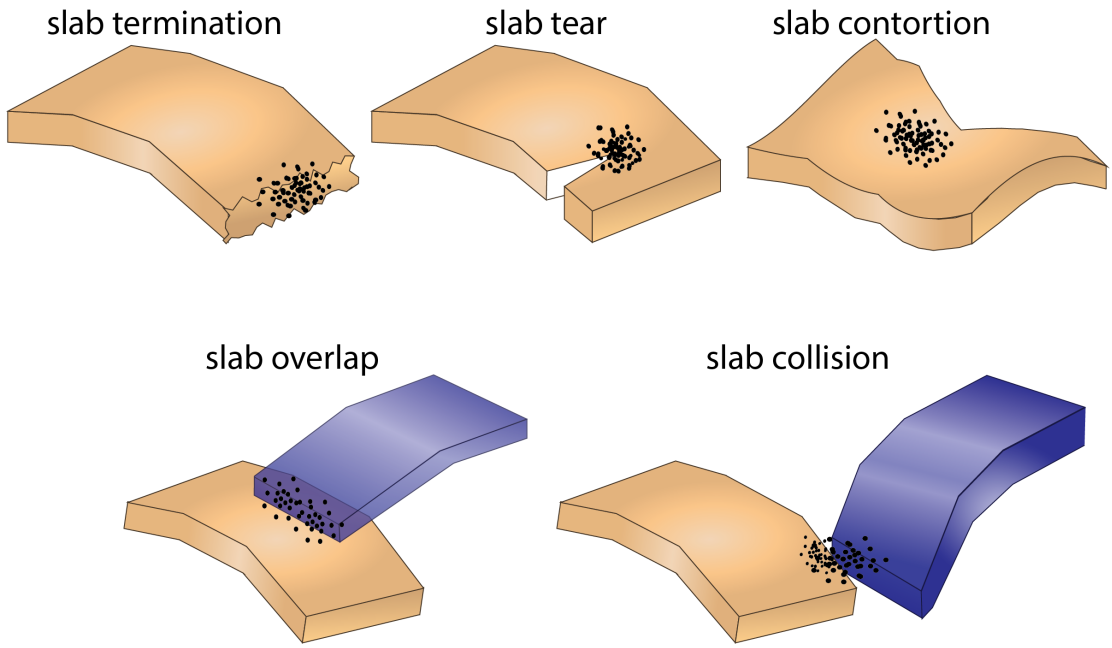

Figure 1-2. Illustrations of various tectonic situations hosting earthquake nests as suggested in the literature. Most require only one slab or slab fragment; however a few involve the interaction between more than one. Single slab scenarios include: the edge of a slab, a tear in the slab, and a complex stress field. The possibility of slab fragments interacting in the upper mantle is also suggested in situations where one slab overlaps the other or where they might collide.

The Hindu-Kush Nest, Afghanistan – 36.5°N 71°E – 30x75x120km

One region of prominent concentrated intermediate-depth seismicity is the Hindu-Kush Nest near the Afghanistan-Pakistan border. The tectonics of the region is dominated by the collision of the Indian plate with the Eurasian plate. In many tomographic studies (e.g. Chatelain et al., 1980; Fan et al., 1994) suggested there are two subducted slab fragments with opposing orientations in the area. A recent study combines tomography, seismicity and thermo-kinematic modeling and agrees with the two slab model, but suggests a collision between the two at ~130 km. Other works allow for the possibility of a two-slab solution, but focus on a single slab interpretation of the S-shaped seismicity (Billington et al., 1977). Lister et al. (2008) interpret this seismicity to be a product of slab break-off through ductile faulting and shear zones.

The S-shaped seismicity distribution is a signature of the Hindu-Kush Nest. Cross sections across the Pamir and Hindu Kush areas show regions of opposite dips (Prieto

et al., 2012). The northward dipping Hindu Kush region extends deeper (~250 km) than the south-southeast dipping Pamir region (~175 km). Most earthquakes in the Hindu-Kush Nest are reverse faulting-type mechanisms in a nearly vertical slab. By dimension, this is the largest of the well-documented, primary nests and is the most active with respect to total moment release. This nest produces more **M**>4 events than any other nest on Earth, including the largest event since 2000, as well as several **M**>7 events in the last century. There are an average of 2.2 $m_b > 4.8$ events per month, and more than 7000 events in the ISC catalog (Havskov and Zarifi, 2003).

One such M>7 event occurred in the nest on 3 March 2002. The M 7.4 earthquake occurred at a depth of ~225 km. It was widely felt throughout Pakistan and Afghanistan, responsible for approximately 150 deaths. The rupture is thought to be a composite event of two seismic releases separated by 75 ±5km and 8.5 ±2s (Kiser et al., 2011). Accounts of composite event style releases are observed in nests other than the Hindu Kush, including the Bucaramanga Nest and the Vrancea Nest and may be a common feature of nest seismicity in general.

The Vrancea Nest, Romania – 45.7°N 26.5°E – 20x50x110km

The Vrancea Nest is located beneath the Romanian Carpathian range and is associated with closing and subsequent subduction of the Tethys Ocean (Sperner et al., 2001). Active subduction in the region ceased in the North with the convergence of Eastern European lithosphere, which is substantially less dense than the ocean lithosphere, about 12-14 Ma (Jiricek, 1979). This cessation began in the northwest and progressed along the arc to the southeast. The Vrancea Nest is located on the southeastern-most edge of this arc and is the only region of the zone that is known to be seismically active.

The nest is nearly vertical, with seismicity extending from 70-180 km depth (Prieto et al., 2012). Earthquakes in the global CMT catalog are primarily reverse-faulting events within a nearly vertical slab. The nest has the highest contrast of seismicity, with nearly 900 times greater moment release within the nest, when compared to the

surrounding area (Zarifi and Havskov, 2003). This separation is used to invoke two interpretations of the tectonic setting using seismic tomography: slab break-off or delamination. Additionally, this seismicity is well separated from the shallow seismicity of the region (Sperner et al., 2001).

The slab break-off model proposes that slabs in the northern, inactive region have detached, while those in the south (Vrancea) are at least partially coupled to the lithosphere. This partial coupling and continued slab-pull allows for the intermediate-depth seismicity observed. In the north where the slab is thought to be completely detached there is no notable intermediate-depth seismicity. This is akin to the tectonic separation of the slab proposed in the Hindu Kush. Koulakov et al., 2010, describe the alternate situation of delamination. They propose the high velocity anomaly observed in tomography models is a mass of eclogite formed by the mafic upper crust. In this interpretation, the stress concentration of this negatively buoyant layer is thought to drive the Vrancea seismicity in this interpretation.

The most notable earthquake produced by this nest is the 4 March 1977 **M** 7.2 Vrancea earthquake. Early studies of the rupture process of this event suggested it was comprised of four composite events, one with reverse polarity to the other three (Müller et al., 1978). The four events show a roughly cascading pattern, down-dip and to the southeast (Fuchs et al., 1979) and are separated by ~10s of seconds and ~100km. This earthquake was particularly devastating to the city of Bucharest where over 90% of the ~1600 fatalities occurred (Georgescu and Pomonis, 2008). The cascading failure of these multiple reverse-polarity events is similar to observations in the Bucaramanga Nest, but on a much larger scale.

The Bucaramanga Nest, Colombia – 6.8°N 73.1°W – 4x4x8km

The Bucaramanga Nest (BN) will be a focal point of this dissertation, some properties of the tectonic setting are detailed in this section, but an in-depth discussion of seismicity patterns are detailed in Chapters 3 and 4.

Tectonics of the Bucaramanga Region

The Bucaramanga Nest is located beneath northern Colombia in a complex tectonic setting (Figure 1-3). The tectonics of the Northern Andes involved the subduction of the Caribbean (CAR) and Nazca (NAZ) plates and associated slab fragments beneath the South American plate (SAM). The Caribbean Plate (dip direction ~130°) has a shallow dip ~25° and rather slow rate of convergence (1.4 cm/yr, Freymuller et al., 1993). In contrast, the Nazca Plate (dip direction 80-100°) dips more steeply ~50°, with a much faster rate of convergence (7 cm/yr, Freymuller et al., 1993). In the region of interest, the Nazca Plate is commonly further divided into three slab segments (from south to north): the Peru (flat slab) segment, the Ecuador segment and the Central Colombia segment, with substantial overlap between the two northern-most segments (Corredor, 2003).

The specific location of the Bucaramanga Nest within this tectonic framework is debated in the literature. Some authors argue for a location on the Nazca Plate (van der Hilst and Mann, 1994), others place the nest within the Caribbean Plate (Cortes and Angelier, 2005; Corredor, 2003), and Zarifi et al., 2007 argue Bucaramanga Nest earthquakes are the result of a collision between the two plates.

Evidence for the Nazca Plate location

An iterative inversion using earthquakes from 1964-1989 leads to a tomographic image of the northern Andes that suggests that the Bucaramanga Nest is located on top of the subducting Nazca Plate (van der Hilst and Mann, 1994). The results show a steeply dipping slab, which the authors call a "redefined Bucaramanga slab." This interpretation places the nest in contact with the overlying mantle wedge, allowing for dehydration reactions to account for the intermediate-depth seismicity in the region. The authors suggest a complex stress field and the possible collision of the Bucaramanga slab with their Maracaibo slab (Caribbean Plate), similar to a scenario explored later by Zarifi et al. (2007).

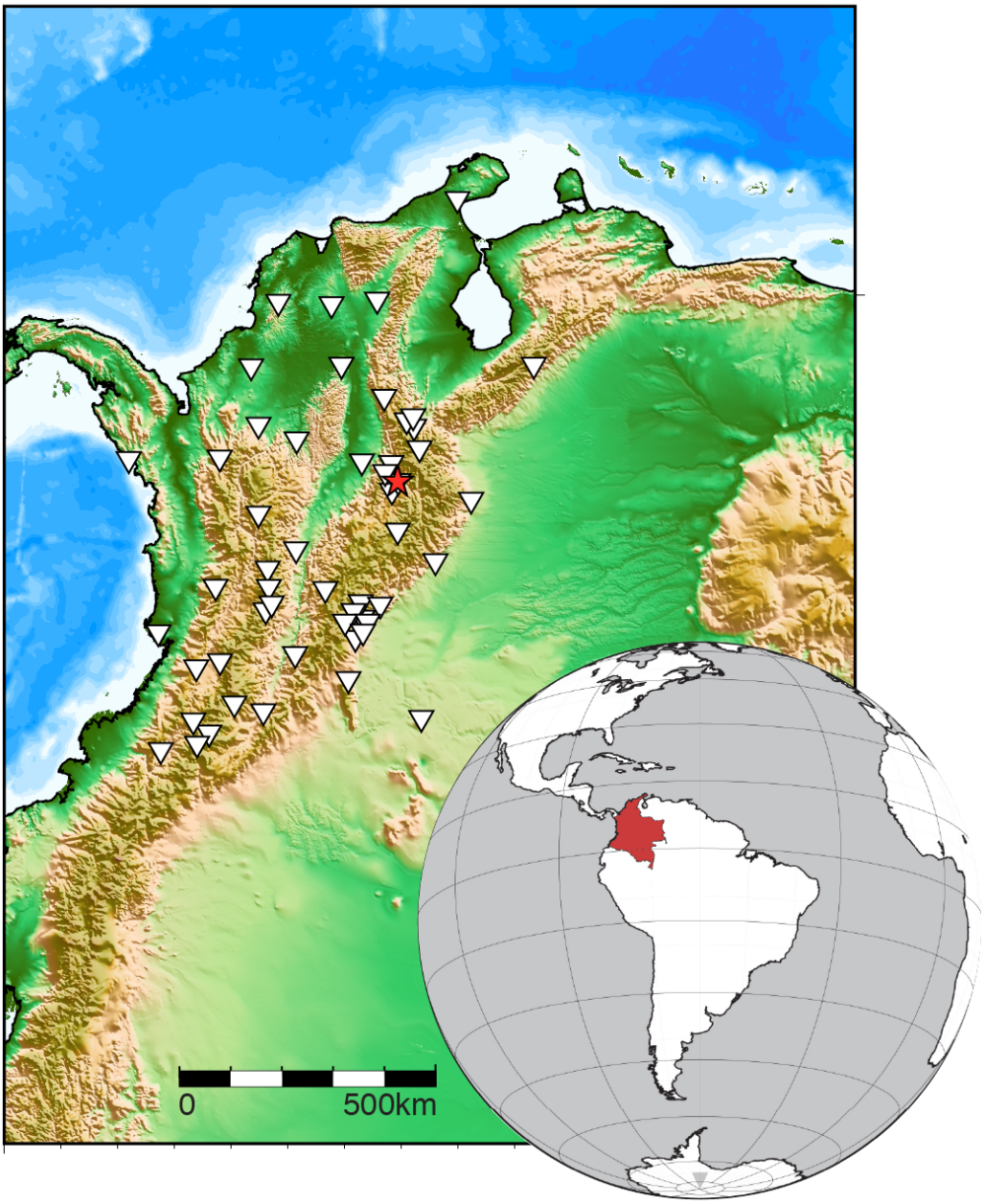

Figure 1-3. Setting of the Bucaramanga Nest and the National Colombian Seismic Network (RSNC). Colombia is located on the northern most portion of South America. In the north, the Caribbean Plate subducts at a typical angle (~20°) while the Nazca Plate subducts from the west at a much higher dip (~60°). The Bucaramanga Nest (red star) is thought to be associated with Caribbean Plate subduction. Also shown are RSNC stations used in this work (white triangles).

Evidence for the Caribbean Plate location

A Caribbean Plate location for the Bucaramanga Nest is explored by many works (e.g. Pennington, 1981; Taboada et al., 2000; Vargas et al., 2013) and is the accepted location for further work in this dissertation. A model produced by Corredor (2003), computes moment tensors of moderate-sized earthquakes for the Caribbean Plate and Nazca Plate segments. The results show a Caribbean Plate extending farther south (to nearly the Central Colombia segment of the Nazca Plate) and places the Bucaramanga Nest very near the southern terminus of the plate. Other authors (Cortes and Angelier, 2005) use a focal mechanism inversion to model the stress regime of the region. They propose a tear in the subducting Caribbean slab, consistent with the minimum stress direction (σ_3) as obtained in their inversion, with concentrated normal stresses at the rip boundary. This setting is akin to a propagating crack. The existence of a tear is further supported by the proposed location at the point of maximum curvature in the subducting slab.

There is also some discussion a complex stress system formed by a contorted slab hosting the nest seismicity. This situation would be analogous to the proposal for the Hindu-Kush Nest by Pegler and Das (1998). In this thesis, we use the Caribbean Plate location for the Bucaramanga Nest, based on the work discussed in Prieto et al., 2012.

Interaction between the Nazca and Caribbean Plates

The presence of multiple subducting slabs and their respective slab fragments suggest the possibility of more unusual scenarios for interaction. Zarifi et al. (2007) investigate a circumstance in which the Caribbean Plate and Nazca Plate collide at some depth. A 3D finite element model shows the effect of the proposed plate collision on the stress field, the altered stress field is proposed trigger the Bucaramanga Nest seismicity.

Small proposed nests of Colombia: Cauca and Murindo Nests

A few lesser-documented nests are located in Colombia, the Cauca and Murindo Nests. The Cauca nest is located in western Colombia at ~4.5°N 76.3°W and is likely associated with subduction of the Nazca Plate. While this nest is not nearly as active

as the Bucaramanga Nest, it does seem to show clustering of seismicity separate from the Wadati-Benioff-zone-related seismicity. It is possible this nest is associated with slab tears (Cortés and Angleier, 2005) due to the extreme bending of the Nazca Plate in this region. Some authors refer to this as the Caldas tear (Vargas et al., 2013). The same authors also suggest the presence of a nest farther north, the Murindo nest (~6.5°N, 76.5°W).

Other proposed global nests

A broad definition for earthquake nests allows for other possibilities around the globe including Fiji (Schneider et al., 1987) and Socompa near the Chile-Argentina border (Sacks et al, 1967). Other examples discussed in the literature such as Burma or Italy, do not have the concentrated seismicity that is a hallmark of the nests discussed above. The proposed nest in Ecuador is too closely located to a volcano (Cotopaxi) to rule out a volcanic origin for the nest – thus it does not fit into our proposed definition for an earthquake nest.

Failure Mechanisms of Intermediate-Depth Earthquakes

Shallow earthquakes fail through a brittle shear process; however, at intermediate- and deep-depths, high temperatures and pressures inhibit this failure mechanism. Another method of failure must be used to explain the failure mechanism of earthquakes with hypocentral depths greater than ~60 km. Several mechanisms have been proposed and the two most popular are (1) dehydration embrittlement and (2) thermal shear instability, which is the method favored in this thesis. Some authors (e.g. Green and Houston, 1995) have proposed independent mechanisms for intermediate-depth and deep earthquakes to explain the distribution of seismicity with depth which decreases to ~300 km and then has a second peak of activity at deeper depths (Figure 1-4). For the purposes of this work, we will only examine candidate mechanisms appropriate for intermediate-depths. For this reason, we do not consider transformational faulting or anti-cracks as these candidate mechanisms are suggested for depths well below the Bucaramanga Nest. We will also dismiss mechanisms such as solid-solid phase

transitions that imply a volumetric implosion. The discussion will be focused on the two most viable mechanisms of failure: dehydration embrittlement and thermal shear instability. Dehydration embrittlement is a popular option as it builds off known subduction processes, such as reactivation of hydrated faults, and allows for a failure process similar to shallow earthquakes. Thermal shear instability is a runaway process that relies on high shearing stresses. Much of the work on thermal shear instability failure began as laboratory experiments and has expanded to include observations from numerical modeling and observational seismology.

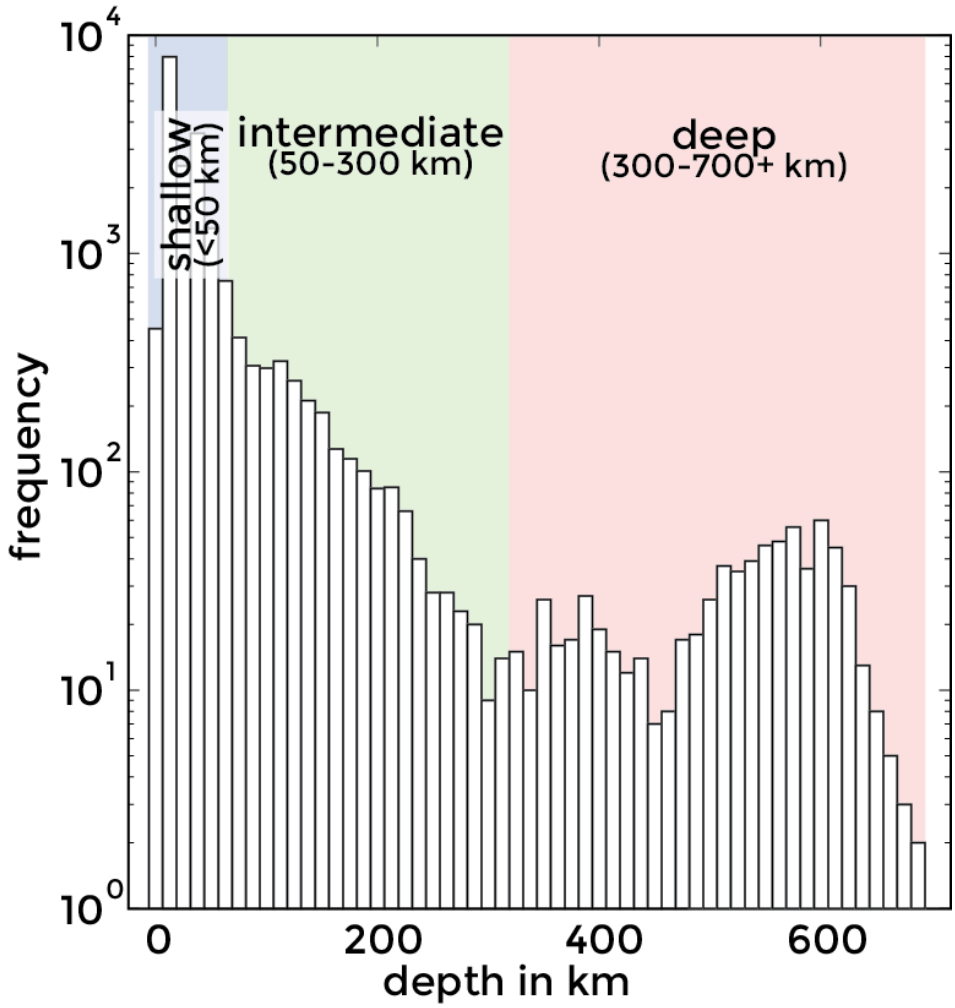

Figure 1-4. The distribution of seismicity with depth for a decade of seismicity. Shallow (<50 km depth) and intermediate-depth (50-300 km) earthquakes exhibit a decrease in frequency with increasing depth. Deep earthquakes (>300 km) seem to increase in frequency, opening the possibility for multiple failure mechanisms.

Dehydration embrittlement

The presence of pore fluids is known to promote failure under conditions that would otherwise not allow brittle failure (e.g. Scholz, 1990).

$$(\tau > \sigma_n - p_p) \qquad \textit{equation 1-1}$$

Where τ is the shear stress, σ_n the normal stress and p_p the pore pressure.

Most zones of intermediate-depth seismicity – including nest seismicity – are associated with active or historic subduction zones. Through this process, colder, hydrated material is in contact with the mantle. The mechanism of dehydration embrittlement involves the release of fluids from hydrous minerals in the subducting slab as pore fluids, encouraging brittle failure. Two important assumptions exist:

1. There must be a sufficient source of pore fluid (the subducting material is sufficiently hydrated)
2. The pore fluid pressure must not exceed the minimum principle stress, as this would induce hydrofracture.

Savage (1969) proposed a mechanism through which fluids might permeate through the thickness of the subducting slab. Outer-rise normal faults are common at most subduction zones and allow for hydration of the oceanic crust. During subduction, these faults are re-activated at depth, a concept supported by more recent studies (e.g. Peacock, 2001). Failure could occur in both the hydrated material near the slab surface and within the subducting slab. Hydration within the plate is possible about ~20 km into the lithosphere (Ranero et al., 2003). This is approximately the same distance as the separation between double seismic zones. Slab hydration is further supported by volcanic geochemistry. Studies of beryllium isotopes observe ^{10}Be in global subduction-zone volcanism, suggesting these hydrated sediments reached depths of at least 100 km.

Dehydration reactions can explain the observed distributions of seismicity in the slab (Hacker et al., 2003b). Hydration, the depth extent of seismicity and double seismic zones correspond to reactions in petrothermal models, four of which are discussed in detail in the Subduction Factory series of papers (Hacker et al., 2003a; Hacker et al., 2003b, Hacker and Abers, 2004; and van Keken et al., 2011):

1. Dehydration of basalt to produce earthquakes
2. Dehydration of gabbro to produce earthquakes and transition to eclogite
3. Local dehydration of upper mantle material to produce earthquakes
4. Anhydrous mantle transitioning aseismically from a spinel to garnet assemblage

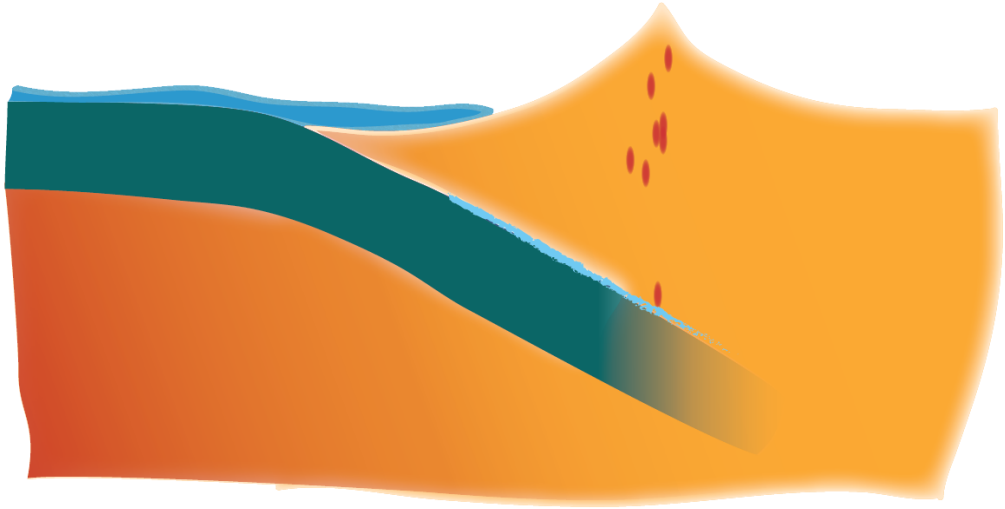

Figure 1-5. Dehydration embrittlement occurs when hydrous minerals in the down-going slab react to transition to a higher temperature and pressure state. The minerals tend to dehydrate as they go through such phase changes. The release of fluids can promote brittle failure by increasing the pore pressure and thereby reducing the effective normal stress.

The fluids produced in these dehydration reactions migrate through percolation via mode I cracks and through post seismic processes (Hacker et al., 2003b). The nature of these reactions suggests an exhaustive process. At some depth, most material will be sufficiently dehydrated and pressures will be too great to allow for shear failure, even with the remaining available fluid pressure. The depth of complete dehydration of

fluid bearing minerals should vary from subduction zone to subduction zone based on the thermal properties and original amount of fluids.

Shear instabilities or thermal-shear runaway

High axial shearing stress experiments in laboratories have unveiled another possible failure mechanism that is possible under high temperatures and pressures (e.g. Meade and Jeanloz 1991; Karato et al., 1998). Thermal shear instabilities represent a runaway positive feedback loop (Figure 1-6) resulting from high shear stresses. The laboratory results are also supported by numerical simulation (Keleman and Hirth, 2007), geologic observations (Andersen et al., 2008), seismic observations (Prieto et al., 2013), and a few anecdotal cases (e.g. Kanamori, 2004).

In laboratory experiments, a high axial shearing and associated stresses can prompt dilatancy hardening and increased friction in a sample. Along with an increase in friction, an increase in temperature can cause local melting (Bridgman, 1936) or readjustment of the crystalline structure known as amorphization (Meade and Jeanloz, 1991). These are both inherently weakening processes that can promote failure. Seismic failure can increase the temperature and friction in nearby regions, creating a positive feedback loop. For this reason, failure in shear instabilities that interacts with and is reinforced by shear heating is sometimes referred to as a thermal-shear runaway.

Numerical simulation by Kelemen and Hirth (2007) show a periodic failure pattern that might occur at mantle conditions. Their model has failure in pre-existing fine-grained zones, surrounded by a coarse-grained elastic halfspace. The initial temperature conditions are from 600-800° C, which is usually considered to be the upper bound for seismic failure and an initial strain rate of 10^{-15} – 10^{-12} s^{-1}. They observe rapid increases of strain rate and temperature followed by a dramatic stress drop and a return to initial strain rates. This failure pattern is repeated with a quasi-periodic recurrence, which the authors attribute to far-field deformation rates.

Studies of pseudotachylyte fault veins in Corsica yield bounds on the necessary temperature increase (and associated stress drop) necessary to produce melting of the peridotite facies (Andersen et al., 2008). If the stress drop is proportional to the amount of melting, the authors estimate 220-580 MPa stress drops, substantially higher than the accepted range of stress drop for shallow earthquakes (Baltay et al., 2011; Abercrombie, 1995). The abundance of small veins of pseudotachylyte in the region imply this maybe a common process at intermediate- and deep-depths.

A detailed look at the energy budget of intermediate-depth earthquakes provides seismic observations that support a thermal shear failure (Prieto et al., 2013). Bucaramanga Nest earthquakes of moderate size (M_w 4-5) show a relatively high stress drop and low radiation efficiency. A seismic failure of this type would produce a rapid increase in temperature (600-1000° C) in a layer a few centimeters thick. The temperature increase could cause melting or a change in the crystalline structure, which should act to initiate the positive feedback loop of thermal-shear runaway.

Kanamori (2004) inferred that shear melting might have occurred during the rupture process of the 1994 Bolivian earthquake (647 km depth). Several other studies reach similar conclusions, yet all require relatively high stress drops ($\Delta\sigma >\sim 55$ MPa).

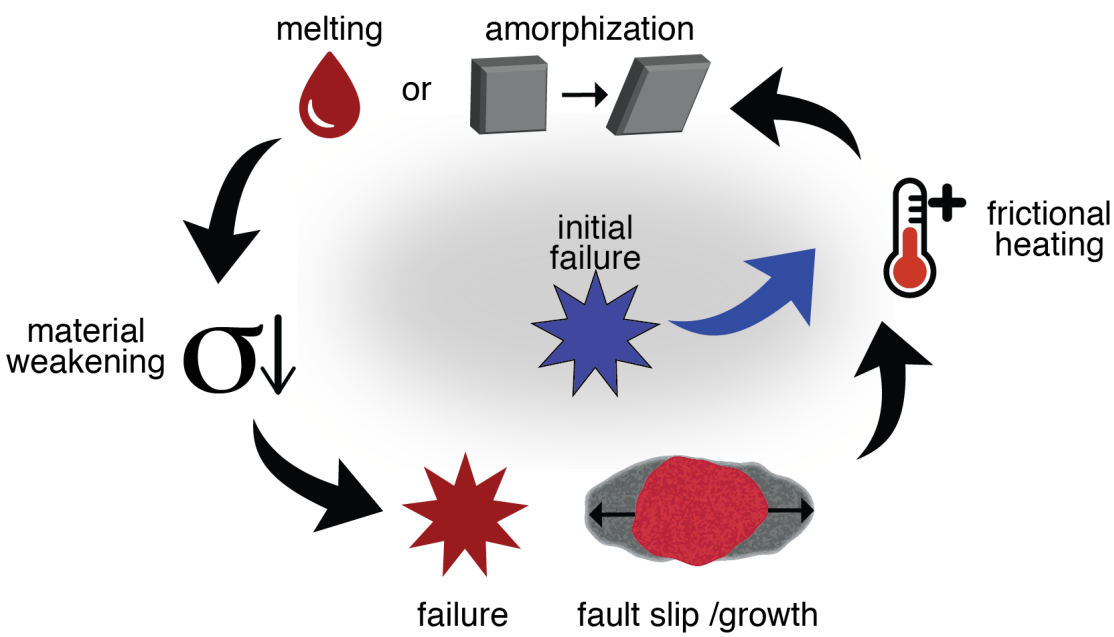

Figure 1-6. A schematic of the positive feedback processes associated with thermal shear instability. An increase in friction and temperature can cause a shift in the material structure (amorphization or melting). The weakened material can fail seismically. The fault slip or growth associated with this failure is shown to increase temperature in the surrounding region.

Most authors agree a critical shear zone thickness (Z, equation 1-2) is important in this process. If the shear zone is too thin, thermal shear failure is prevented by conduction; if the zone is too thick, failure is prevented when there is an insufficient elastic energy concentration to produce the critical temperature instability required for failure (e.g. Ogawa, 1987).

$$Z > \frac{\rho C_p \Delta T \, \kappa}{\upsilon \tau} \qquad \textit{equation 1-2}$$

ρ – density
C_p – specific heat
ΔT – change in temperature needed to achieve melting
κ – thermal diffusivity
υ – velocity of plastic deformation
τ – shear stress

One potential shortcoming of this theory is the lack of observations of acceleratory precursory creep prior to failure, which might appear on very low-frequency records

of large deep earthquakes (Frohlich, 2006); however it might be difficult to observe these faint signals at typical event to station distances. At intermediate-depths the stresses are high and it is reasonable to assume that thermal runaway might accelerate too rapidly to observe.

Alternative methods of failure

In addition to the two leading theories of dehydration embrittlement and thermal shear instabilities, there are alternative failure mechanisms discussed in the literature.

As the subducting slab descends into the earth, many minerals undergo phase transitions as they transition from low to high pressure. The contrast of a new phase surrounded by its parent material can act as an anti-crack – that is a mode-I failure that involves a reduction in volume (Green and Burnley, 1989) and result in transformational faulting. The presence of meta-stable olivine in a subducting slab allows for the creation of shear instabilities when olivine breaks down into its high-pressure polymorphs (Green 2007). The anti-cracks eventually link into protofaults (with oblique orientations to the principal stress; Green and Houston, 1995), supporting observations that support the fracture of intact rock at intermediate and deep depths. Such changes have been observed in ice I to ice II (Kirby, 1987), olivine germanate α to spinel γ (Green & Burnley, 1989) and olivine α to modified spinel β (Green et al., 1990). The later is the only of these studies performed at transition zone temperatures and pressures (15 GPa, 1650°K). Many of these transitions are exothermic reactions that would allow for a runaway process of transition and faulting.

These reactions occur at greater depths than intermediate-depth earthquakes (~50-300 km) and are not a viable option in this study. Furthermore, Hacker et al., (2003) notes that transformational faulting is not a viable mechanism for oceanic crust as most solid-state reactions that occur in metamorphosing basalt to eclogite are not polymorphic. Additionally this model of faulting cannot predict large fault widths

often inferred for deep earthquakes (Wiens, 2001) as this would require large scale phase transitions on the order of earthquake rupture area for events M~8.

Phase transitions (solid-solid) with a net volume change were historically associated with deep earthquakes, although there is little evidence to support this claim. Deep earthquakes generally constrained to have at most a very small isotropic component (<10%). Similar constraints apply to these phase transitions with other mechanisms; failure must propagate at earthquake rupture speeds, and phase transitions can only occur for a given location once (which would seem to be inconsistent with observations of repeating deep events, e.g. Wiens & Snider, 2001). Martensitic materials (enstatite) could also emit acoustically; however, enstatite is not present in large enough quantities to yield failures on seismic scales (Green & Houston, 1995). These solid-solid phase transitions are also highly unlikely to occur on known rupture scales of large deep earthquakes (which may be as large as 10-100 km).

Summary of the Contents of this Thesis

This introduction is an overview of the range of ideas concerning the nature of intermediate-depth earthquakes with respect to their locations (nests) and on leading theories on their failure mechanism.

Chapter 2 introduces a novel modification of an established detection method that substantially improves detection results. This empirical subspace detector works much like traditional template matching, but utilizes the similarity between the second singular vector and the time derivative of a template to detect events with highly similar waveforms with greater reliability. The example application is to a well-recorded aftershock sequence in Southern California. The empirical subspace method detects more earthquakes than traditional methods. It is effective at improving detections for large event to station distances on single components. The new earthquakes are smaller magnitude and often occur as overlapping events. The method is also used in Chapter 4 to detect more earthquakes in the Bucaramanga Nest.

The repeating, and more curious, anti-repeating earthquakes observed in the Bucaramanga Nest are examined in Chapter 3. While repeating earthquakes are observed in many locations, repeating events with reversed polarity is a new observation. We call these events reverse polarity repeats. We examine a sequence of these repeating and reverse polarity repeating earthquakes in both space at time. Some events within a group repeat very closely in both dimensions (13 meters and 13 seconds). The cascading type failure process is consistent with lines of observation supporting thermal-shear instabilities and boudin formation on large scales.

The focus of Chapter 4 is on the magnitude of the Bucaramanga Nest earthquakes. We seek to identify all earthquakes in a six-month sequence and determine the probability that an earthquake of a given size is detectable. We observe a deviation from Gutenberg-Richter magnitude-frequency distributions at small magnitudes that cannot be attributed to limitations on earthquake detectability. We suggest that the deficiency in small magnitude earthquakes within the Bucaramanga Nest is thought to be indicative of a minimum rupture size, related to the need to achieve sufficient weakening for sudden shear failure to occur. This interpretation supports a runaway failure mechanism such as thermal shear instability for intermediate-depth earthquakes.

The final chapter summarizes the evidence for thermal shear failure and the nature of intermediate-depth earthquakes within earthquake nests by synthesizing the evidence and results presented in the prior chapters.

References

Abercrombie, R. E., (1995). Earthquake source scaling relationships from -1 to 5 M_L using seismograms recorded at 2.5-km depth, *J. of Geophys. Res.*, **100**, B12, 24015-24036.

Andersen, T. B., K. Mair, H. Austrheim, Y. Podladchikov, and J. C. Vrijmoed, (2008). Stress release in exhumed intermediate and deep earthquakes determined from ultramafic pseudotachylyte, *Geology*, **36**, 12, 995-998; doi: 10.1130/G25230A.1.

Baltay, A., G. Prieto, and G. C. Beroza, (2010). Radiated seismic energy from coda measurements and no scaling in apparent stress with seismic moment, *J. Geophys. Res.*, **155**, B08314, doi: 10.1029/2009JB006736.

Beck, S., S. Barrientos, E. Kausel, and M. Reyes, (1998). Source characteristics of historic earthquakes along the central Chile subduction zone, *Journal of South American Earth Sciences,* **11**, (11), 115-129. doi: 10.1016/S0895-9811(98)00005-4.

Billington, S., B. Isacksa, and M. Barazangi, (1977). Spatial distribution and focal mechanisms of mantle earthquakes in the Hindu Kush-Pamir region: A contorted Benioff zone, *Geology*, 5, 699-704.

Bridgeman, P. W., (1936). Shearing phenomena at high pressure of possible importance for geology, *J. Geol.*, **44**, 653-669.

Chatelain, J.L., Roecker, S. W., Hatzfeld, D., and P. M. Molnar (1980). Microearthquake seismicity and fault plane solutions in Hindu Kush Region and their tectonic implications. *J. Geophys. Res.*, 85, 1365-1387, doi: 10.1029/JB085iB03p01365.

Corredor, F., (2003). Seismic Strain Rates and Distributed Continental Deformation in the Northern Andes and Three-Dimensional Seismotectonics of Northwestern South America, *Tectonophysics,* 372, 147-166.

Cortés, M. and J. Angeleir, (2005). Current States of Stress in the Northern Andes as Indicated by Focal Mechanisms of Earthquakes, *Tectonophysics*, 403, 29-58.

del Canto, H., P. Godoy, E. Aguirre, J. Muñoz-Christi, and J. Ibáñez, (1940). Informe de la commission gubernativa sobre los efectos producidos por el Terremoto de Enero de 1939, *Anales del Instituto de Ingenieros de Chile*, Oct-Nov, 376-395.

Fan, G., J. F. Ni, and T. C. Wallace (1994). Active Tectonics of the Pamirs and Karakorum, *J. Geophys. Res.*, 99 (B4): 7131-7160, doi: 10.1029/93JB02970.

Fattal, G., E. Simiu, and G. Culver, (1977). *Observations on the Behavior of Building in the Romania Earthquake of March 4, 1977*, U.S. National Bureau of Standards Special Publication 490, 168 pp.

Freymueller, J. T., and J.N. Kellogg, (1993). Plate Motions in the North Andean Region, *J Geophys*. Res, 98(B12), 21,853-21,863.

Frohlich, C. (2006), Deep Earthquakes, Cambridge Univ. Press, Cambridge.

Fuchs, K. E. A., Bonjer, K. P., Bock, G., Cornea, I., Radu, C., Enescu, D., ... & Tudorache, G., (1979). The Romanian earthquake of March 4, 1977 ii. Aftershocks and migration of seismic activity, *Tectonophysics*, 53 (3), 225-247.

Georgescu, E. S., & Pomonis, A. (2008). The Romanian Earthquake of March 4, 1977 revisited: new insights into its territorial, economic and social im4pacts and their bearing on the preparedness for the future. In Proceedings of the 14th World Conference on Earthquake Engineering (pp. 12-17).

Green, H. W., T. E. Young, D. Walker and C. H. Scholz, (1990). Anticrack-associated faulting at very high pressure in natural olivine, *Nature*, **348**, 720722, doi:10.1038/348720a0.

Green, H. W., (2007). Shearing instabilities accompanying high-pressure phase transformations and the mechanics of deep earthquakes, *Proceedings of the National Academy of Sciences*, **104**, (22), 9133-9138, doi: 10.1073/pnas.0608045104.

Green, H. W. and P. C. Burnley, (1989). A new self-organizing mechanism for deep-focus earthquakes, *Nature*, **341**, 733-737, doi: 10.1038/341733a0.

Green, H. W., and H. Houston, (1995). The Mechanics of Deep Earthquakes, *Annu. Rev. Earth Planet. Sci.,* 22 (16): 2265. doi:10.1029/95GL01602.

Hacker, B. R., G. A. Abers, and S. M. Peacock, (2003a). Subduction Factory 1. Theoretical Mineralogy, Densities, Seismic Wave Speeds, and H 2O Contents, *J. Geophys. Res.*, 108 (B1). doi:10.1029/2001JB001127.

Hacker, B. R., S. M. Peacock, G. A. Abers, and S. D. Holloway, (2003b). Subduction Factory 2. Are Intermediate-Depth Earthquakes in Subducting Slabs Linked to Metamorphic Dehydration Reactions?." , *J. Geophys. Res.*, 108 (B1). doi:10.1029/2001JB001129.

Hacker, B. R. and G. A. Abers, (2004). "Subduction Factory 3: an Excel Worksheet and Macro for Calculating the Densities, Seismic Wave Speeds, and H_2O Contents of Minerals and Rocks at Pressure and Temperature." *Geochemistry Geophysics Geosystems* 5 (1) Q01005,

Havskov, J., and Z. Zarifi, (2003). Characteristics of Dense Nests of Deep and Intermediate-depth Seismicity, *Advances in Geophysics*, 46, 237-278.

Jiricek, R. (1979). Tectogenetic development of the Carpathian arc in the Oligocene and Neogene. In *Tectonic profiles through the West Carpathians* (pp. 205-214). Geologicky Ustav Dionyza Stura Bratislava.

Kanamori, H., (2004). The diversity of the physics of earthquakes, *Proceedings of the Japan Academy*, **80**, (7), 297-316, doi:10.2183/pjab.80.297.

Karato, S., C. Dupas-Bruzek, and D. Rubie (1998). Plastic deformation of silicate spinel under the transition-zone conditions of the Earth's mantle, *Nature*, **395**, 266-269, doi:10.1038/26206.

Kelemen, P. B. and G. Hirth (2007). A periodic shear-heating mechanism for intermediate-depth earthquakes in the mantle, *Nature*, **447**, 787-790. doi:10:1038/nature05717.

Kirby, S. H., (1987). Localized polymorphic phase transformations in high-pressure faults and applications to the physical mechanism of deep earthquakes, *J. Geophys. Res.*, **92**, 13789-13800, doi:10.1029/JB092Ib13P13789.

Kiser, E., M. Ishii, C. H. Langmuir, P. M. Shearer, and H. Hirose, (2011). Insights into the mechanism of intermediate depth earthquakes from source properties as imaged by back projection of multiple seismic phases, *J. Geophys. Res.*, 116, B06310, doi:10.1029/2010JB007831.

Koulakov, I., B. Zaharia, and B. Enescu, (2010). Delamination or Slab Detachment Beneath Vrancea? New Arguments From Local Earthquake Tomography. *Geochem Geophys. Geosys.*, **11**, 3, doi: 10.1029/2009GC002811.

Lister, G., B. Kennett, S. Richards and M. Forster (2008). Boudinage of a stretching slablet implicated in earthquakes beneath the Hindu Kush, *Nature Geosci.*, 1, 196-201, doi:10.1038/ngeo132

Meade, C., and R. Jeanloz, (1991). Deep-Focus Earthquakes and Recycling of Water Into the Earth's Mantle, Science, 252 (5002): 68–72.

Müller, G., Bonjer, K. P., Stockl, H., & Enescu, D. (1978). Romanian earthquake of March 4, 1977 i. Rupture process inferred from fault-plane solution and multiple-event analysis, *J. of Geophys.-Zeitschrift fur Geophysik*, 44 (3), 203-218.

Nowroozi, A. A., (1971). Seismo-tectonics of the Persian plateau, eastern Turkey, Caucasus, and Hindu-Kush regions, *Bullet. Seism. Soc. Am.*, **61**, (2), 317-341.

Ogawa, M., (1987). Shear instability in a viscoelastic material as the cause of deep focus earthquakes, *J. Geophys. Res.*, **92**, 13801-13810, doi:10.1029/JB092iB13p13801.

Omori, F. (1895). On the after-shocks of earthquakes, *J. Coll. Sci. Imper. Univ. Tokyo,* **7**, (2), 111-200.

Pavlis, G. L. and M. W. Hamburger, (1991). Aftershocks sequences of intermediate-depth earthquakes in the Pamir-Hindu Kush seismic zone, *Journal of Geophysical Research*, **96**, B11, 18107-18117, doi: 10.1029/91JB01510.

Peacock, S.M. (2001). "Are the Lower Planes of Double Seismic Zones Caused by Serpentine Dehydration in Subducting Oceanic Mantle?" *Geology*, 29, 299-203.

Pegler, G. and S. Das, (1998). An enhanced image of the Pamir-Hindu Kush seismic zone from relocated earthquake hypocenters, *Geophys. J. Int.*, 134, 573-595.

Pennington, W. D., (1981). Subduction of the eastern Panama Basin and seismotectonics of northwestern South America. *J. of Geophys. Res. 86*(B11), 10753-10770, DOI: 10.1029/JB086iB11p10753.

Preito, G. A., G. C. Beroza, S. A. Barrett, G. A. López, and M. Florez, (2012), *Tectonophysics*, 570-571, 42-56, doi.org/10.1016/j.tecto.2012.07.019

Preito, G. A., M. Florez, S. A. Barrett, G. C. Beroza, P. Pedraza, J. Faustino, and E. Poveda, (2013). Seismic evidence for thermal runaway during intermediate-depth earthquake rupture, *Geophysical Research Letters*, **40**, 6064-6068; doi:10.1002/20013/GL058109.

Ranero, C. R., J. P. Morgan, and K. McIntosh, (2003). Bending-Related Faulting and Mantle Serpentinization at the Middle America Trench. *Nature*, 425, 367-373.

Sacks, I. S., Suyehiro, S., Kamitsuki, A., Tuve, M. A., Otsuka, M., Saa, G., ... & Aldrich, L. T. (1966). A tentative value of Poisson's coefficient from the seismic" nest of Socompa. *Annual report of the Director, Carnegie Inst.". Technical report Dep. of Terr. Magn.*

Saita, T., (1940). The great Chilean earthquake of January 24, 1939, *Bull. Earthquake Res. Inst., Tokyo Univ.,* **18**, 446-459.

Savage, J. C., (1969). The Mechanics of Deep-Focus Faulting. *Tectonophysics* 8, (2), 115-127.

Schneider, J. F., Pennington, W. D., & Meyer, R. P. (1987). Microseismicity and focal mechanisms of the intermediate depth Bucaramanga nest, Colombia,*J. of Geophys. Res.* **92**, (B13), 13913-13926, doi: 10.1029/JB092iB13p13913.

Scholz, C. H., (1990). *The Mechanics of Earthquakes and Faulting*. Cambridge University Press: New York, New York.

Sperner, B., F. Lorenz, K. Bonjer, S. Hettel, B. Müller, and F. Wenzel, (2001). Slab Break-Off – Abrupt Cut or Gradual Detachment? New Insights From the Vrancea Region (SE Carpathians, Romania), *Terra Nova* 13 (3): 172–179. doi:10.1046/j.1365-3121.2001.00335.

Taboada, A., L. A. Rivera, A. Fuenzalida, A. Cisternas, H. Philip, H. Bijwaard, J. Olaya, and C. Rivera, (2000). Geodynamics of the Northern Andes: Subductions and Intracontinental Deformation (Colombia). *Tectonics* 19 (5): 787–813. doi:10.1029/2000TC900004.

van der Hilst, R., and P. Mann, (1994). Tectonic implications of tomographic images of subducted lithosphere beneath northwestern South America, *Geology*, 22, 451- 454.

van Keken, P. E., B. R. Hacker, E. M. Syracuse, and G. A. Abers (2011). Subduction factory: 4. Depth-dependent flux of H2O from subducting slabs worldwide, *J. Geophys. Res.*, 116, B01401, doi:10.1029/2010JB007922.

Vargas, C. A., & Mann, P., (2013). Tearing and Breaking Off of Subducted Slabs as the Result of Collision of the Panama Arc-Indenter with Northwestern South America. *Bulletin of the Seismological Society of America*, 103(3), 2025-2046, doi: 10.1785/0120120328

Wiens, D. A., (2001). Seismological constrains on the mechanism of deep earthquakes temperature dependence of deep earthquake source properties, *Phys. Earth Planet. Int.*, **127**, 145-163, doi:10.1016/S0031-9201(01)00225-4.

Weins, D. A. and N. O. Snider, (2001). Repeating deep earthquakes: evidence for fault reactivation at great depth, *Science*, **293**, (5534), 1463-1466, doi:10.1126/science.1063042.

Zarifi, Z., J. Havskov, and A. Hanyga, (2007). An Insight Into the Bucaramanga Nest." *Tectonophysics,* 443, 93-105.

CHAPTER TWO

An Empirical Application to Subspace Detection

Abstract

Earthquake detection remains one of the essential procedures in seismology. We offer an empirical adaptation to traditional, theoretical subspace detection methods. Our empirical subspace detector is a matrix composed of the waveform and its time derivative. This matrix very closely approximates the first two singular vectors in the theoretical subspace methods (a subspace dimension with $n = 2$). We show the usefulness of this detector to perform as well as the theoretical version, with minimal effort from an analyst. We display detections of overlapping events that are undetected using traditional methods. Moreover, we showcase an application that uses a single component of a single station at ~60 km distance from the swarm, implying the effectiveness of this method in regions of sparse station spacing.

Earthquake Detection Methods

A complete and precise catalog of earthquakes is a necessarily prerequisite to studies of seismicity. Standard detections rely on arrival-time picks to obtain possible first-arrival times and an association algorithm to access if those times are consistent with a

source within the Earth. Most methods use either complete *a priori* knowledge of the seismic waveform (template matching) or the generalization that an earthquake has higher energy than the ambient seismic field (energy based detectors).

Correlation-based detectors

Template matching, or waveform cross-correlation (Van Trees, 1968), exploits waveform similarity of nearby earthquakes. This is a powerful approach to detecting highly similar events with success in regions with high signal-to-noise ratios or where events might be closely spaced in time (waveforms overlap). The use of correlation methods is quickly growing and have widespread applications in mining-induced seismicity (Gibbons and Ringdal, 2006), in suspected induced seismicity (van der Elst et al., 2013), in nuclear test ban treaty verification (Rowe et al., 2012), in aftershock detection (Peng and Zhao, 2009) and in low-frequency earthquakes (Shelly et al., 2006, 2007). Shortcomings of this method are based on the requirement of a cataloged event waveform that is highly similar to those of interest, and the assumption that specific source waveform repeats (Brown et al., 2008). Such prior knowledge or occurrence of seismicity is not always available or useful in noisy regions.

Energy-based detectors

In cases where little is known about a region or its seismicity, a more general, energy-based detector is appropriate. These methods, such as short-term average/long-term average (STA/LTA) utilize impulsive, high signal-to-noise first arrivals of earthquakes. This is best implemented within a seismic network to verify an arrival. Energy based detectors are unsuitable under conditions of low signal-to-noise ratio, overlapping earthquakes (e.g. aftershocks, swarms), for emergent first arrivals, or in networks where events are sparsely recorded. Such methods generally require several instruments to provide independent detection information (typically four, to constrain the hypocenter).

Subspace-based detectors

Subspace detectors act as an intermediary method: a generalization of template matching into multiple dimensions. The detectors are constructed from the singular value decomposition of a matrix that consists of a design set of waveforms (Harris, 2006; Harris and Paik, 2006). The subspace detection algorithm makes the assumption that uncataloged events can be represented as a linear combination of a portion of the largest singular vectors in the design set matrix subspace. Common features of the waveforms will manifest in an orthonormal representation of the events. These detectors have been applied to cases of tremor (e.g. Maceira et al., 2010) with some success but have not seen wide adaptation in earthquake monitoring and detection.

Methods of Subspace Detection

The singular value decomposition (Eqn. 1) of a matrix **A** produces three matrices. The matrix **U** (left singular vectors) is composed of orthonormal vectors that span the subspace, the singular values (**Λ**) which provides the proper weighing of the singular vectors, and the right singular vectors (**V**) which are also orthonormal. In this application, the matrix **A** has columns composed of earthquake waveforms aligned to the *P*-arrival. The result of the singular value deposition yields left singular vectors (**U**) with columns that form the basis for design set waveforms.

$$SVD(A) = U \Lambda V^T \qquad \textit{equation 2-1}$$

If we rank the singular vectors according to the size of their corresponding singular value, then the first singular vector contains the information common to the design set. This vector has the greatest power to describe the set of waveforms. The second singular vector contains the dominant remaining information common to the design set, once the contribution of the first singular vector is removed. This process continues with each successive vector containing increasingly smaller contributions to describing the design set. Information in these later vectors can be thought of as details specific to certain waveforms or subsets of the design set. These vectors can be used

as detectors (Harris 2006; Harris and Paik, 2006). It is sometimes suitable to truncate the matrix to an acceptable dimension that accurately represents the design set at a specific level.

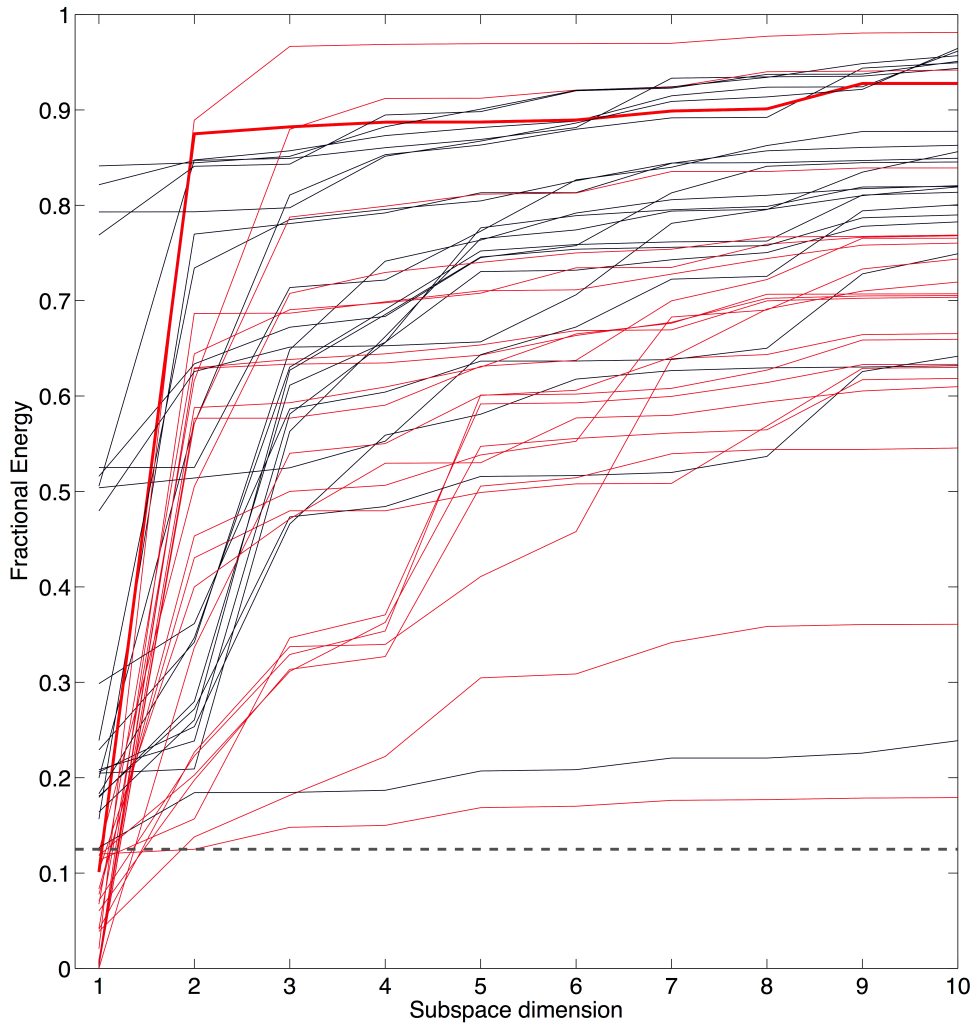

Figure 2-1. The fractional energy capture for the following subspace detection application. The 66 waveforms are all well represented at the 0.125 threshold (dashed line) by either one-dimension (black line) or two-dimensions (red line). The darkened red line represented the 'master event' used for *P*-wave alignment.

The appropriate dimension of **U** to use can be verified by using a fractional energy capture. In this example, we see that all design set waveforms is well represented by two singular vectors (Figure 2-1). Other cataloged events may require the additional dimensions to be represented at a given level, here 0.125. This level can be computed

statistically, or by examination of the problem. For example, more disperse seismicity or variation in focal mechanism might require additional dimensions to explain a more diverse set of waveforms.

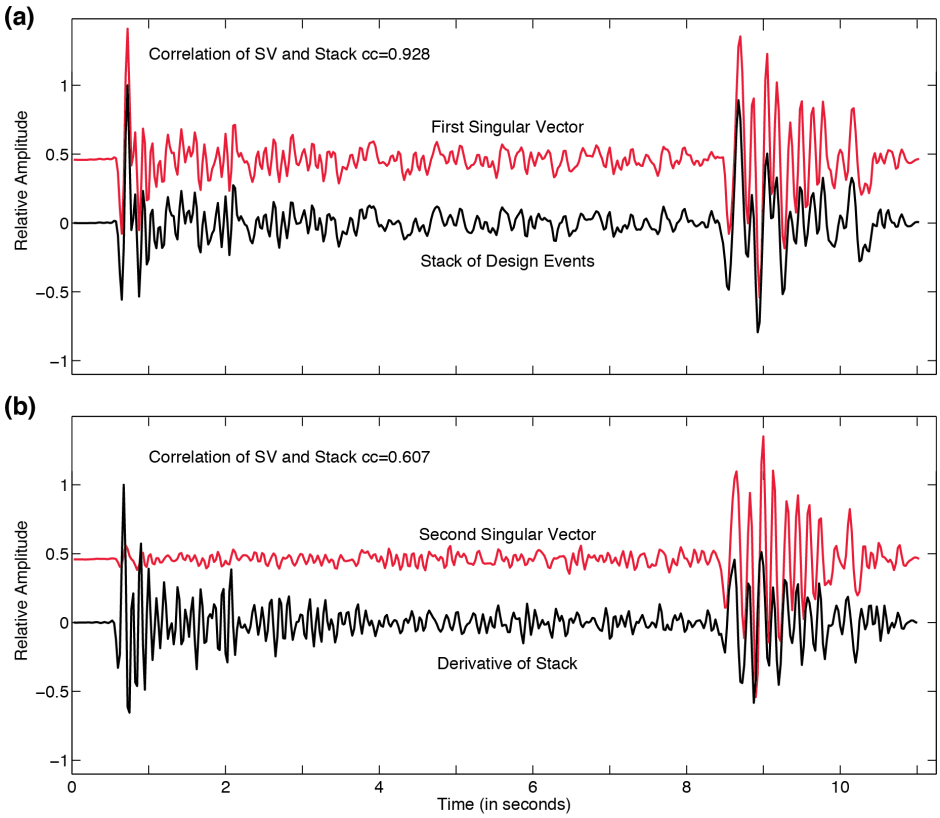

Figure 2-2. (a) The largest singular vector (red) shows similarity to the stack (black) of the 66 design set events (cc = 0.928). (b) The second largest singular vector (red) resembles the time derivative (black) of the design set stack (cc = 0.607), especially in the portion corresponding to the *S*-wave arrival. All waveforms are normalized to unit amplitude.

We find that for localized groups of seismicity, the first singular value is highly similar to the average waveform (stack) of the design set (Figure 2-2a). This finding is unsurprising as the first (largest) singular vector contains information common to the design set. It should therefor be similar to the average, or stack of the design set. A more interesting investigation into the second singular vector shows it is highly similar to the time derivative of the average seismogram, especially in the region corresponding to the *S*-wave arrival (Figure 2-2b). We suggest this is due to variability

in the seismogram that results from location differences in the earthquakes (i.e. changes in the *S*-*P* times). The *S*-wave arrival dominates the amplitude in the second singular vector since the design set matrix **A**, is constructed using *P*-wave alignment. Successive singular vectors do not have a clear physical representation, that is to say, they do not represent higher order derivatives of the average waveform. Examination of the fractional energy capture for this data set (Figure 2-1) suggests the first two singular vectors are sufficient to represent the design set of waveforms.

Instead of using the first two singular vectors, we propose exploiting the similarity of these vectors to the stack and the time derivative of the stack, and using these two physical representations as an analog for a theoretical subspace. In forming a matrix composed of two vectors: the average seismogram and its time derivative, we create a new detector, which we call an empirical subspace. We demonstrate the utility of this matrix of the first two singular vectors as a method for earthquake detection on a well-recorded aftershock sequence.

Application to 2003 Big Bear Sequence

The 2003 M_w 5.0 Big Bear earthquake occurred on 22 February 12:19:10 (UTC) at 34.41° N 116.85° W (Figure 2-3). It occurred in the same region as the 1992 *M* 6.5 Big Bear earthquake, the largest aftershock of the 1992 *M* 7.3 Landers event. This event occurred in the Eastern California Shear Zone, a complex tectonic region, but was most likely associated with failure on the Helendale Fault. The area is composed of primarily northwest-trending faults with several conjugate northeast trending faults. It is bounded to the north by the frontal thrust of the San Bernardino Mountains and the San Andreas Fault to the south (Jones et al., 1993).

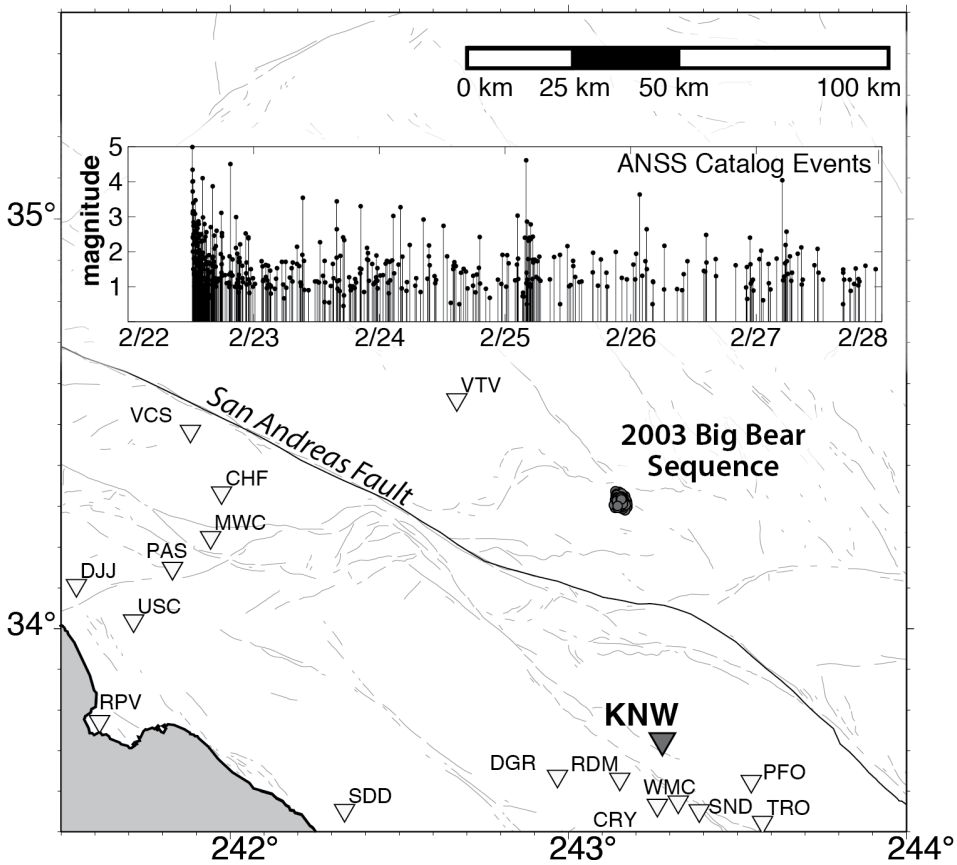

Figure 2-3. Seismicity during the Big Bear swarm as recorded by the Advanced National Seismic System (ANSS) Catalog from 22 February 2003 through 28 February 2003 (circles) on AZ and CI broadband stations (inverted triangles) and Station KNW, the highest quality station, used in this analysis (darkened triangle). Inset: ANSS catalog events during the swarm. The sequence had no activity prior to the mainshock, whereas aftershocks persisted for a few weeks.

While the mainshock was a strike-slip failure, the aftershock sequence produced varied focal mechanism including at least one moderate-size reverse-faulting event, some normal faulting, and failure on conjugate planes (Yang et al., 2012).

The continuous records were not saved for all stations at the time of the 2003 event, and the highest quality nearby station (KNW, part of the ANZA network) is approximately 60 km away from the center of the sequence. This station recorded nearly all of the earthquakes in the ANSS catalog. We use the vertical component of this station for our initial application of empirical subspace detection.

All available waveforms from a given station, on a given channel are used to select the optimal design set for the tectonic setting at hand. While multiple channels may be incorporated (Harris, 2006), we demonstrate the application as if only the vertical channel is available. Horizontal channels produce similar results; however, the lower signal-to-noise ratio of horizontal components makes them less useful.

Waveforms and related metadata for this data set are provided by the IRIS Data Management Center and obtained using the Standing Order for Data (Owens et al., 2004). Basic processing on the waveforms of ANSS cataloged events construct the subspace detector at the appropriate dimension: we arrange the window of interest to be 1 s before the automatically picked *P* arrival and included the following 11 s (which includes ~3 s of the *S* arrival), the mean of the signal is removed, a bandpass filter of 1-10 Hz is applied and a cosine taper is used on 5% of the signal on each end. Each event is cross-correlated pairwise, and then we perform an agglomerative, hierarchical, single-linkage cluster analysis on the waveforms. We selected the largest five groups with normalized cross-correlation coefficients of at least 0.875 to form the design set of earthquakes. This design set yields 66 waveforms (Figure 2-4). Using a master event (with high correlation value with respect to the rest of the design set) we define the lag times for P-wave alignment using cross correlation. We construct a matrix using these aligned waveforms with each seismogram comprising a row of matrix **A**.

We compare the application of the empirical subspace with two other detectors on the continuous seismic record in the week following the 2003 Big Bear earthquake. The first detector is the stack of the design set events, or average seismogram, normalized to unit length. This is used to represent traditional template matching methods or a one-dimensional subspace. The second is our empirical subspace detector; a matrix comprised of two rows: the stack and the time derivative of the stack. Although some empirical weighting would be appropriate (analogous to subspace vectors being weighted by their corresponding singular values), the vectors in this application are equally weighted. Reasonable amounts of weighting, such as values similar to the

relevant contribution of the singular values, do not product drastically different detection results. Weighting may be applicable in cases of more dispersed seismicity. In order to more closely approximate the theoretical subspace, we normalize each of the rows to be of unit length. The final detector is the two-dimensional subspace detector determined using the same design set under a singular value decomposition.

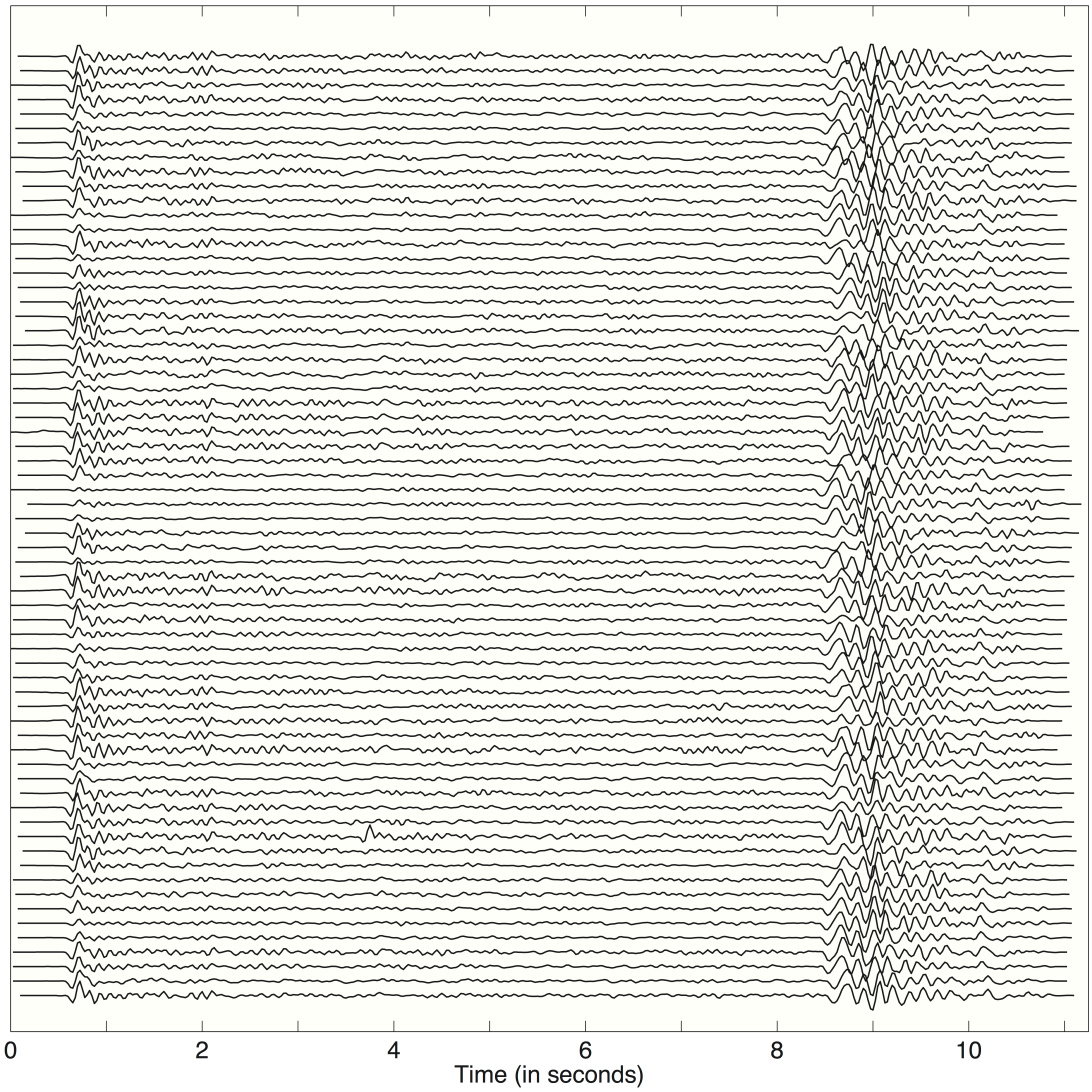

Figure 2-4. Waveforms of the 66 events in the design set cut 1s before to 10s after the *P*-wave arrival. Events are aligned through cross correlation to a master event on the *P*-wave arrival.

Each of the three detectors is used on the seven days following the Big Bear mainshock (the period equivalent to greater than 20 cataloged events per day). We process the continuous record from station KNW in an identical manner to the design set waveforms cut into windows of equal length and normalized to unit length. The dot product of each detector and the windowed continuous signal is computed (γ) at each sample in the time domain. Values above an empirically determined threshold are recorded as detections, compared with the ANSS catalog of events and finally verified visually.

Results

We compare the results of the three detectors (Figure 2-5) at a threshold of 0.125. The stack finds nearly all of the cataloged events as well as over 100 previously uncataloged events. The theoretical subspace detector finds more cataloged and uncataloged events; however the overall number of false detections increases slightly.

The empirical subspace detector finds the most cataloged events with a similar rate of false detection. The waveform of the events identified using the empirical subspace detectors are shown in Figure 2-6. Each of the detections are verified visually to have seismic characteristics consistent with the events originating in the Big Bear mainshock region including expected *P* and *S* arrival times and corresponding change in frequency content.

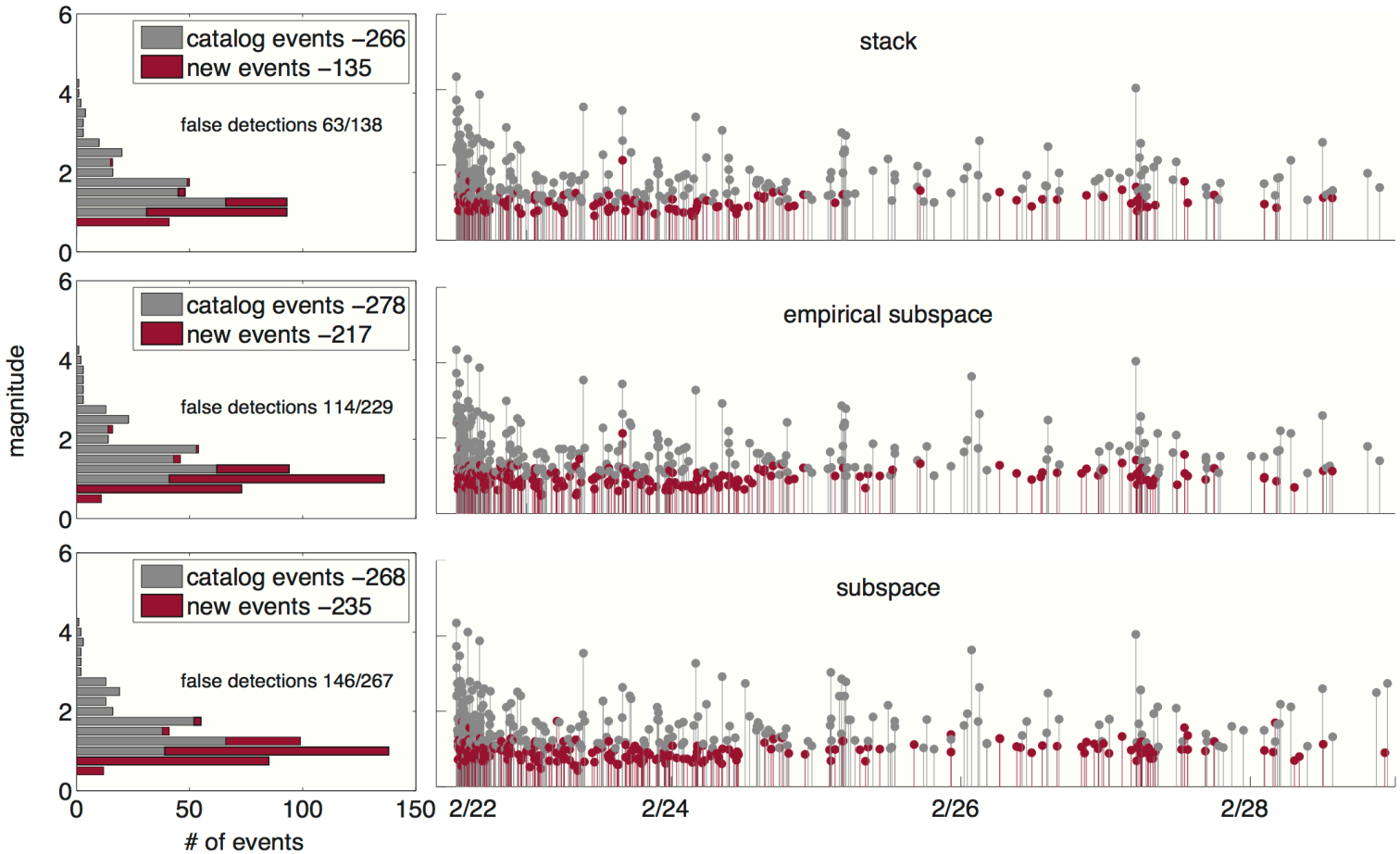

Figure 2-5. Results of the three detectors on one week of continuous data. (a) The results of the stack (representative of templates) detector. Left: distribution of cataloged (gray) and new (red) event detections, sorted by magnitude. False detections not automatically removed during processing are noted. (b) The results of the empirical (representative of a template and its derivative) detector. (c) The results of the 2D subspace.

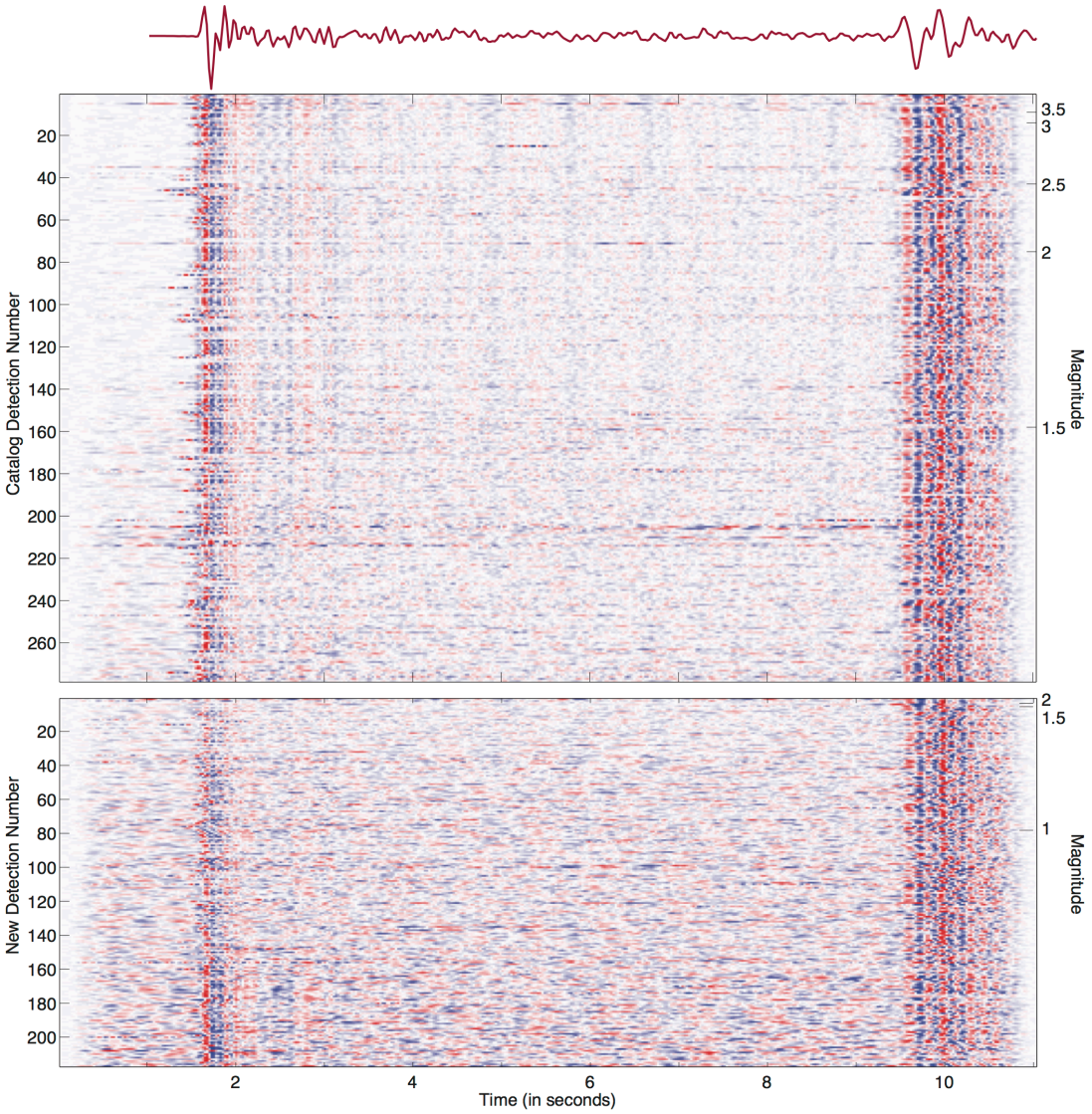

Figure 2-6. Waveforms of the detections made using the empirical subspace detector. The top trace shows the stack of the design waveform for reference. Waveforms are ordered by estimated magnitude. Middle box shows (278) events that were already apart of the CISN catalog. Lower box shoes new (217) detections, with false detections removed.

In considering the outcomes of a detection test, there are four possibilities:

1. No detection in a waveform that contains only noise or unrelated signal (correct null hypothesis)
2. A detection of relevant signal in a waveform of only noise (Type I error)
3. A detection where there is an event of interest (correct detection)
4. No detection where there is an event of interest (Type II error)

The template detector has a slightly lower percentage of Type I errors when compared to both subspace-based detectors (~19% vs. 23-24%). Exploring the use of a statistically (rather than empirically) determined detection threshold for the subspace-based detectors would mitigate these errors. Our empirically derived threshold (0.125) was based on the fractional energy capture analysis which is sufficient to represent, a least all the design set events using two-dimensions of the subspace. While adopting a higher detection threshold would decrease false detections; we prefer to tolerate Type I errors in order to detect the maximum number of earthquakes possible.

Each of the detectors show similar Type II error rates, missing the same number of ANSS cataloged events. We believe these missed detections are variations in focal mechanism and aftershock on perpendicular fault planes as observed by Chi and Hauksson (2006). For example, one early aftershock (m_L 4.5) was determined to have a reverse mechanism. Such a source would not produce a similar waveform that would be well represented by the subspace of singular vectors or the average of the design set, and thus its detection is not observed in any of our detectors. Variations in source are likely not represented by the explored subspace in this example.

We find that the empirical subspace detector succeeds in finding previously uncataloged events without substantially increasing the false detection rate. It performs at nearly the same detection rate as the theoretical subspace, but requires much less effort on the part of the seismic analyst. Of the 217 newly detected events using the empirical subspace, we see the addition of many smaller magnitude events ($m_L < 1.5$).

Another success of the empirical subspace is its detection of overlapping events, where the P-arrival of a second event obscures the arrival of the S-wave of an early, primary event. These earthquakes are most prevalent early in the seismic sequence and often are uncataloged since they occur within the coda of a mainshock, or large aftershock. This is particularly problematic in the case of energy-based detectors as

small events are obscured by larger amplitude waveforms. We observe several instances where the subspace-based detectors find overlapping events missed by the traditional template detector (Figure 2-7).

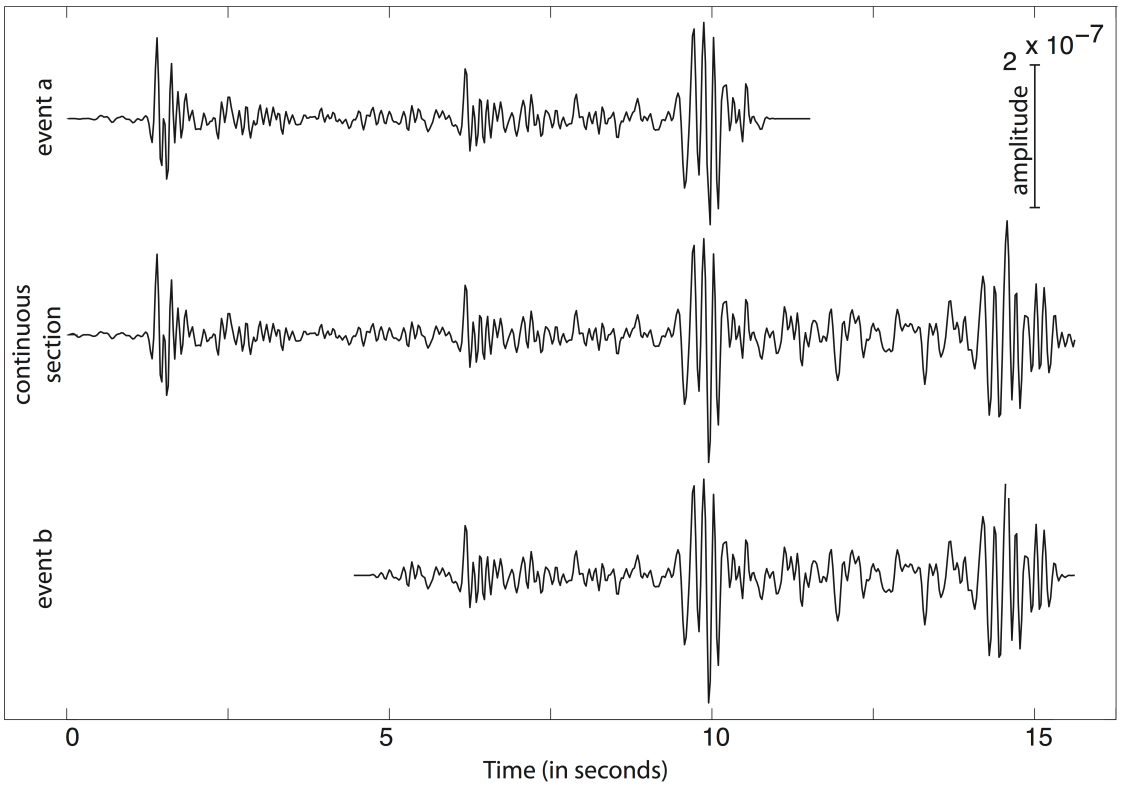

Figure 2-7. An instance of overlapping events (events a and b) detected by the empirical subspace method. The *P*-wave of event b arrives before the *S*-wave of event a. The top and bottom panels show the arrivals of each event. The center panel shows the continuous time series encompassing both events.

While the subspace-based detectors perform well in this application, they do have some disadvantages. In the case of a theoretical subspace, there is substantial work on the part of the seismic analyst assembling and constructing the design population of waveforms, although it could be possible to automate this process (Rowe et al., 2012). The selection of the design set is crucial to the ability of a detector to perform well across the events of interest. For example, as illustrated by the Type II errors, a selection of a simple design set is not optimal for a diverse population of events.

We propose that the empirical subspace might be utilized in a larger capacity. A matrix comprised of a template and its time derivative could be scanned through the continuous record in a method very similar to, but improving on, traditional template matching. This extra information contributed by the time derivative acts as an approximation for the second singular vector and allows for more variation in the templates, improving the detection of events that are similar, but not identical. It also eliminates the need to construct a design set or perform singular value decomposition. In the above application, using the empirical subspace we show a near doubling of new detections when compared to traditional template detection. A catalog of empirical subspace detectors has the possibility to increase the number of detection and decrease the number of errors further.

Conclusions

We find the empirical subspace to be a useful detector and have broad possible applications. In the above example, we use a station ~60km way from the Big Bear source region, showcasing the detectors usefulness in regions of sparse stations spacing. There are many regions of low background activity such as the Central and Eastern United States where station spacing is likely to remain sparse.

Application to the Bucaramanga Nest

The use of an empirical subspace detector can improve the completeness of the catalog at small magnitudes. This method is used to definite the detection probability of small magnitude earthquakes in the Bucaramanga Nest in Chapter 4.

References

Brown, J. R., G. C. Beroza, and D. R. Shelly (2008). An autocorrelation method to detect low frequency earthquakes within tremor, Geophys. Res. Lett. 35, L16305, doi: 10.1029/2008GL034560.

Chi, W.-C., and E. Hauksson (2006). Fault-perpendicular aftershock clusters following the 2003 Mw 5:0 Big Bear, California, earthquake, Bull. Seismol. Soc. Am. 33, L07301, doi: 10.1029/2005GL025033.

Gibbons, S. J., and F. Ringdal (2006). The detection of low magnitude seismic events using array-based waveform correlation, Geophys. J. Int. 165, 149–166.

Harris, D. (2006). Subspace detectors: Theory, Lawrence Livermore Natl. Lab. Rep. UCRL-TR-222758, Lawrence Livermore National Laboratory, Livermore, California.

Harris, D., and T. Paik (2006). Subspace detectors: Efficient implementation, Theory, Lawrence Livermore Natl. Lab. Rep. UCRL-TR- 223177, Lawrence Livermore National Laboratory, Livermore, California.

Jones, L. E., S. E. Hough, and D. V. Helmberger (1993). Rupture process of the June 28, 1992 Big Bear Earthquake, Geophys. Res. Lett. 20, 1907–1910.

Maceira, M., C. A. Rowe, G. Beroza, and D. Anderson (2010). Identification of low-frequency earthquakes in non-volcanic tremor using the subspace detector method, Geophys. Res. Lett. 37, L06303, doi: 10.1029/2009GL041876.

Owens, T. J., H. P. Crotwell, C. Groves, and P. Oliver-Paul (2004). SOD: Standing order for data, Seismol. Res. Lett. 75, 515–520.

Peng, Z., and P. Zhao (2009). Migration of early aftershocks following the 2004 Parkfield earthquake, Nat. Geosci. 2, 877–881.

Rowe, C. A., R. J. Stead, M. L. Begnaud, and E. A. Morton (2012). Seismic signal analysis for event detection and categorization, in 2012 Monitoring Research Review: Ground-Based Nuclear Explosion Monitoring Technologies 312–320.

Shelly, D. R., G. C. Beroza, and S. Ide (2007). Non-volcanic tremor and low-frequency earthquake swarms, Nature 446, 305–307.

Shelly, D. R., G. C. Beroza, H. Zhang, C. H. Thurber, and S. Ide (2006). High-resolution Subduction zone seismicity and velocity structure beneath Ibaraki Prefecture, Japan, J. Geophys. Res. 111, B06311–B06320.

van der Elst, N. J., H. M. Savage, K. M. Keranen, and G. A. Abers (2013). Enhanced remote earthquake triggering at fluid-injection sites in the midwestern United States, Science 341, no. 6142, 164–167.

Van Trees, H. L. (1968). Detection, Estimation and Modulation Theory, Vol. 1, John Wiley and Sons, New York.

Wessel, P., and W. H. F. Smith (1998). New, improved version of the Generic Mapping Tools released, Eos Trans. AGU 79, 579.

Yang, W., E. Hauksson, and P. M. Shearer (2012). Computing a large refined catalog of focal mechanisms for southern California (1981– 2010): Temporal stability of the style of faulting, Bull. Seismol. Soc. Am. 102, 1179–1194.

CHAPTER THREE:

Repeating and reverse polarity earthquakes of the Bucaramanga Nest

Repeating Earthquakes

Repeating earthquakes are phenomena that are observed in many different tectonic settings including subduction zones off the coast of Japan (Igarashi et al., 2003; Kimura et al., 2006), off the coast of Sumatra (Barrett, 2010) and the San Andreas Fault system (Nadeau and Johnson, 1998; Peng et al., 2005). Repeating earthquakes are generally thought to be recurrence of slip on a seismic patch and can be identified using seismograms or spectra, utilizing the assumption that slip on that patch will produce a nearly identical seismic wavefield. In this chapter, repeating events are identified by characteristics of their seismograms. Slip on an asperity in the Bucaramanga Nest produces a wavefield that when recorded on a given seismometer, produces a highly similar seismogram (Figure 3-1). In practice, the seismic records are not perfectly identical and the slight differences in the waveforms represent differences in the source parameters, source region or slight deviation from a similar path. Cross correlation, a measure of the similarity of two time series is used to quantify the similarity between two waveforms.

$$f \star g = \int_{-\infty}^{\infty} f^*(-\tau)\, g(t-\tau)\; d\tau \qquad \textit{equation 3-1}$$

Where f and g represent the seismograms from two candidate earthquakes. This produces a function of correlations at various lag times. If f and g are normalized to unit length, then a perfectly identical signal will have a coefficient of 1; while a perfectly opposite polarity signal will have a coefficient of -1. In general, most unrelated earthquakes have maximum correlation values from 0.1-0.3. Earthquakes from similar regions have slightly higher maximum correlation coefficients (in the range of 0.5-0.6). Repeating signals of related earthquakes (repeating earthquakes) tend to have much higher correlations (~0.95 Barrett, 2010) low frequency earthquakes have slightly lower, but still significant coefficients (~0.3-0.6; Shelly et al., 2007). For repeating earthquakes, the maximum of this function is recorded. For reasons that will be explained in the following sections, for our study of the Bucaramanga Nest, we also record the minimum of the correlation function.

Information gained from identifying repeating intermediate-depth earthquakes, such as magnitude and recurrence interval, can be used to quantify tectonic processes such as plate motions or post-seismic aftershock decay. There are several different varieties of observed repeating earthquakes (Figure 3-2).

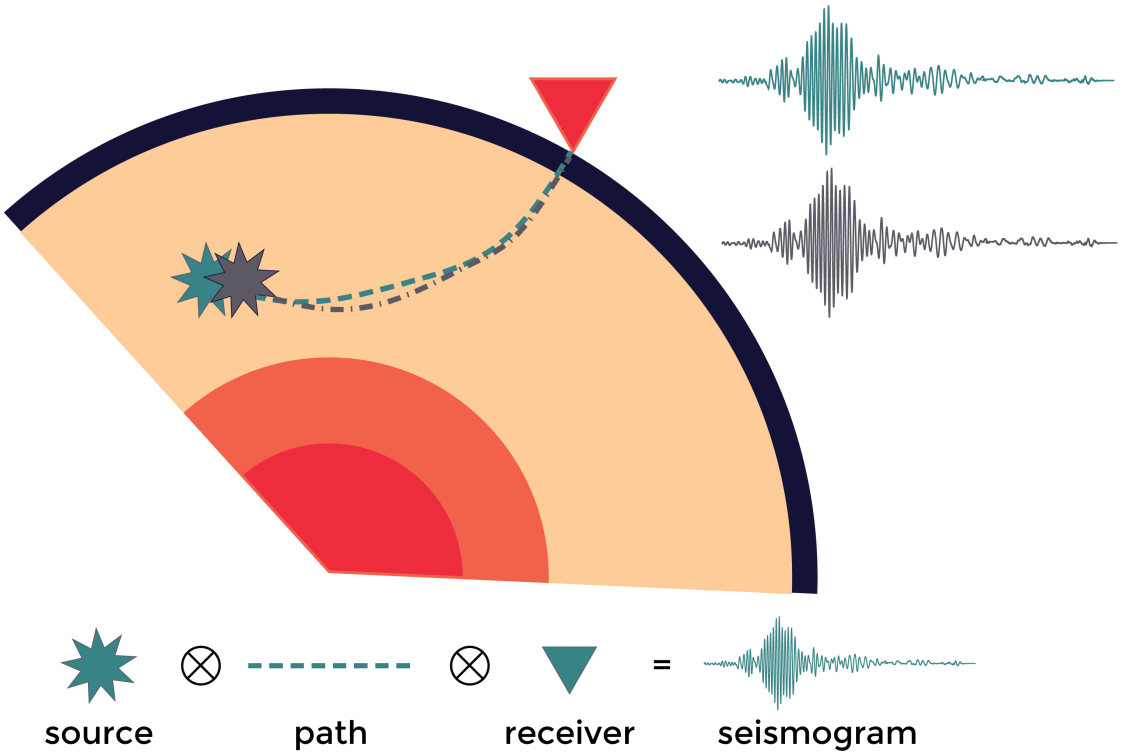

Figure 3-1. An illustration of the contributions to an earthquake's waveform from source to receiver in the context of repeating earthquakes. A seismogram can be represented as the convolution between the excitation effect of the seismic source, linear propagation via the Green's function (or ray path) and possibly nonlinear the site effects and the instrument response of the receiver to input ground motion. Two highly similar seismograms as recorded at a given station should have identical receiver components, and if they are co-located will have highly similar ray paths.

Repeating Earthquake types (burst, continuous, asperity)

Igarashi et al., 2003 identified two varieties of repeating earthquakes in their study of Pacific plate subduction off the coast of Japan. The first, continuous-type repeating, earthquakes are perhaps the most commonly thought of variety. These earthquakes occur with relatively consistent recurrence intervals, magnitudes and with focal mechanisms indicative of the plate boundary.

Burst-type repeating earthquakes commonly occur as part of aftershock sequences and likely occur on pre-existing fault planes, not necessarily consistent with the plate boundary orientation (Kimura et al., 2006). Like other aftershocks, they generally follow Omori type decay in recurrence interval (Schaff et al., 1998), the focal mechanism is more likely to vary.

A third, hybrid type, of repeating earthquakes is similar to burst-type, and was identified in the aftershock sequence of the 2004 Sumatra megathrust. They are similar to burst-type in that they are apart of an aftershock sequence and have increasing recurrence intervals, but are also like continuous-type repeaters as they have a highly similar focal mechanism as the mainshock or plate boundary and occur on the plate boundary interface. The size of these events can decrease with increasing recurrence interval. While this contradicts popular hold-time fault rupture processes (Dieterich and Kilgore, 1994), this is likely a result of a rapidly changing regional strain rate. There is also evidence for this earthquake behavior along the Calaveras fault (Peng et al., 2005).

A new type of repeating earthquake, the reverse polarity-repeating earthquake is introduced in this thesis.

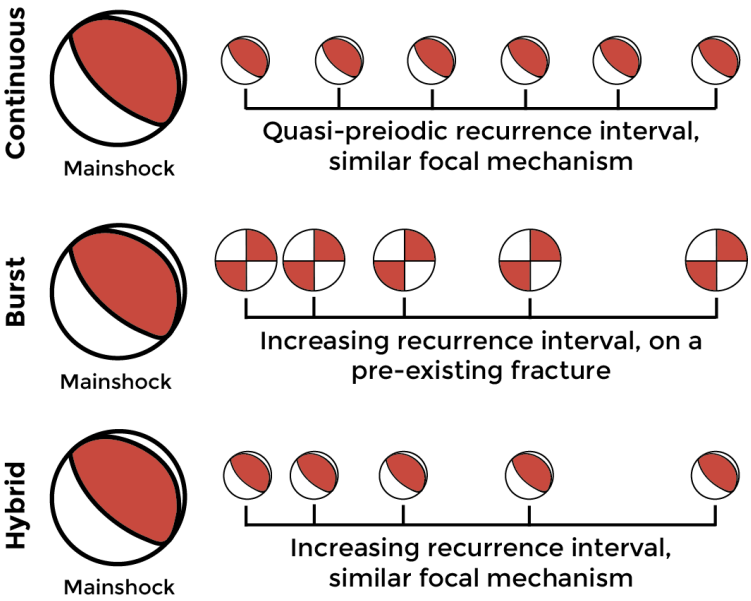

Figure 3-2. A cartoon of various documented types of repeating earthquakes. Continuous type repeaters occur regularly in similar locations, of similar magnitude and on regular recurrence intervals. Burst type events are generally associated as aftershocks and might be on pre-existing faults. A hybrid type observed after the Sumatran megathrust have similar focal mechanisms to the plate boundary but have increasing recurrence intervals over time. Modified from Barrett 2010.

Relative locations of repeating earthquakes

Repeating earthquakes are identified based on the assumption that closely located events with have highly similar source-to-receiver paths, producing highly similar

waveforms. Slight variations in these waveforms, among other things, suggest small differences in the source location. The size of a circular earthquake rupture of small to moderate size can be estimated from an assumed stress drop (Eqn 3-2, e.g. Brune, 1970).

$$Radius = \sqrt[3]{\frac{7}{16}\frac{M_o}{\Delta\sigma}} \qquad \textit{equation 3-2}$$

Using this information, together with highly precise location, we can infer if a repeating event ruptures the same patch or if there is a very small separation between events (near repeating; Figure 3-3).

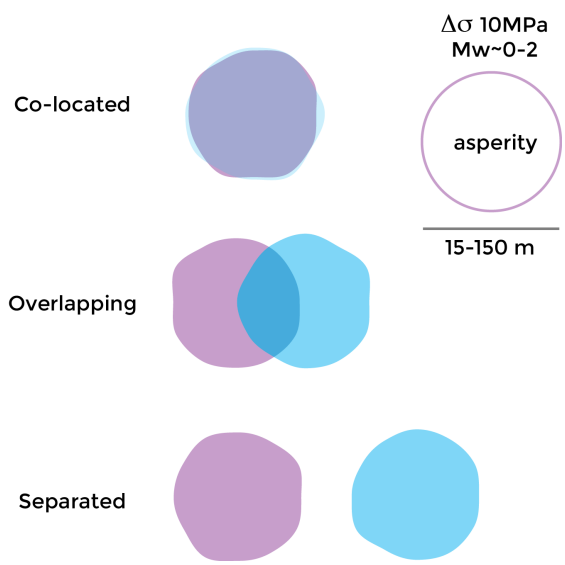

Figure 3-3. An illustration showing the possible arrangement of repeating, or near-repeating earthquakes. Repeating earthquakes are generally associated with the asperity model of earthquakes-implying that repeating events fail on the same "patch" surrounded by aseismically creeping region. The size of the asperity is inferred from the magnitude and assumed stress drop.

Seismicity in the Bucaramanga Nest & the Colombian Seismic Network

In the past decade, the Colombian National Seismic Network (RSNC) increased the number of number of 3-component short period and broadband stations in their network. Additionally, many instruments now feature sampling rates of 100 Hz. This increase in instrumentation resulted in tens of thousands of arrival times acquired from and broadband data since 2002. Currently, the catalog is complete to ~M 2, a metric that is further explored in Chapter 4. This catalog provides an extensive resource to

study the Bucaramanga Nest, which has ~8,000 earthquakes a year in the RSNC catalog.

Table 3.1 Parameters of the Bucaramanga Nest

Earthquakes per year	8,000
Frequency	1 earthquake per hour
Largest earthquake since 2000	M 6.2 (March 2015)
Estimated nest dimension	8 x 4 x 4 km

As mentioned previously, the Bucaramanga Nest is the smallest and most active (in terms of moment release per volume) of the primary earthquake nests. The earthquakes are of varied focal mechanism and size, and are known to occur within an extremely small volume 11 km^3 (Frohlich et al., 1995). While the possibility of moment tensors with significant isotropic or non-double-couple components are frequently brought up in the literature, most of the nest earthquakes exhibit a double-couple mechanism, with little to no isotropic or compensated linear vector dipole (CLVD) component. The highly varied focal mechanisms of the Bucaramanga Nest have been noted by several previous studies (Schneider et al., 1987; Cortés and Angelier, 2005).

The Bucaramanga Nest produces many repeating earthquakes, as well as repeating events with perfectly reversed polarity. We call this population of events, anti-repeating, or reverse-polarity repeating earthquakes. The records of reverse polarity repeats are highly similar, once the polarity of one event has been reversed (Figure 3-4). The nest also produces earthquakes that do not appear to repeat (or anti-repeat). Temporal or spatial changes in these populations might provide indications of failure mechanism or other source parameters.

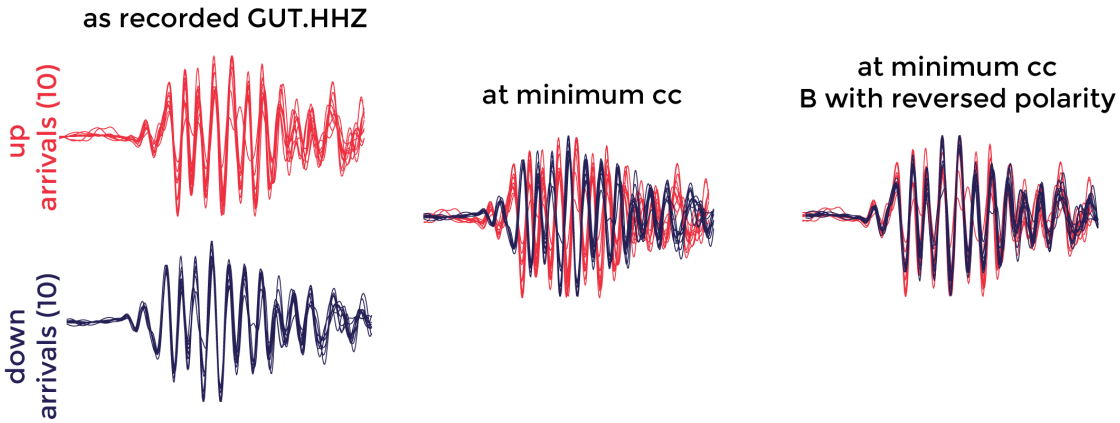

Figure 3-4. The Bucaramanga Nest contains several families of repeating events (red, blue). A group of 10 events in each of these families are shown on the left panel. The center panel shows the two groups plotted aligned at their minimum cross correlation. The final panel shows the alignment at the same time, but with the polarity of the blue family reversed.

While apparent polarity reversal may occasionally occur as an artifact of station maintenance, the signals we observe are genuine as they persist through long periods of time, and the patterns of occurrence frequently change from one group to the other (and back), and are recorded across the network in a consistent manner (Figure 3-5).

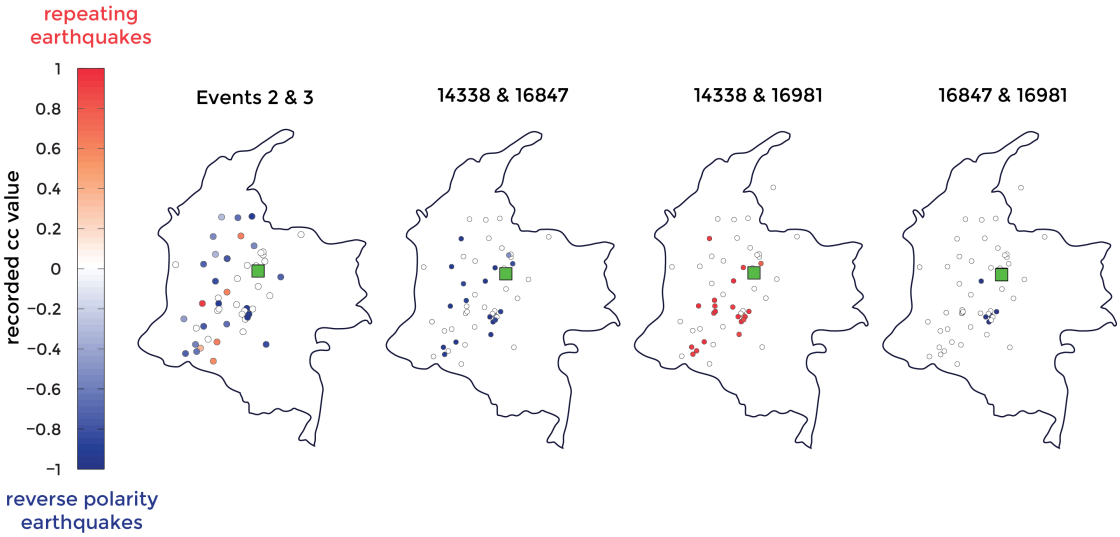

Figure 3-5. Cross correlation values of various earthquake pairs, as recorded across the Colombian Seismic Network. The outlined region represents the borders of Colombia, each station is indicated by a circle and is shown to be red when the events have high positive correlations, blue when they have high negative correlations and white when the correlation is indistinct or one of the events was not recorded at that station. The Bucaramanga Nest is indicated with a green square. For the most part, stations are consistent in the sign of the correlation value between two events.

Repeating earthquakes can be identified and categorized using their correlation coefficients through cluster analysis.

Cluster Analysis

Cluster analysis is a useful method of classification that is used widely across many fields of study. In this application, earthquakes (represented by their seismograms) represent members in a set. Since characteristics of the seismogram will vary based on path differences, each station's records are analyzed separately. Waveforms show similarity and dissimilarity that allows for the judgment of how closely a given earthquake is related to each other earthquake in the set.

The options for cluster analysis methods are numerous. The focus in this application is on hierarchal methods, which are particularly useful as they do not require an initial number of clusters, as do partitioning methods (such as the popular *k*-means clustering). In most fields, the popular methods of cluster analysis are offshoots of agglomerative hierarchal methods, further subdivided by the measure of similarity distance between events (Blashfield, 1976). In agglomerative methods, clustering begins with *n* clusters (where *n* is the total number of elements in the set) and finds the most similar element or cluster to link. The first step must consider all possible links between two elements in the set:

$$C_n^2 = \frac{n(n-1)}{2} \qquad \textit{equation 3-3}$$

This process continues until the final step where all elements are part of a single cluster.

While agglomerative methods are useful, we introduce the idea that *a priori* knowledge of the Bucaramanga Nest calls for a different approach. Rather than an agglomerative method, we introduce the use of a simplified divisive method. Divisive clustering is by definition hierarchical and proceeds inversely from agglomerative. At each iteration, a cluster is split into two smaller groups until each group contains a

single element. Divisive clustering methods are often overlooked due to their intensive computational requirements. In the first step, the division of all members into two subsets must be considered. This scales as:

$$C_n = 2^{n-1} - 1 \qquad \textit{equation 3-4}$$

where *n* is the number of elements.

This problem scales much faster than the agglomerative case (which scales quadratic ally). For just 100 events, there are ~6 x 10^{29} possible divisions for the first step alone. This is considerably larger than in the agglomerative case, which has ~5000 possible first links (equation 3-3).

The method of cluster analysis must fit the application and *a priori* knowledge of the situation can be used to select the appropriate technique. In Bucaramanga, we have some idea that events will divide into a repeating group (A) and a reverse-polarity repeating group (B), with a possibility of a null set that doesn't easily fit into either group (N). For our purposes, it would be useful to divide events into these three event, so we adopt a divisive clustering approach, but with a modification to avoid large computations. We use the known dissimilarity between earthquakes to begin the division into A and B groups, thereby eliminating the computationally expensive first step. We then use linkages, in a similar process to agglomerative clustering to further subdivide events into each group, and then divide that group into smaller deviations.

In practice, elements are measured by their dissimilarity to one another. The method of calculating this distance, known as "linkage," plays an important role in establishing clusters. The metric of this distance can be varied in certain applications; however, the most popular option, Euclidean distance is appropriate in this case. While many options of linkage method exist, single-, average-, and complete-linkage are the most

popular and appropriate options (Figure 3-6). Single linkage, or nearest neighbor, searches for the smallest distance between an element of P and Q:

$$d\,(P,Q)$$

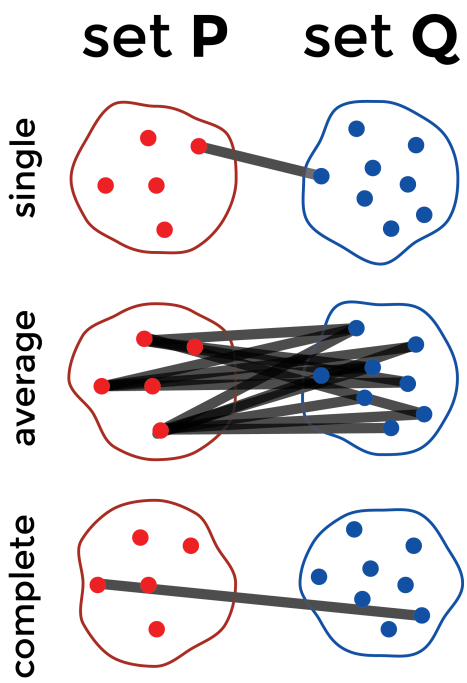

Figure 3-6. Different methods of linkage in cluster analysis. Single linkage finds the smallest distance between any two events. Average linkage finds the average (mean) distance between elements in each set. Complete linkage uses the maximum distance between any members of the set. (After Kaufman and Rousseeuw, 1990).

Where P and Q might be single- or multi-element clusters. This is a useful way to find highly similar elements; however it susceptible to chaining phenomena. This process occurs when two clusters have member elements that are close to one another, but not necessarily the entire group. The two clusters can link because of these similar elements, resulting in a long chain of events of which some members may be highly dissimilar.

Average-linkage is the primary rule used in this application. In this method $d(P,Q)$ is taken to be the average of all dissimilarities between the elements in P and Q. An average-linkage process can also be weighted in appropriate situations, although the unweighted average distance (UPGMA) is used in this application. Other methods of linkage such as compete (or farthest neighbor), weighted center of mass distance (median), and inner squared distance (ward) were also tested but not used.

The groups formed in cluster analysis can be visualized in a dendrogram (Figure 3-7)

Two Families of Repeating Earthquakes

We begin by investigating a set of earthquakes known to be repeating or anti-repeating. After an earthquake of 3.5 we look at the following three hours for aftershocks, yielding 92 candidate events. We take this subset of earthquakes and cross correlate each earthquake pairwise (n*(n-1))/2 pairs) at all available stations on all available components. We only consider the vertical component for purposes of clustering earthquakes as not all stations are three-component and the signal-to-noise ratio on this channel is higher.

A note on "missing" data

The correlations performed between events in this chapter are pairwise. In the operation of seismic networks there are often dropouts or interference that can sometimes lead to a station not recording an event (here an event record is defined as a pickable *P*-arrival or *S*-arrival). In a matrix of correlation values, this can be remedied by deleting the pair (pairwise deletion) or by mean substitution where the missing data point is replaced by the mean of all correlations. While this keeps the data consistent, it decreases the variance of the variable, which can be problematic in later analysis. In cases where one member of a correlation is absent at a given station, we replace this correlation value with NaN (effectively, pairwise deletion) so as to not distort the statistics of the correlation coefficients.

Furthermore, we check the statistical distribution of correlation values between event pairs at all stations that record both events to ensure the divisions were correct.

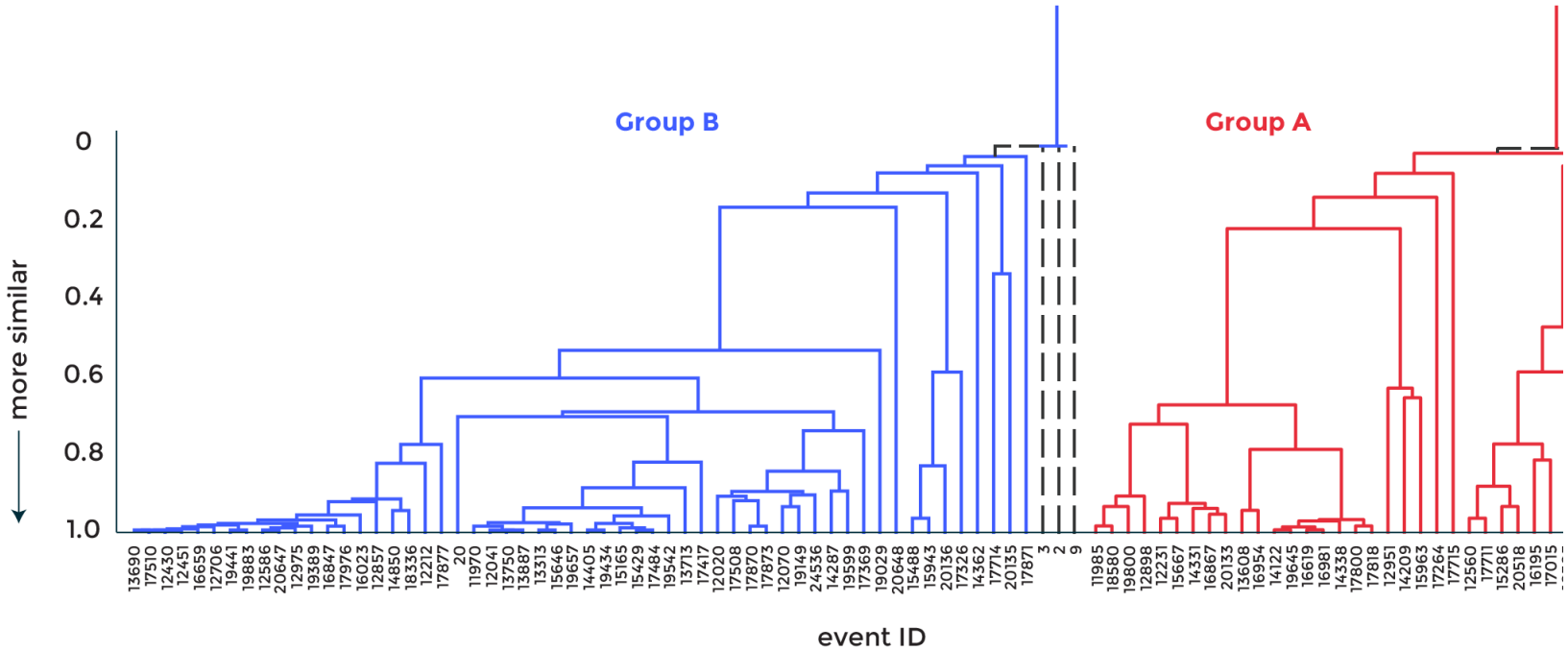

Figure 3-7. An example dendrogram based on average-linkage correlation values recorded at station GUT. This example shows an agglomerative method. Two distinctive groups emerge, one associated with Group A (red) and the other with Group B (blue). This station records most, but not all events. Those events that did not have arrival picks at station GUT are shown as dashed lines and their membership in a group is not considered meaningful. More similar events branch lower on the y-axis, while the initial divide between the two groups is shown to be lower than 0 correlation (since the groups have anti-correlations with one another).

A note on the statistics of correlation values

It is important in correlation statistics to note that in the case of centered data, correlation coefficients cannot be averaged, as they are not additive. The initial distribution of cross correlation coefficients is not normal because we are correlating seismic events with each other, and not including correlations with noise. In order to obtain certain statistics (such as the average, or mean correlation value), a conversion to Z-scores using the Fisher Transformation (Equation 3-5) is necessary. This extends the distribution from the limits of correlation coefficient from -1 to 1, as well as creates a normally distributed variable.

$$Z = \frac{1}{2}[\ln(1+r) - \ln(1-r)] = \frac{1}{2}\ln\left[\frac{(1+r)}{(1-r)}\right] \qquad \textit{equation 3-5}$$

r – correlation coefficient

These values are additive, so an arithmetic mean (or median) can be computed. This equation can be written in terms of average Z score ($\bar{Z}$) and inverted to obtain an equation for the mean correlation function (Faller, 1981), also referred to as the Fisher weighted mean value.

$$\bar{r} = \frac{e^{\bar{Z}} - e^{-\bar{Z}}}{e^{\bar{Z}} + e^{-\bar{Z}}} \qquad \textit{equation 3-6}$$

We look at the relationship between all event pairs by investigating the distribution of the Z-scores as recorded at stations in the RSNC network. As before, missing correlations are treated as NaN values. We look at both the maximum correlation coefficient and the minimum correlation coefficient for the event pairs and examine the distribution of z-scores as boxplots (Figure 3-8). We find that the median of this distribution correctly identifies the sign of the relationship between two events (+1 for positively correlated, repeating earthquakes and -1 for negatively correlated, reverse polarity repeating earthquakes). The sign is used to distinguish if the maximum or minimum correlation coefficient between two events is recorded as +1 for maximum

and -1 for minimum. Once an event pair is defined as a repeat or an anti-repeat, the corresponding coefficient is assigned across all stations in the network. This eliminates some true variation in the data as shown in Figure 3-5, however this noise could be a result of receiver site effects or slight variation in focal mechanism that should not influence the overall classification of an event.

For each station we consider the cross correlation matrix of each earthquake with every other earthquake. Since we know *a priori* this data set contains two distinct populations of earthquakes, we chose to implement a modified divisive clustering procedure. To avoid the large computational costs associated with the initial step of divisive clustering (eqn 3-4), we find the event pair with the lowest average correlation value across all stations. This event pair becomes the seed events for each start group (A) and (B). Next, the distances of the remaining events are checked with each seed event. The event with the shortest average distance across all stations joins one of the two groups. The correlation values of the groups are recalculated to include the contributions of the new element. These two steps are repeated until all events fit strongly with group (A) or (B), or are left as part of a null set (N) recorded in Appendix A. Visually, waveforms of these groups are consistent and correlate strongly with each other (Figure 3-9).

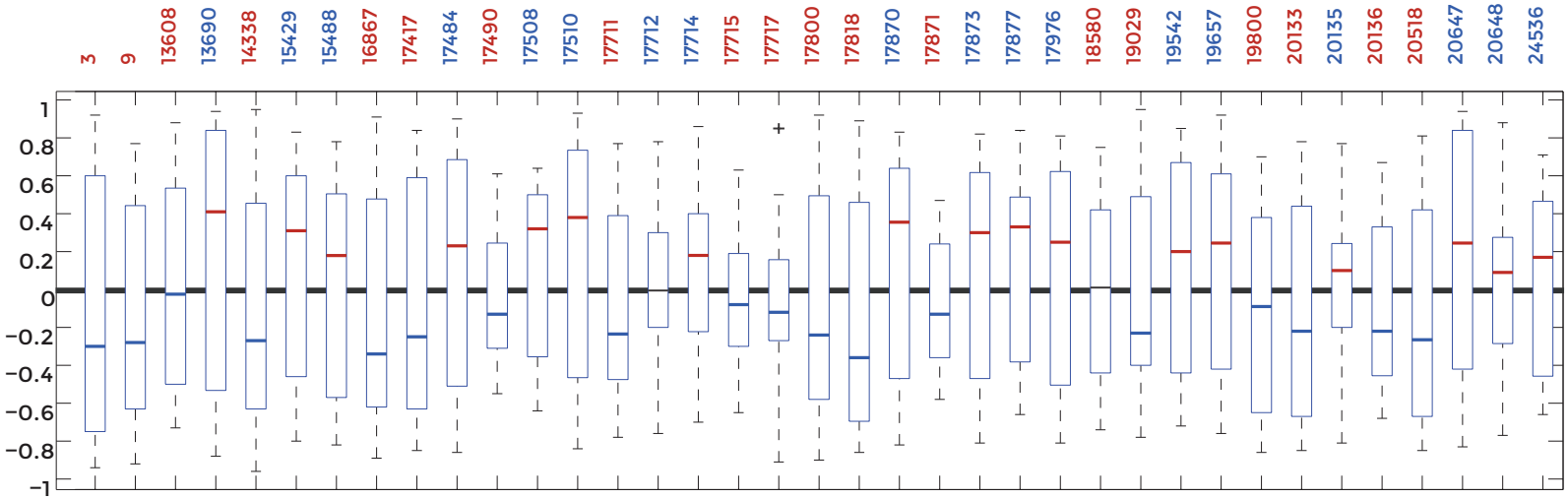

Figure 3-8. Distribution of all Fisher Weighted z-scores transformed from the minimum and maximum cross correlation values as recorded on the RSNC network stations. Events are shown if there is a minimum of 40 observations with Event 2. Positive median values are shown in red, while negative values are shown in blue. The events are color coded by their eventual membership in either group A or group B.

Figure 3-9. Example waveforms from Group A and Group B. Each group of events correlates highly within the group (repeating earthquakes), yet they are nearly the reverse polarity of each other. The waveforms of three instances of each group are shown at three temporary broadband stations. The center panel shows ten events of each group, at the same stations, stacked.

We can measure the consistency of an event grouping by investigating event triplets. That is, we check that if N and M have positive correlations with each other, and negative correlations with P, then N and M should be members of group A and P a member of group B. We find that these triplets are consistent to ~70%. A few events lower this number substantially, if only 2-3 of the most inconsistent events are removed, the consistency increases ~10-15%. We also check that the starting event pair does not play a major role in how groups are divided. We find that if we start with two negatively correlating events with a sufficient number of correlations, we obtain nearly identical results. The small variation in these groups largely stems from whether or not an event is included in the null group (N) or a set group (A or B).

Once groups are established, we seek to define precise locations of each group and assess if they are on similar or related structures.

Double Difference Relocations

HypoDD uses differential arrival time data to resolve precise relative locations among earthquakes (Waldhauser and Ellsworth, 2000; Waldhauser, 2001). The process exploits the slight differences in waveforms of closely located earthquakes by assuming the majority of a path to a given station is similar. Also, by using the same station, site effects can be neglected. For two earthquakes (i and j), as observed at a given station (k) we attempt to minimize the residual between the predicted travel time and the observation at station k. The difference in the residual for each earthquake yields a double difference:

$$dr_k^{ij} = \left(t_k^i - t_k^j\right)^{obs} - \left(t_k^i - t_k^i\right)^{calc} \qquad \textit{equation 3-7}$$

Using this information, we form a matrix, **G** with rows equal to the number of double-differences and columns equal to four times the number of events (a location: x, y, z; a time: t) and invert for locations. Using many events at many stations, we can use the relative arrival times (of both the *P* and *S* waves) in the inversion, using correlation coefficients to weight the reliability of each observation. If the data set is sufficiently large a solution of the system of equations using a singular value decomposition (SVD) may become computationally infeasible, and a conjugate-gradient method (LSQR) can be used instead; however, we choose to use the SVD in the inversion as it produces estimates of errors, in the linearized approximation of the relocation data without further analysis. These errors can be used later to assess the quality of the results and to condition subsequent feature extraction methods.

To ensure the inversion is robust, we test various initial event locations (Figure 3-10). The first case uses the initial RSNC catalog locations; the next uses the catalog longitude and latitude, but uses a single depth; another places all events at the center of the nest; and the final case uses random locations within the boundaries of the nest region. In all four cases, highly similar relocations are produced.

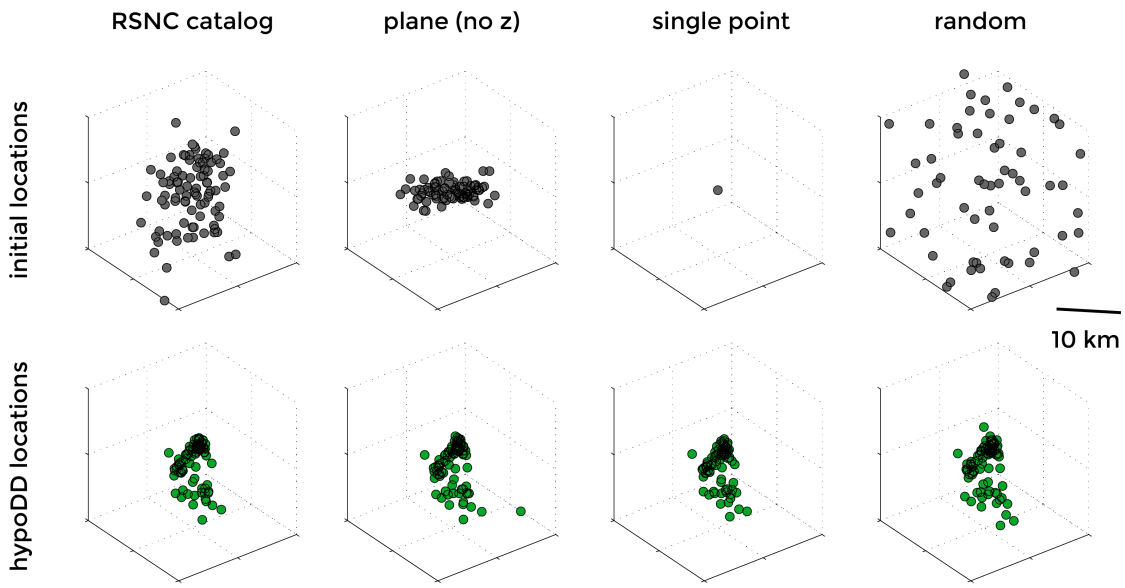

Figure 3-10. Various initial input locations to hypoDD (upper panel) are shown to produce nearly identical relocation results. The first column shows the RSNC catalog locations, the next shows events with no vertical spread, the third begins all events at the mean location of the nest, and the final test has random locations, far more disperse than the catalog locations. Since similar relocations are recovered in all cases, we feel the inversion is robust.

Incorporating the information from the divisive analysis into the hypoDD relocation reveals a loose separation of events within the A group and B group (Figure 3-11). While these relocations hint at an underlying structure, we attempt to utilize information in the errors produced in the SVD determine the extent to which we can collapse the locations on lower dimensional features to the extent allowed by location uncertainty.

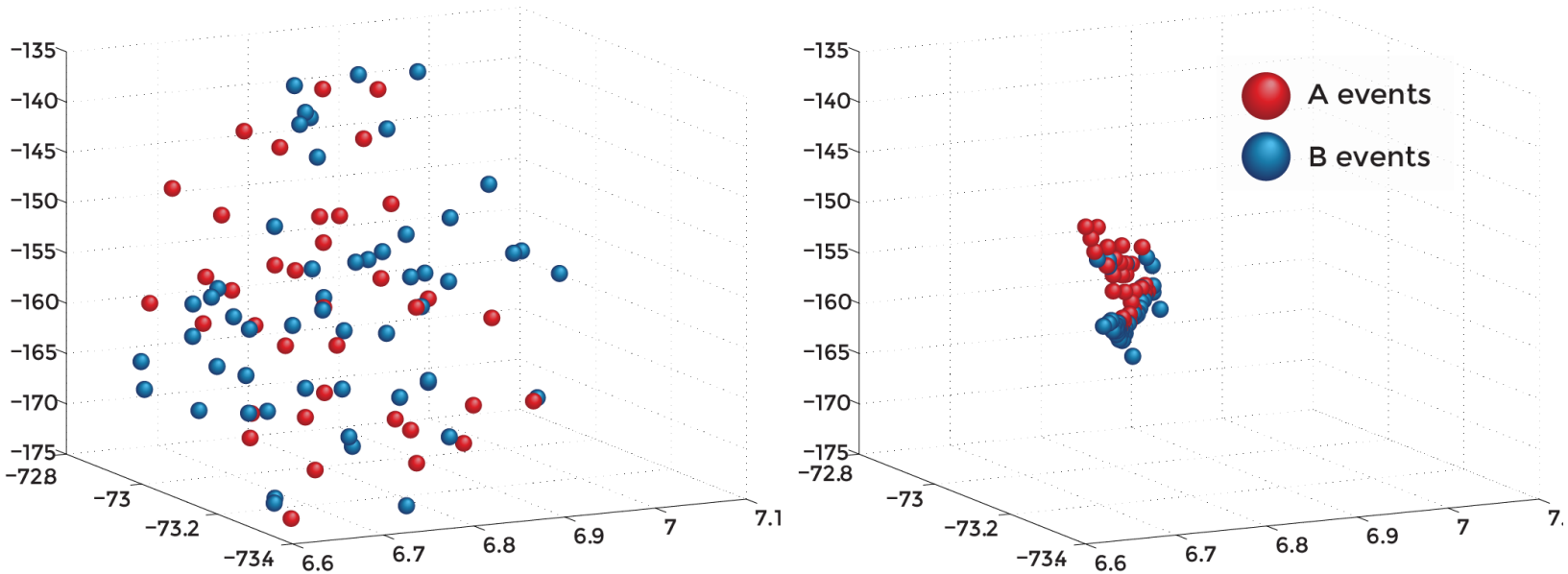

Figure 3-11. The left panel shows the initial RSNC locations, the right shows the hypoDD relocations of the same earthquakes. Group A events are shown in red, while Group B events are blue. While the two groups begin to separate in the hypoDD case, a feature extraction algorithm further improves the visibility of underlying structures.

Feature Extraction Relocation

The SVD inversion in hypoDD produces relocated events with meaningful corresponding errors. The feature extraction method of relocation (sometimes called "cloud collapse"), introduced by Jones and Stewart (1997) uses these errors to condition an additional step of feature extraction. This process can condense a diffusive cloud of seismicity to a simpler underlying structure.

The assumption in this method is that earthquakes generally occur along simple structures (usually points, lines or planes). The errors determined above provide the dimensions of a confidence ellipsoid (Figure 3-12), within which an event is likely to be located. In many cases, these ellipsoids can overlap, yielding a region of high probability. The method employed in this chapter attempts to condense seismicity to a simple point.

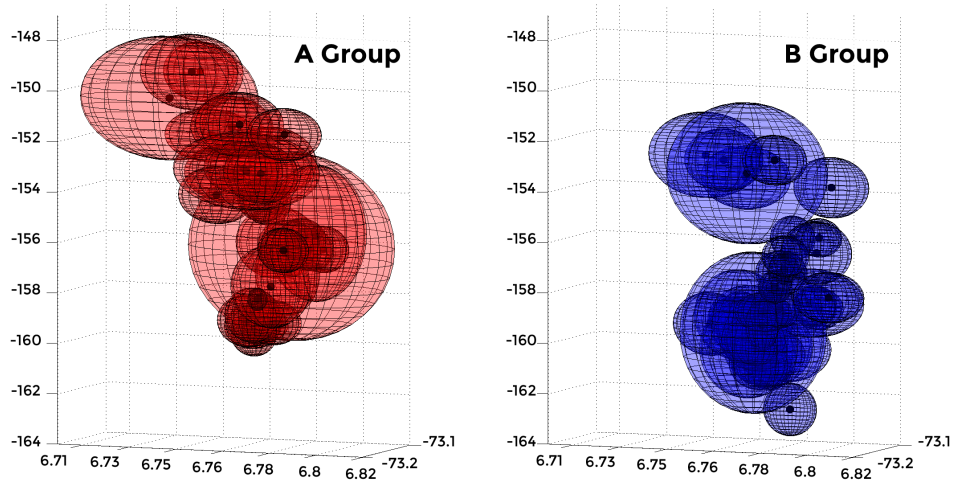

Figure 3-12. The singular value decomposition option of hypoDD produces meaningful errors in event location. These errors are plotted as ellipsoidal regions, centered on the relocated events. A and B groups are shown separately for clarity, but on the same scale.

In this step, hypoDD relocations are loaded as the initial locations. The size of the error ellipsoid is determined by a constant α * errors. Various values of sigma were tested (Figure 3-13) before selecting α=4. Since events of group A and B are

inherently different (one with positive first motion, the other with negative first motion), we use feature extraction on these events separately. This step is important since unlike in the case of hypoDD, the feature extraction does not account for waveform similarity in its locations. This step is justified since the separation between the two populations emerges in the hypoDD relocation and by nature of the algorithm, feature extraction of all events would produce a single structure removing that outcome in a later step. Feature extraction of all events at once does yield a single structure, which is interesting; however, the mechanics of a single fault that would be able to slip with reversed motion in the same location would be difficult to understand. The result of the separated feature extractions on the A and B group populations are shown in Figure 3-14. The two groups are separated by roughly 5 km. This distance should be sufficiently large to eliminate the possibility of overlapping rupture areas between the two structures. The movements of each event from hypoDD to final feature extraction location are detailed in Figure 3-15.

As the two structures are relatively linear, we can fit lines to the cloud of seismicity (Figure 3-16). Since the algorithm attempts to minimize structures to a point, we believe the recovery of a linear feature represents a true geometry.

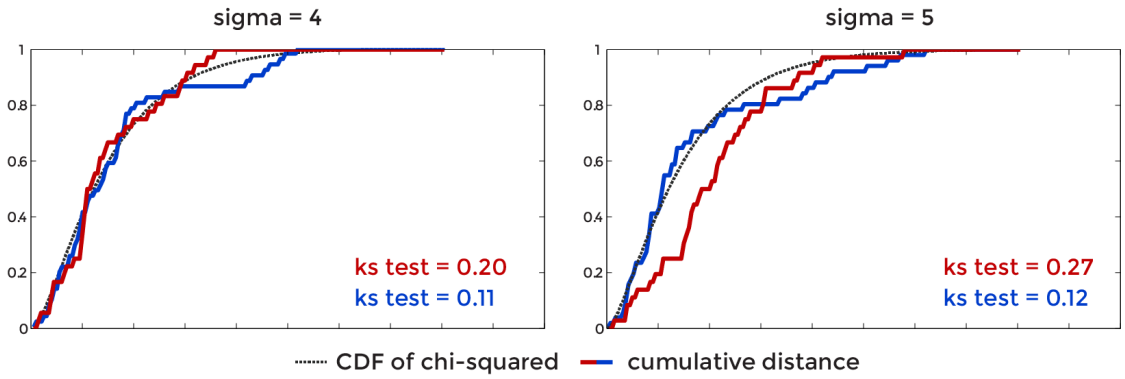

Figure 3-13. Fits to a chi-square cumulative function (dashed gray line) for groups A (red) and B (blue). The data is fit well at sigma =4, while sigma = 5 slightly over fits.

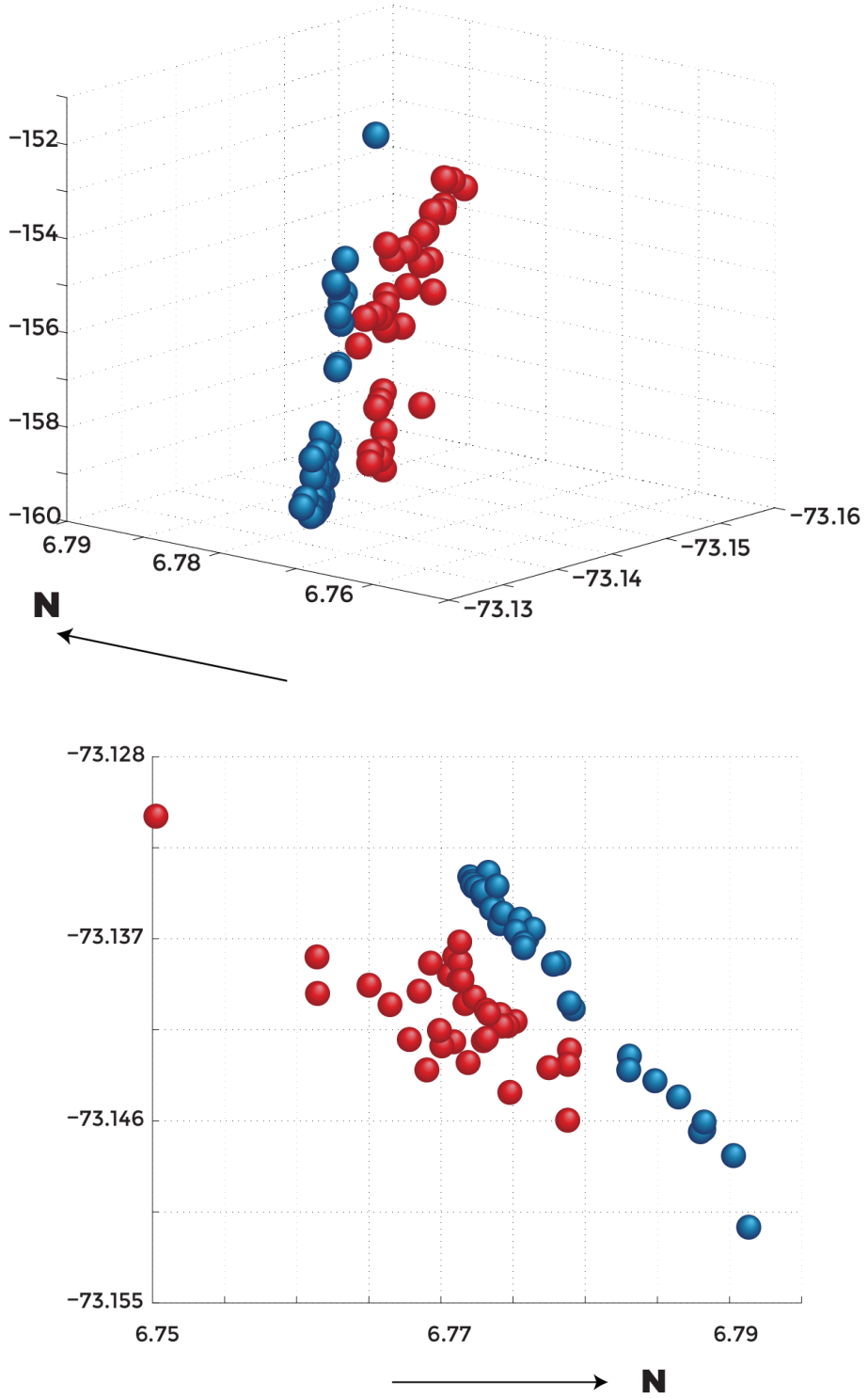

Figure 3-14. Various views of repeating and reverse polarity repeating earthquake groups as relocated using a feature extraction process. Two roughly linear features are recovered, each corresponding to a repeating group of earthquakes.

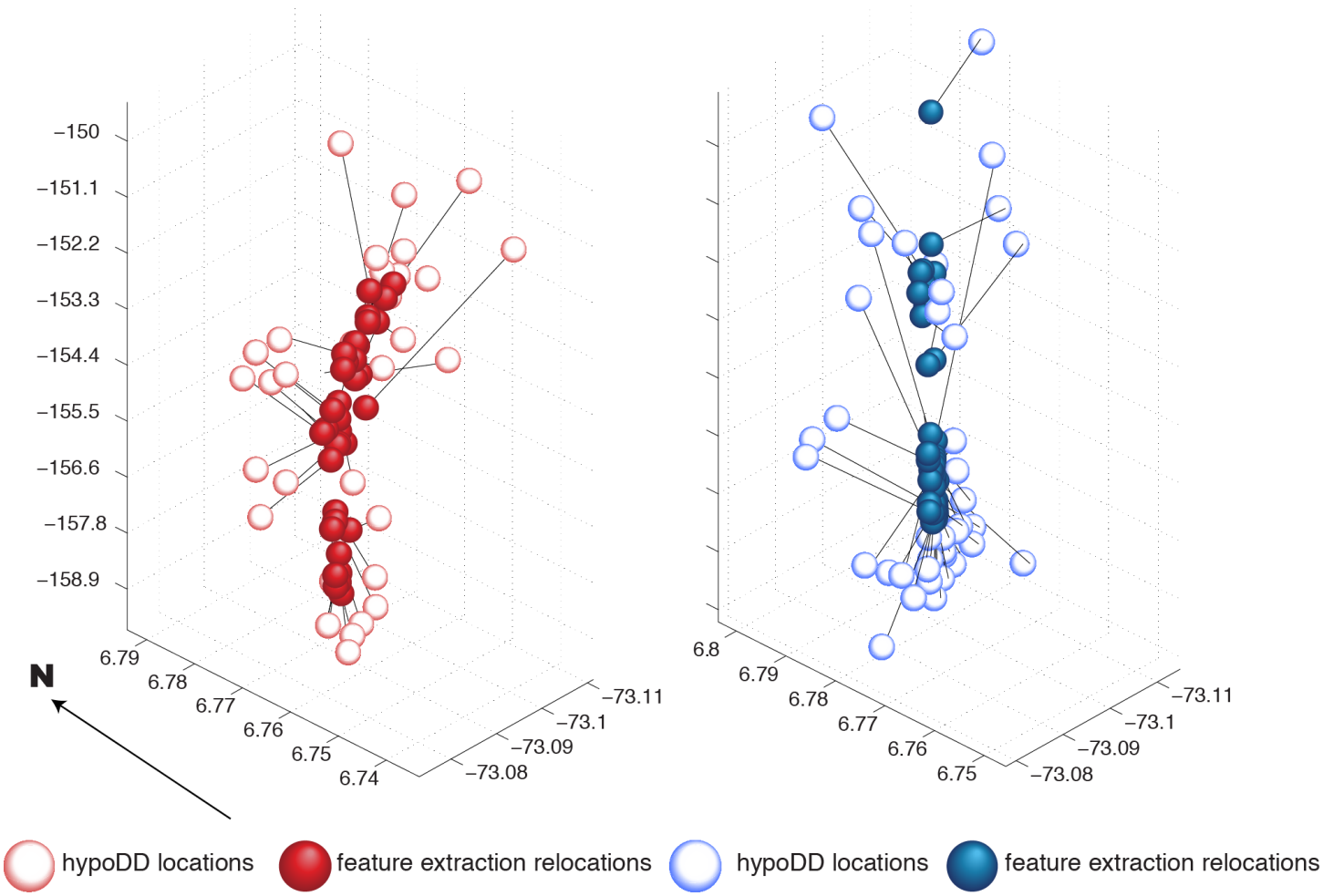

Figure 3-15. Changes in earthquake location from hypoDD relocations to feature extraction relocations for A group (left) and B group (right). The feature extraction process attempts to condense a cloud of seismicity to a single point. The fact that the seismicity collapses to a line in each case means that this aspect of the seismicity distribution is resolved by the data.

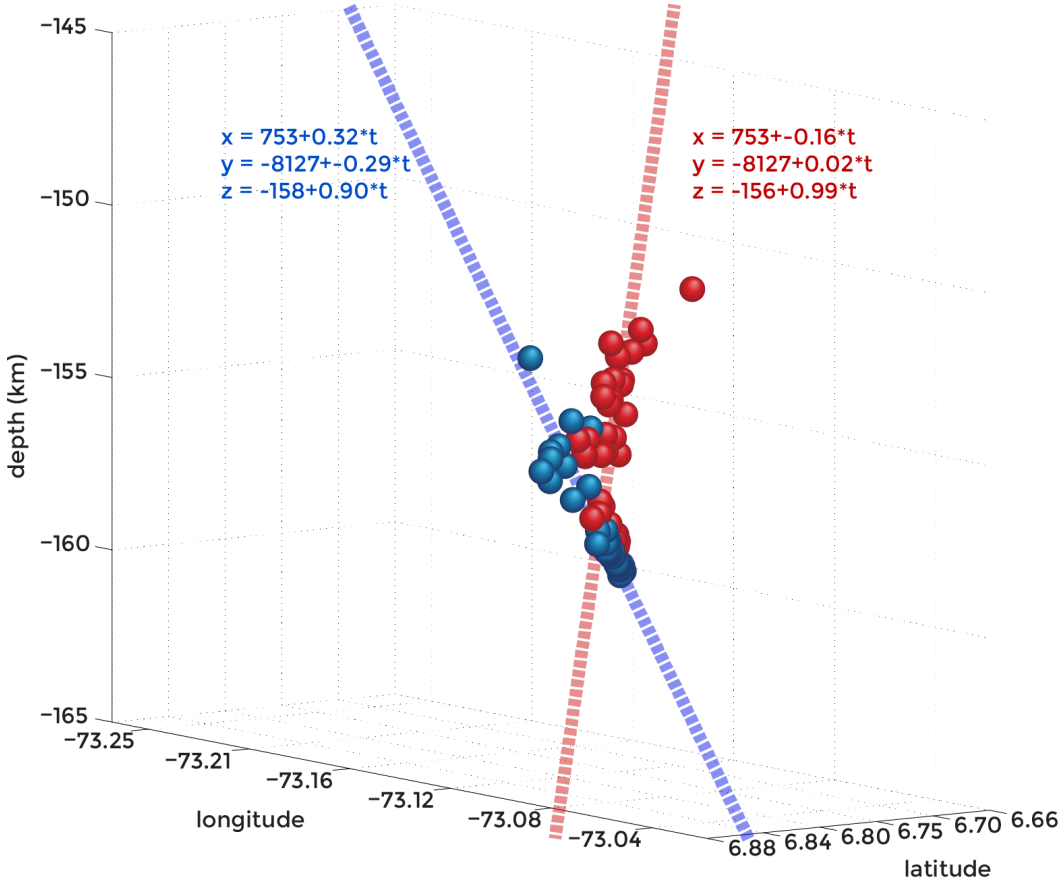

Figure 3-16. Lines of best fit to each of the relocated populations following the feature extraction process. Both occurring on steeply dipping features at high angles to one another.

The repeating and reverse polarity groups are in close proximity, yet their waveform polarity differences suggest opposite directions of motions. Boudin formation (boudinage) has been associated with large-scale nest formation as in the case of the Hindu-Kush Nest (Lister et al., 2008). Boudins form as elongated, rigid bodies surrounded by less competent (ductile) material in shear zones. The boudins stretch in response to the ambient stress conditions and can break apart in a process call "necking." In the process of boudin formation, a predominant shear direction is evident, often with an antithetic direction of shear also supporting slip. Field observations of boudins range in size from several centimeters, to tens of meters. When this explanation is used in the Hindu-Kush Nest to describe contrasting focal mechanism data, the authors suggest boudin formation on a large scale (~100km). In

the Bucaramanga Nest, each of the groups observed is associated with a shear zone in a boudin-like zone within the nest (Figure 3-17). If field observations and the Hindu-Kush Nest are used as boundaries for the scale of this process, it seems reasonable to suggest such a process might occur on a ~5-10 km scale.

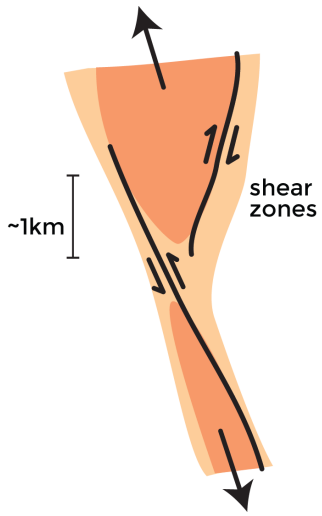

Figure 3-17. Schematic of Bucaramanga Nest boudinage. Each shear zone supports one of the above groups of seismicity. The opposite sense of shear is observed in the waveforms of A groups (upward first arrival) and B groups (downward first arrival).

This interpretation is consistent with prior observations of Bucaramanga Nest seismicity by Prieto et al., (2013). They compare stress drops of shallow earthquakes with those of the Bucaramanga Nest and find higher stress drops in the nest earthquakes. A study of the energy budget that incorporates the high stress drop observes low radiation efficiency (about an order of magnitude smaller than in the case of shallow events) and suggest a dissipative mechanism of failure. The authors model a lower-bound temperature rise of more than 600°C for shear zones of thickness 1-3 cm and corresponding fracture energies sufficient for frictional melting of peridotite (10-30 MJ/m^2). These ambient conditions, coupled with observations of distinctions of fundamental parameters between shallow and intermediate-depth earthquakes supports the idea of a separate failure mechanism from shallow earthquakes. Boudinage is a process that is known to occur in regions with high shear under ductile conditions. The case for boudin formation is further supported by suggestions by John et al., 2009. The authors in this case suggest thermal shear instability might be initiated by a grain-size reduction in material. While they suggest this might be an outcome of hydration reactions, this might also be stated as a

mechanism for a contrast between mechanically strong and mechanically weak layers commonly associated with boudin formation.

There is some evidence for shear localization along boundaries in boudin formation; however, in peridotite materials the observation is relatively rare. There are field observations of pseudotachylytes in Italy (e.g., Piccardo et al., 2010; Ueda et al., 2008) that suggest frictional melting produced by seismic slip (in a process such as thermal shear instability). It is possible that dehydration reactions still may play a role in facilitating the failure of thermal shear instabilities in boudin formation.

The September 2011 Sequence: Evidence for Cascading Failure

A subsequence of seven events occurred in the Bucaramanga Nest on 6 September 2011. These events are all members of Group B and occur in a rapid succession of cascading failure (Table 3-1). We relocate only this subset of events, again using hypoDD to examine their relationship with one another and feature extraction relocation to find a simple structure. One event, 21 (italics in Table 3-1), is not as well connect with the rest of the group based on correlation coefficients and is not relocated in the double-difference relocations. The other six events and their final locations are shown in Figure 3-18.

Table 3-2 Events in September 2011 Sequence

Year	Month	Day	Time	Latitude	Longitude	Depth	EventID
2011	9	6	19:59:03	6.788	-73.109	143.7	17870
2011	9	6	19:59:16	6.788	-73.109	143.7	20
2011	9	6	20:01:35	6.745	-73.088	137.5	17871
2011	9	6	20:02:29	6.804	-73.133	147.2	17873
2011	*9*	*6*	*20:04:44*	*6.788*	*-73.109*	*143.7*	*21*
2011	9	6	21:08:20	6.759	-73.052	132.4	17876
2011	9	6	21:34:10	6.785	-73.118	146.7	17877

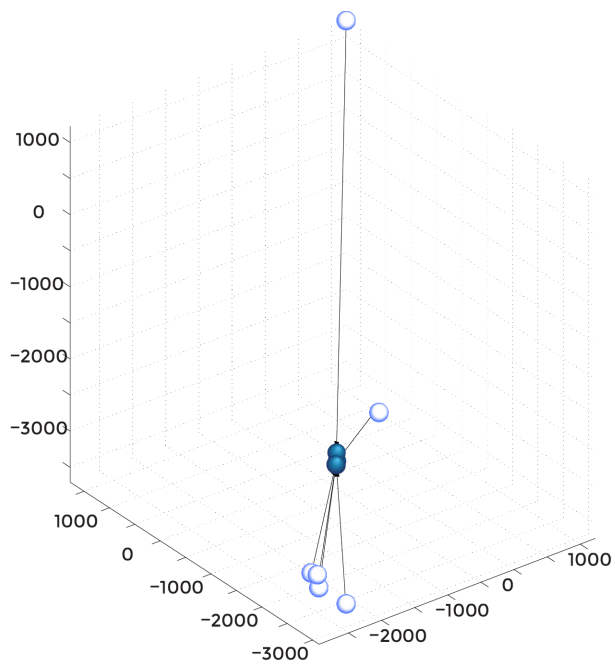

Figure 3-18. Relocation of the September 2011 subset of Bucaramanga Nest earthquakes from their double-difference relocation positions (open circles) to feature extraction locations (solid circle).

These events are closely located to one another. Their relative distances, following feature extraction relocations, are less than 200 m at most (Table 3-2).

Table 3-3 Distance between Relocated Events (in meters)

	17870	**20**	**17871**	**17873**	**17876**	**17877**
17870	-	45	13	2	155	17
20	45	-	52	46	113	51
17871	13	52	-	13	163	27
17873	2	46	13	-	155	18
17876	155	113	163	155	-	157
17877	17	51	27	18	154	-

The size of the rupture can be estimated using equation 3-2 using magnitude and reasonable stress drops. For an event of M_w ~2 and a stress drop of 10 MPa, we can expect a circular rupture patch with radius ~54m (Figure 3-19a). It has been suggested

that for thermal shear failure, very high stress drops might be necessary; we also test the case of a 100 MPa stress drop (Figure 3-19b).

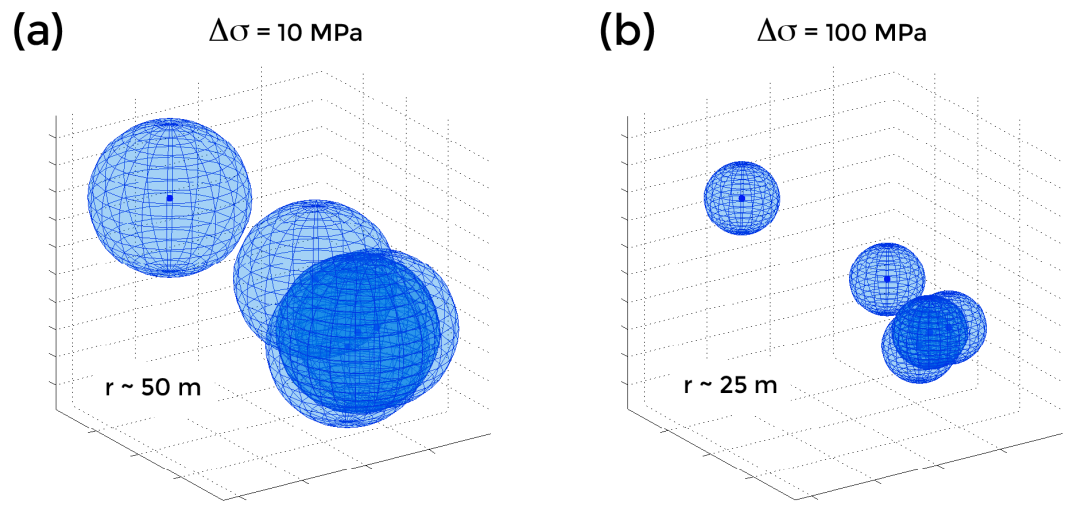

Figure 3-19. Estimated rupture areas for circular asperity failure (radius estimated here in all dimensions as a sphere) in the case of 10 MPa stress drop (a) and 100 MPa stress drop (b).

Even considering more conservative rupture areas, the sequence of events are largely overlapping, nearly perfect repeating events. The inter-event time increases during the sequence from ~13 seconds between events 17870 and 20 to ~1600s for events 17876 and 17877. There does not appear to be a connection battening timing of the events and a rupture direction.

As mentioned in Chapter 1, the 1977 Vrancea earthquake shows a pattern of down-dip cascading failure (Müller et al., 1978), the earthquake was likely four composite events. Investigating the waveforms of these composite events strengthens the analog; Müller et al. (1978) show one event with a reversed polarity to the other three events. The waveforms for this event were not readily available so no further quantification of their similarity is possible beyond visual inspection.

The cascading failure process in the Vrancea earthquake is similar to the 2011 September sequence in the Bucaramanga Nest. Although the Bucaramanga Nest sequence are all of the same polarity and rupture direction is not resolvable, the

repeating failure in quick succession in both space and time provides evidence towards a positive feedback process, such as thermal shear failure.

Conclusions

In this chapter, a new type of repeating earthquake is introduced, the reverse polarity repeat. A revision of Figure 3-2 to include this new variety is necessary (Figure 3-20). These polarity reversals continue for long periods of time and occur in quick cascading type failures in both space and time. It should become a standard practice for seismologists investigating repeating earthquakes to also record the minimum of the cross correlation function to identify these reverse-polarity repeating earthquakes.

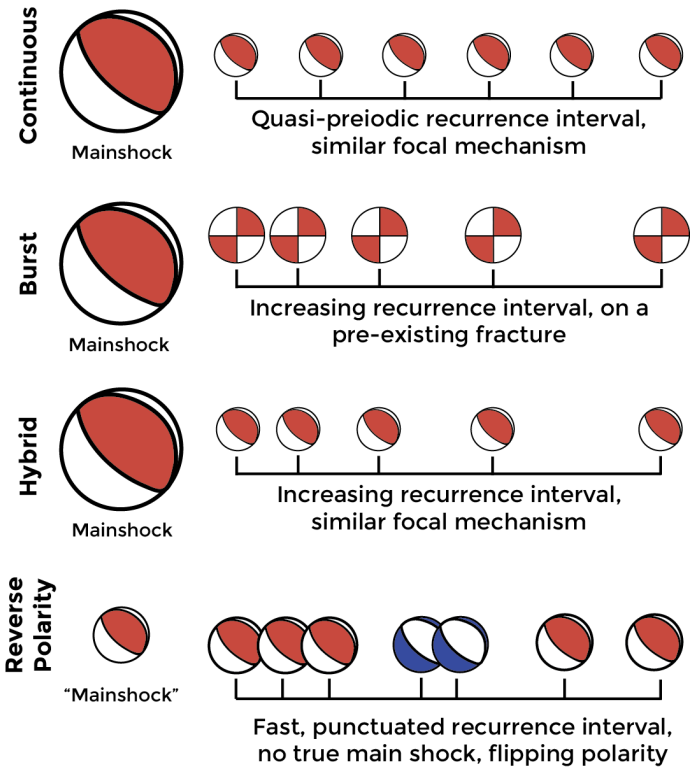

Figure 3-20. Revised figure showing new reverse polarity type repeating earthquakes as observed in the Bucaramanga Nest.

Double different relocations and subsequent feature extraction shows each family of reverse polarity events corresponds to slip on a close, but separate structure. We

invoke and interpretation of boudinage within the subducting slab to explain these roughly linear features. Field geology observations support the idea of opposite senses of motion in boudinage under ductile shear regimes. We interpret these two structures with opposite sense of slip to be associated with an independent shear zone along the edges of a rigid boudin and a material undergoing ductile deformation. Thermal shear instability failure could occur along these shear zones

We investigate a small sub-sequence of earthquakes in a repeating family. They are located very closely in both space and time. We are unable to differentiate differences in their locations from one another based on an estimated rupture area and are unable to verify if there is a dominant direction of rupture propagation in this sequence. However; their rapid failure in a such a concentrated region indicates a swift failure process, as would be expected for rapid acceleration in thermal shear instability failure.

References

Barrett, S. A. (2010), Observation and analysis of repeating earthquakes beneath the Aceh Basin, Northern Sumatra. Thesis. The Pennsylvania State University. State College, PA.

Blashfield, R. K. (1976). Mixture model tests of cluster analysis: accuracy of four agglomerative hierarchical methods, Psychological Bulletin, v. 83, (3), 377-388.

Brune, J. N. (1970). Tectonic stress and the spectra of seismic shear waves from earthquakes, *J. Geophys. Res.*, **75**, 26, 4997-5008, doi: 1029/JB075i026p04997.

Cortés, M. and J. Angeleir, (2005). Current States of Stress in the Northern Andes as Indicated by Focal Mechanisms of Earthquakes, *Tectonophysics*, 403, 29-58.

Dieterich, J. H. and B. D. Kilgore (1994), Direct observation of frictional contacts: new insights for state-dependent properties, Pure and Applied Geophysics, 143, 283-302.

Faller, A. J. (1981), An average correlation coefficient, *J. appl. Meteor.*, **20**, 203-205, doi: 10.1175/1520-0450(1981)020<0203:AACC>2.0.CO;2.

Igarashi, T., T. Matsuzawa and A. Hasegawa (2003). Repeating earthquakes and interplate aseismic slip in the northeastern Japan subduction zone, Journal of Geophysical Research, 108, (B5) 2249-2258, doi: 10.1029/2002JB001920.

John, T., S. Medvedev, L. H. Rüpke, T. B. Andersen, Y. Y. Podladchikov, and H. Austrheim, (2009). Generation of intermediate-depth earthquakes by self-localizing thermal runaway, *Nat. Geo.*, **2**, 137-140, doi: 10.1038/NGEO419.

Jones, R. H. and R. C. Stewart (1997). A method for determining significant structures in a cloud of earthquakes, *J. of Gephys. Res.*, **102**, doi: 10.1029/96JB03739.

Kaufman, L. and P. J. Rousseeuw (1990), Finding groups in data: an introduction to cluster analysis, John Wiley & Sons, Inc. New York, New York, pp. 1-63, 199-279.

Kimura, H., K. Kasahara, T. Igarashi, and N. Hirata. (2006). Repeating earthquake activities associated with the Philippine Sea plate subduction in the Kanto district, central Japan: A new plate configuration revealed by interplate aseismic slips, Tectonophysics 417, 101-118, doi:10.1016/j.tecto.2005.06.013.

Lister, G., B. Kennett, S. Richards, and M. Forster, (2008). Boudinage of a stretching slablet implicated in earthquakes beneath the Hindu Kush, *Nat. Geosc.*, **1**, 196-201, doi: 10.1038/ngeo132.

Müller, G., Bonjer, K. P., Stockl, H., & Enescu, D. (1978). Romanian earthquake of March 4, 1977 i. Rupture process inferred from fault-plane solution and multiple-event analysis, *J. of Geophys.-Zeitschrift fur Geophysik*, 44 (3), 203-218.

Nadeau, R.M. and L.R. Johnson (1998). Seismological studies at Parkfield VI: Moment release rates and estimates of source parameters for small repeating earthquakes, Bulletin of the Seismological Society of America, **88,** (3) 790-814.

Peng Z., J. E. Vidale, C. Marone and A. Rubin (2005), Systematic variations in recurrence interval and moment of repeating aftershocks, Geophysical Research Letters, 32, (15), L15301, doi: 10.1029/2005GL022626.

Piccardo, G. B., G. Ranalli, and L. Guarnieri (2010), Seismogenic shear zones in the lithospheric mantle: ultramafic pseudotachylytes in the Lanzo Peridotite (Western Alps, NW Italy), *J. of Petrology*, **51**, 1, 81-100, doi: 10.1093/petrology/egp067.

Schaff, D. P., G. C. Beroza, and B. E. Shaw (1998), Post seismic response of repeating aftershocks, *Geophys. Res. Letts.*, **25**, 24, 4549-4552.

Schneider, J. F., Pennington, W. D., & Meyer, R. P. (1987). Microseismicity and focal mechanisms of the intermediate-depth Bucaramanga nest, Colombia, *J. of Geophys. Res.* **92**, (B13), 13913-13926, doi: 10.1029/JB092iB13p13913.

Shelly, D. R., G. C. Beroza, and S. Ide (2007). Non-volcanic tremor and low-frequency earthquake swarms, Nature 446, 305–307.

Ueda, T., M. Obata, G. Di Toro, K. Kanagawa, and K. Ozawa (2008). Mantle earthquakes frozen in mylonitized ultramafic pseudotachylytes of spinel-lherzolite facies, *Geology.*, v. 36, no. 8, 607-610, doi: 10.1130/G24739A.1.

Waldhauser, F. (2001), HypoDD: A computer program to compute double difference hypocenter locations, U.S. Geol. Surv. Open File Rep., 01-113, 25 pp.

Waldhauser, F., and W. L. Ellsworth (2000), A double-difference earthquake location algorithm: Method and application to the northern Hayward fault, California, Bull. Seismol. Soc. Am., 90, 1353 – 1368.

CHAPTER FOUR:

A Deficiency of Small Magnitude Earthquakes at Intermediate-Depths

Earthquake Catalogs and Detectability

The probability of detecting an earthquake depends on many factors, chiefly the magnitude of the earthquake, the network geometry, and the distance between source and receiver. A strong knowledge of the level to which a catalog is complete is useful in studies of seismicity to understand a region's hazard and risk as well as for monitoring the state of operation of a seismic network. The level and distribution of completeness can be measured in different ways: magnitude of completeness (Woessner and Wiemer, 2005), b-value / Gutenberg-Richter distribution (Gutenberg and Richter, 1944), or probability of detection (Schorlemmer and Woessner 2008; Bachmann, 2011). Woessner and Wiemer (2005) use the entire range of magnitudes to determine the magnitude of completeness (and its associated uncertainty) from a distribution of cumulative and non-cumulative magnitude frequency distribution. The approach in Gutenberg and Richter (1944) studies the relative frequency of small to large magnitude earthquakes. The method of determining the probability of detecting an earthquake of a given size, at a given distance from source to receiver is outlined in Schorlemmer and Woessner (2008) on a catalog of earthquakes in northern California.

Earthquakes are generally thought to follow a power law relationship with the base-10 logarithm of event frequency proportional to the magnitude, which is a logarithmic measure of seismic wave amplitude, (eqn 4-1, Gutenberg and Richter, 1944), i.e.:

$$log_{10}(N) = a - bM \qquad \textit{equation 4-1}$$

Where N is the frequency of earthquakes with magnitude greater than or equal to a given magnitude (M). The parameters a and b are largely empirical and represent the intercept, a, which represents the number of M > 0 earthquakes in the population and the negative of the slope, b, which describes the relative number of large vs. small earthquakes, and is in most cases nearly equal to 1. In practice, distributions of seismicity diverge from this relationship at both limits of recorded magnitudes. Missing large magnitude events are thought to be a result of insufficient monitoring time or limited fault system size, while missing small events are usually thought to be the result of limitations in detection capability of a seismic network. Often it is at the point where the linear relationship deviates from the number of observed small magnitude earthquakes that seismologists question the completeness of a catalog (M_c); however, it can be difficult to identify this magnitude accurately. A detection threshold based on a break in b-value has other important disadvantages. First, it's difficult to determine spatial variations in the detection threshold because that requires dividing the data into subsets. Second, it's difficult to document time-dependent changes, which are important as stations drop out/are added, for the same reason. Third, it's silent about the detection threshold where no earthquakes are detected. An alternative approach (Schorlemmer and Woesner, 2008) takes known earthquakes and determines the detection probability as a function of magnitude and distance. It uses that to map the probability that an earthquake is detected as a function of assumed magnitude and location. This is what we really want to know, and it has the further advantage of making no assumption about the magnitude-frequency relation.

Schorlemmer and Woessner (2008) propose a new framework that is empirically based probability of detection, $P_D(M, L)$ for an event of any given magnitude (M) at any given distance (L) from a station (Probabilistic Magnitude of Completeness, PMC). This yields a series of maps for all stations in the network showing the probability-based completeness. The initial work provides an example in a well-maintained network in Southern California over a broad region, but has been utilized in many settings including the Northern California Seismic Network (Bachmann, 2011), and the Swiss Seismic Network (Nanjo et al., 2010). In this chapter, we will adapt the probability of detection metric for earthquakes, but largely neglect the distance parameter due to the small dimension (~10 km) of the Bucaramanga Nest relative to the propagation distance (~160 km at the epicenter).

The performance of a catalog can be improved by using more sensitive earthquake detection techniques that can identify earthquakes of small magnitude that would otherwise go unreported – either because their signal strength is too small, or because the are recorded by fewer than the minimum of four stations required to locate an earthquakes. While in shallow earthquakes the smallest observable magnitude is pushed smaller and smaller, there is some evidence for a critical nucleation size for earthquakes that might failure under a mechanism other than brittle-shear. As discussed in Chapter 1, in thermal-shear runaway failure there is thought to be a critical shear zone thickness.

$$Z > \frac{\rho C_p \Delta T \, \kappa}{\upsilon \tau} \qquad \textit{equation 4-2}$$

ρ – density
C_p – specific heat
ΔT – change in temperature needed to achieve melting
κ – thermal diffusivity
υ – velocity of plastic deformation
τ – shear stress

The critical thickness is the limit at which energy within the layer is unable to conduct away from the layer quickly enough to avoid melting. Melting can lead to the temperature instability that allows for a runaway process.

In this chapter, we seek to understand the smallest detectable earthquake originating in the Bucaramanga Nest. Verifying the true absence of such events in the catalog might provide a line of evidence towards a process of thermal shear instability as the underlying mechanism for failure in intermediate-depth earthquakes.

A Minimum Earthquake Size

Thermal shear instability failure suggests there is a minimum amount of slip necessary in order for the process to "runaway". To start this failure process of positive feedback for a given earthquake size, the rupture patch must undergo sufficient slip. If the earthquake is too small, it will not produce the slip and associated frictional heating necessary for a seismic failure. This would produce a deficiency of small magnitude earthquakes in the Bucaramanga Nest catalog and a deviation from typical GR distributions. If intermediate-depth earthquakes undergo a failure process similar to brittle failure (as in the case of dehydration embrittlement), there would be no deficiency in small magnitude earthquake beyond the limits of the detection method. We seek to quantify the distribution of the small magnitude earthquakes in the Bucaramanga Nest as well as the limitations of our detection methods.

The Initial Distribution of Earthquake Magnitudes

The National Colombian Seismic Network Catalog (RSNC) contains thousands of events each year originating in the Bucaramanga Nest. Their network of instruments record most of these earthquakes, especially on two broadband instruments closest to the nest: BRR and RUS. While these stations are still ~170 km from the center of nest, they represent the closest arrangement available on well-maintained stations. For the period of interest in the first six months of 2013, the RSNC catalog contains 7282 events, 3851 of which are earthquakes in the Bucaramanga Nest. Dropouts on these two stations are common; however, they still operate with a higher performance than most stations in the network. We use a modified Gutenberg Richter (G-R) diagram (Figure 4-1), which shows binned magnitudes (rather than ≥M) to highlight the drop

off in detection of small magnitude earthquakes. The RSNC catalog shows a deviation from the expected linear relationship around M_L ~2. A best-fit line with a slope of 1 is generally expected for G-R distributions, although this value varies depending on setting. The RSNC catalog magnitudes for Bucaramanga Nest earthquakes have a b-value of 0.82. This value differs from the b-value reported by Frohlich (2006) who obtains a *b*-value of 1.59, by combining a temporary local network, the ISC and CMT catalogs. Frolich's results would indicate far more energy is released in the nest in the form of small earthquakes than in the more general case; however it is inconsistent with our findings during the time period in question.

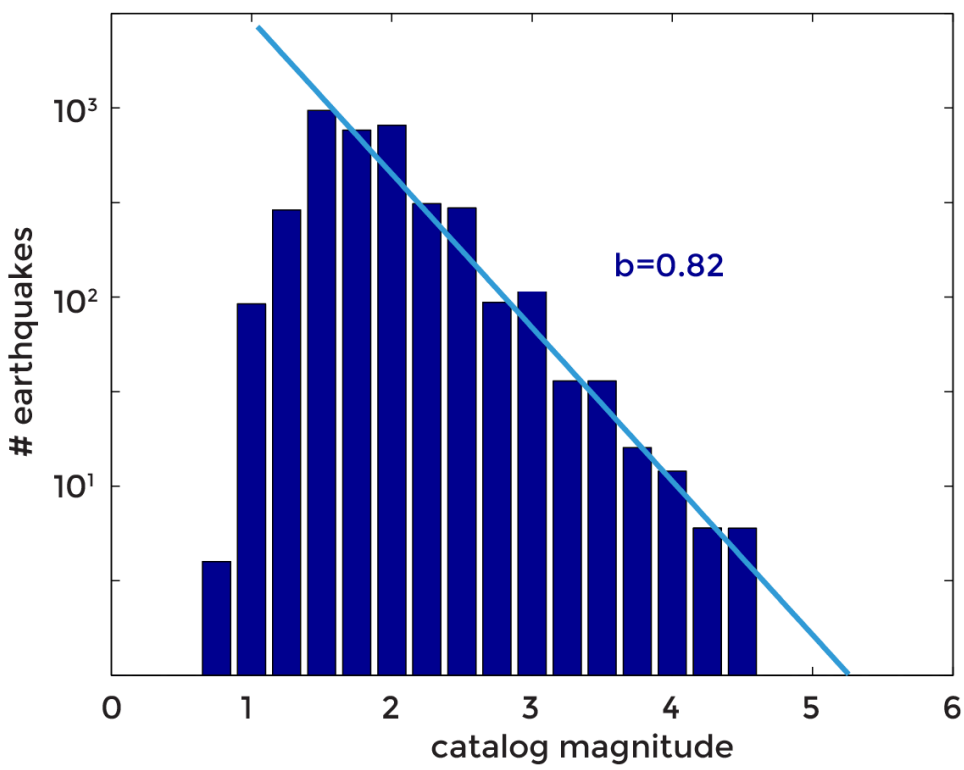

Figure 4-1. Modified Gutenberg-Richter distribution for earthquakes in the RSNC catalog during the first six months of 2013.

In order to include the magnitudes of newly detected earthquakes into this distribution in a consistent way, we recalculate the RSNC magnitudes based on the maximum amplitude of the *S*-wave arrival of the earthquakes. As the relationship between the $\log_{10}$(maximum *S* amplitude) and the magnitude should be approximately linear, we

investigate the use of several magnitude ranges to achieve a best-fit line with a slope ~1 (Figure 4-2)

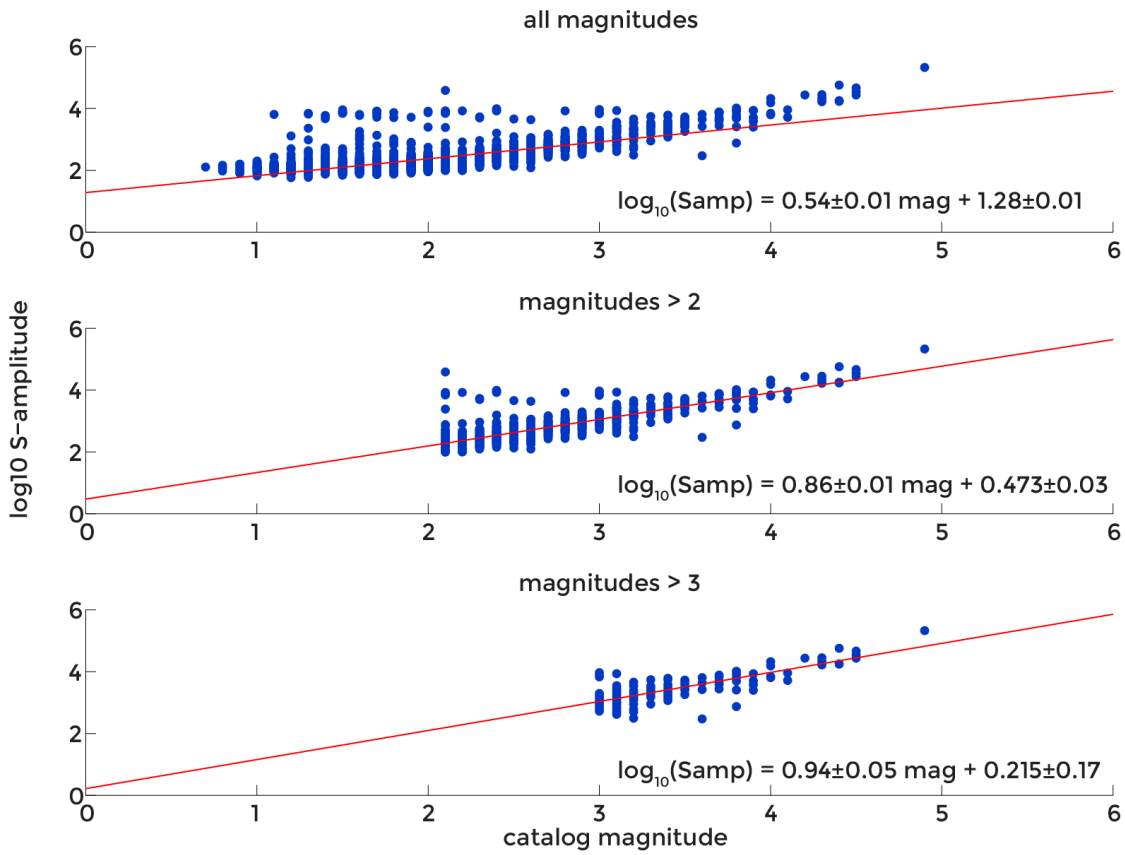

Figure 4-2. Relationship between catalog magnitude and $\log_{10}$ of the maximum S-wave amplitude using various magnitude ranges. A least squares method is used for the linear fit; standard errors for the 95% confidence intervals are shown. The relationship should be roughly linear with a slope approximately equal to 1.

We only obtain a *b*-value that approaches 1 when we use RSNC events of magnitude 3 and larger. These are also likely to be the most reliable magnitudes, and we use this relationship between these amplitudes and magnitude and extrapolate it to smaller magnitudes in order to develop more reliable magnitudes for small earthquakes that are based on the maximum *S*-wave amplitude (Figure 4-3). Our adjustment tends to increase the magnitude of relative to the magnitudes in the catalog. It is common practice for local earthquake monitoring agencies to use proxies for the preferred maximum wave amplitude, and these proxies can be subject to biases at small

magnitude levels. We refer to our recalculated magnitudes as the local magnitude (Figure 4-4).

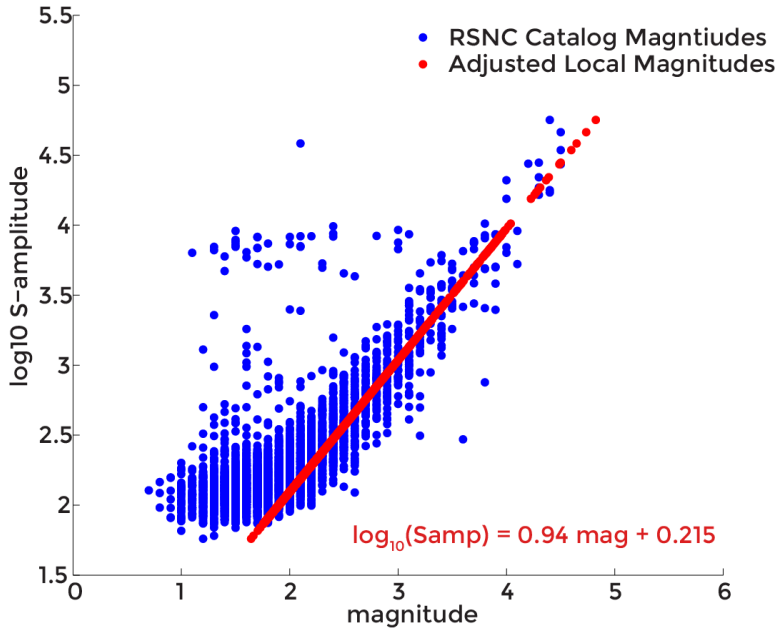

Figure 4-3. Relationship between S-wave amplitudes, catalog magnitude and our revised shifted local magnitude, following the equation obtained in Figure 4-2.

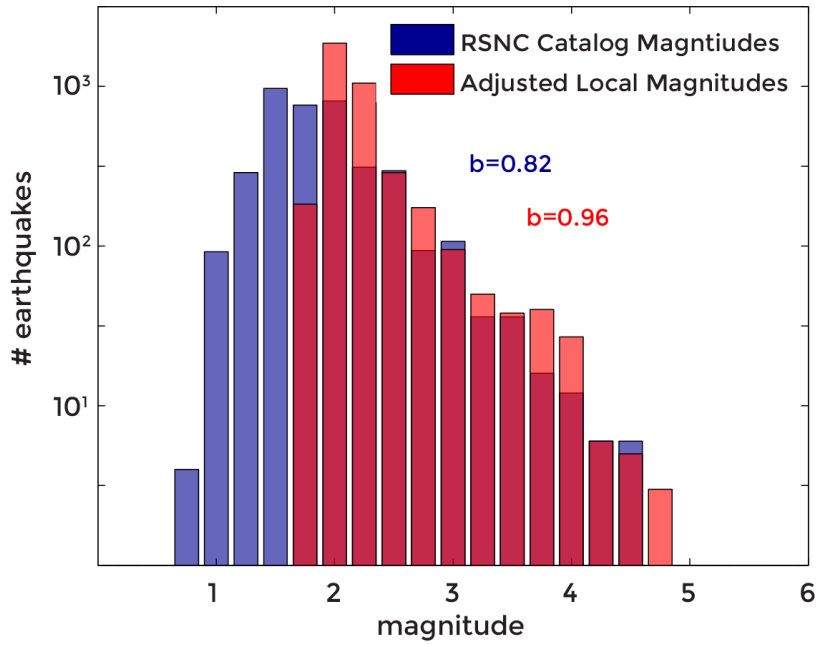

Figure 4-4. Modified GR diagram with RSNC data (blue) and calculated local magnitudes following obtained using the event S-amplitude arrival.

Empirical Subspace Detection

To maximize the number of earthquakes in this catalog, we employ an empirical subspace detector (Barrett and Beroza, 2014; see also: Chapter 2). We use 175 empirical subspace detectors on six months of continuous data in 2013 at our two best broadband stations RUS and BRR. Examples are shown in this work for RUS. These 175 templates are shown to sufficiently span the variation of nest events. We are able to successfully detect more than 95% of earthquakes in the RSNC catalog only using this subset of templates. We find an additional 35,855 Bucaramanga Nest events not previously included in the RSNC catalog, nearly ten times the cataloged amount. New earthquakes are incorporated into the catalog with assigned magnitudes based on their maximum *S*-wave amplitude as described above. Most earthquakes missing from the catalog are smaller in magnitude, thus the empirical subspace detection method adds a disproportionate number of smaller events, as expected (Figure 4-5).

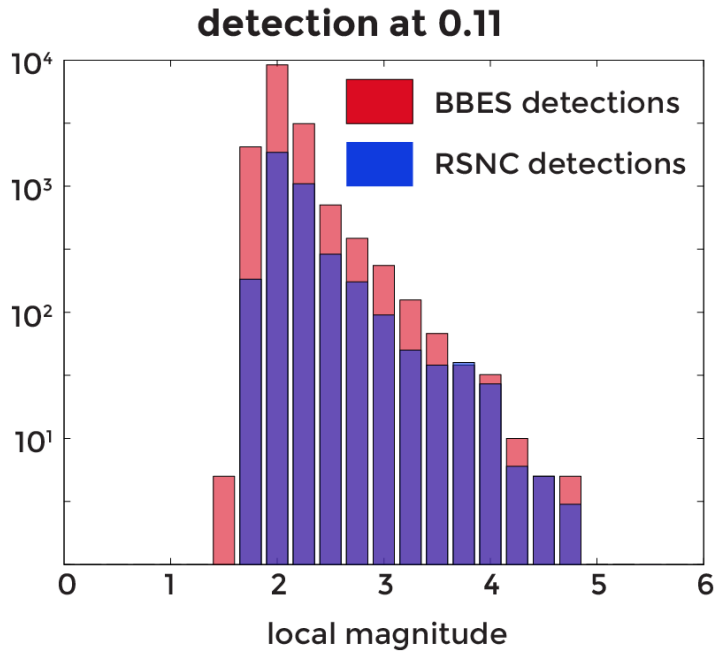

Figure 4-5. Modified GR diagram of new detections compared to RSNC catalog with adjusted local magnitudes. Note that the vertical axis is logarithmic such that the great majority of new detections are small magnitude earthquakes.

In the empirical subspace detection method there are several parameters that can be empirically tuned. The search window length limits the number of detections within a certain time period. This limit is necessary as template *P*-wave arrivals often produce

high correlations with *S*-wave arrivals at a substantial detection threshold, yet this correlation is always smaller than the correct alignment of the template and the event within the continuous signal. These false positives can be quickly removed by stipulating that a detection must be the largest correlation within a window length comparable to the *S-P* time for an event originating in the Bucaramanga Nest. In this setting we selected a time window of 22.5 seconds. Using a shorter time window adds more "detections"; however, many of these would be false positives due to the described misalignment (Figure 4-6). Using a slightly longer window, we find only slightly fewer earthquakes (~2%) than in our 22.5 s window condition; however, because we are attempting to maximize detections of small earthquakes, we chose the more liberal detection criterion..

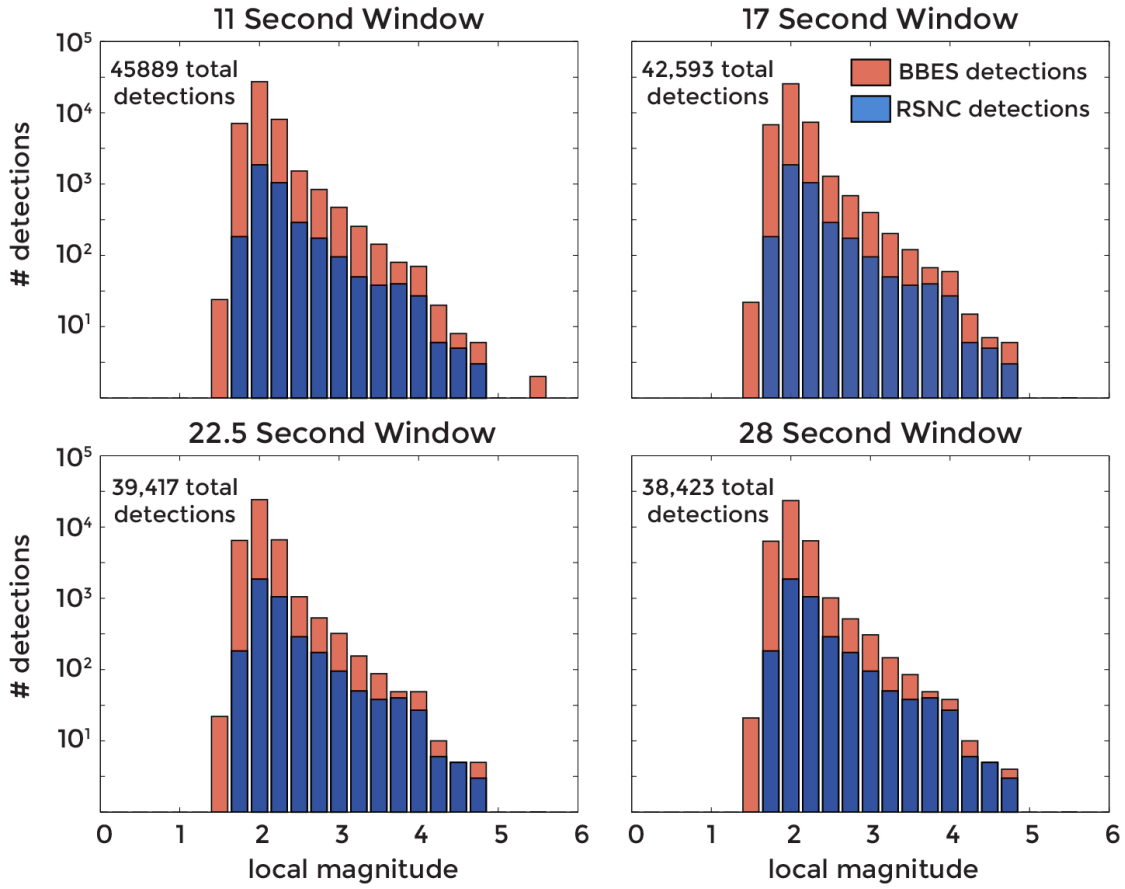

Figure 4-6. Modified GR distributions for various detection windows. The 22.5s window length corresponds to the *S-P* time for an event originating in the Bucaramanga Nest and is used in the final analysis.

The other primary free parameter in the empirical subspace method is the detection threshold. The detection threshold is defined as the normalized projection of section of continuous seismic signal onto the detection subspace. For simplicity, only the value corresponding with the template with the highest correlation is considered. This detection threshold should be set low so as to identify as many small earthquakes as possible (Figure 4-7). There is a trade off to small thresholds, if it is set too small, events outside the nest will be detected (false positives). These are especially evident in the case of large earthquakes from other regions in the subduction zone (detection thresholds 0.07 and 0.05). The selected value of 0.09 is further supported by a series of synthetic tests used to quantify detection performance metrics.

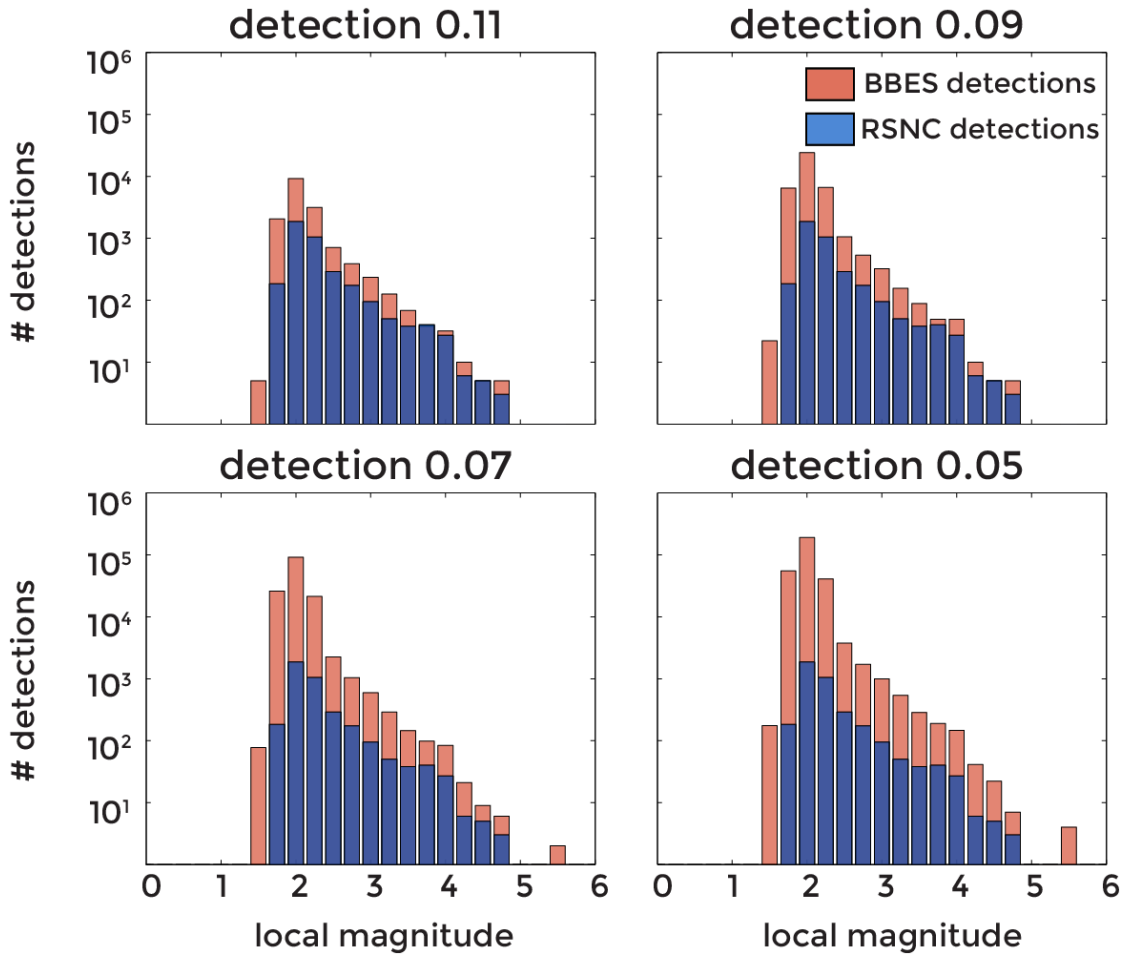

Figure 4-7. GR distributions for various detection levels. When the detection threshold is low enough, false detections will overwhelm the true detections.

The ability to detect an earthquake can be hindered by the background noise level in a continuous section. For a set of newly detected small magnitude earthquakes ($M_L < 2$) we can barely observe these signals in the continuous section (Figure 4-8). With a bandpass filter applied, the seismic characteristics of most the waveforms are clear. We check the ability to detect these small magnitude earthquakes, if they exist, by adding known earthquakes to the continuous signal in a synthetic test.

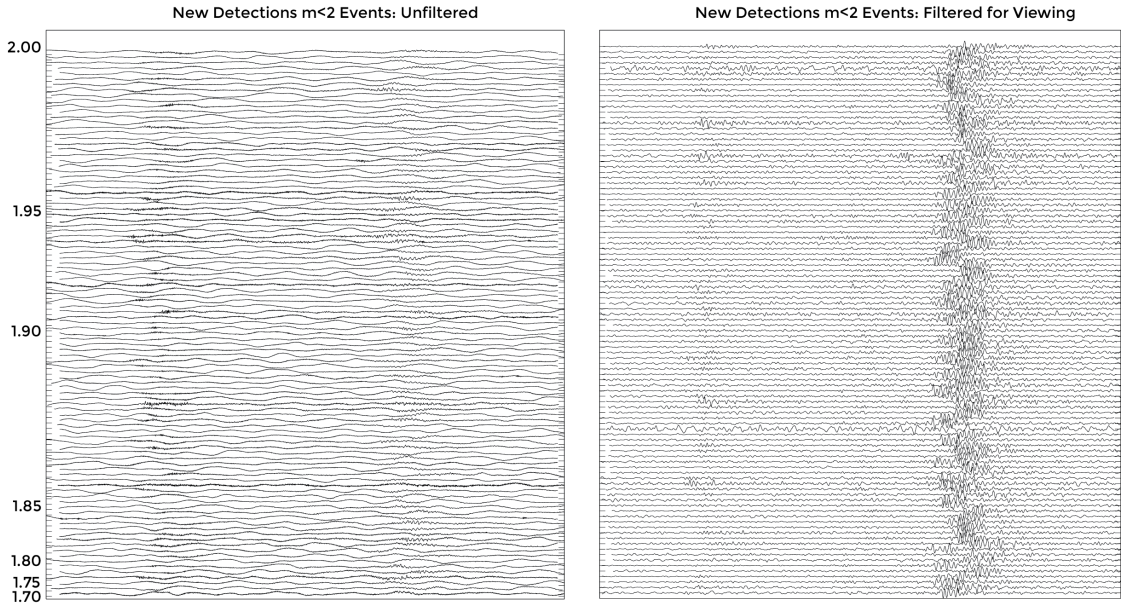

Figure 4-8. Waveforms of small magnitude earthquakes detected only in the subspace detection case. Unfiltered as detected (left) and filtered 1-10 Hz (right).

Synthetic Tests

To verify the ability of the empirical subspace detectors to find small magnitude events, we artificially and systematically plant small magnitude events from m_L=-1 to 3 at intervals of 0.1 magnitude units, by scaling their relative amplitudes into a continuous record from the station of interest. A randomly selected, scaled event is added to the continuous section at each minute during day 25 of 2013. These synthetically added earthquakes are drawn from a RSNC catalog population of nearly four thousand earthquakes during the first six months of 2013. Additionally, there were 24 naturally occurring earthquakes on day 025. A total of 1464 earthquakes of each 0.1 local magnitude unit are tested using the same 175 templates as used above. The performance of this set of detectors at various detection thresholds and search windows is shown in Figure 4-9. We find that using alternative time periods does not significantly affect the recall performance. The most noticeable change in the synthetic test recall when varying the time period used is at the very small magnitudes (less than $m_L \sim 0$) where the analysis is dominated by type I errors (Figure 4-10). The slight variation in the time used for the synthetic test is not enough to account for the lack of small magnitude events in the final magnitude-frequency distribution. We can

use the recall (true positives / relative events) of each of these detection thresholds at various magnitudes to project the portion of earthquakes missing due to limits of the detection method into our modified G-R distributions.

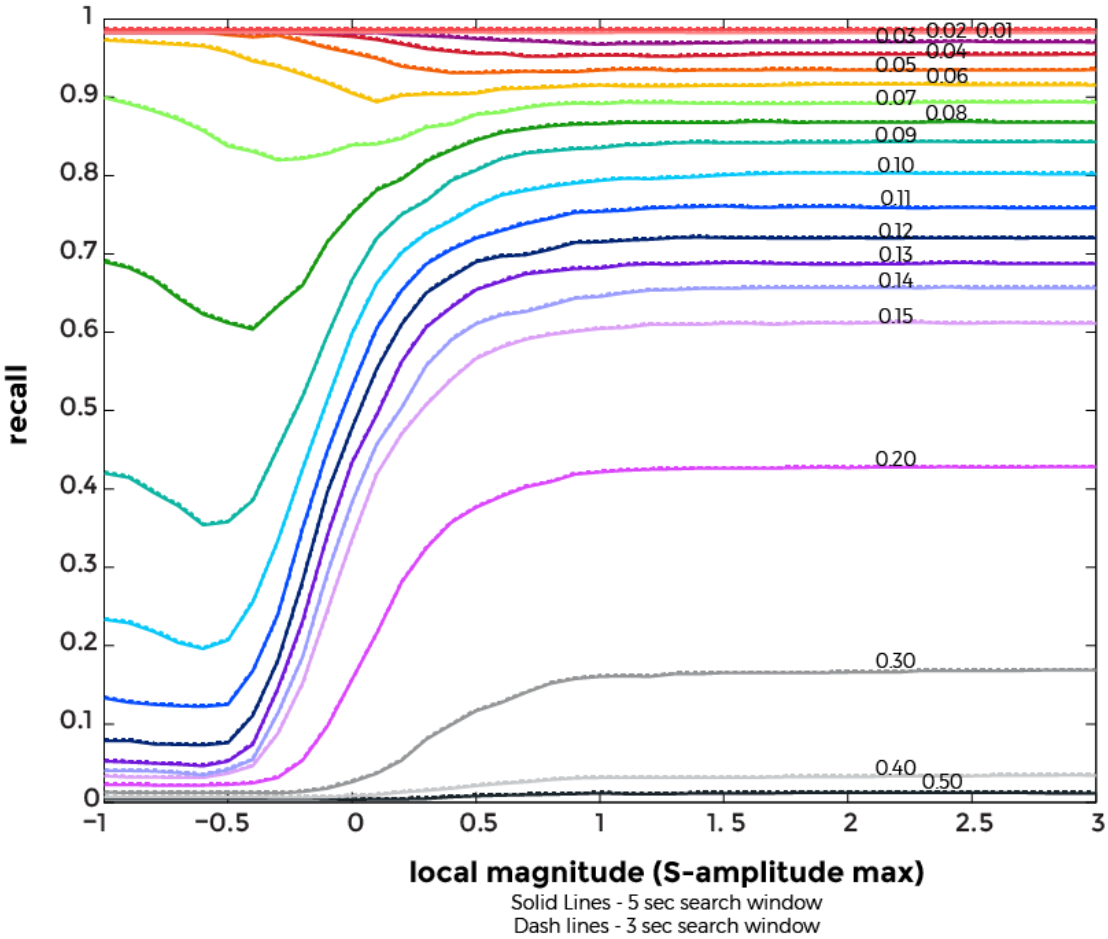

Figure 4-9. Recall performance of detectors using various thresholds across a range of small magnitudes. Each line represents a different threshold of detection. Successful detects are within 3 seconds of a known event (dashed) or 5 seconds (solid). The point which recall begins to increase again is when type I errors or false detections begin to dominate the method.

Accounting for Missing Events through Error Sources

It is helpful to address sources of error in terms of Type I (false positive) and Type II errors (missed detections). Typically, Type-I errors are considered the more serious because they represent the incorrect rejection of the null hypothesis. In our analysis, however, we are not so concerned with Type I errors since our goal is to detect as many earthquakes as possible. The null hypothesis that we seek to test, is that the

number of small earthquakes follows power-law behavior down to the detection threshold. Committing Type-I errors in the detection phase, would boost the number of small earthquakes, and hence would tend to diminish the possibility of incorrectly rejecting the null (Gutenberg-Richter distribution) hypothesis. Type-II detection errors, on the other hand, would be more serious than they are usually considered to be. They could lead to the incorrect rejection of the null hypothesis by concluding that small earthquakes do not follow a Gutenberg-Richter distribution. We quantify missed detections (Type II errors) in an early section, showing ~95% of earthquakes in the RSNC catalog are detected using our method. Additionally, we check these missed detections against the operation of the station. RUS occasionally has station daily station dropouts lasting ~10-20 seconds; however, it is operational 99% of the time during the period of interest. Due to its proximity to the Bucaramanga Nest, it is still the ideal station to use to identify the maximum number of small earthquakes. We also verify new detections are not in periods of outages.

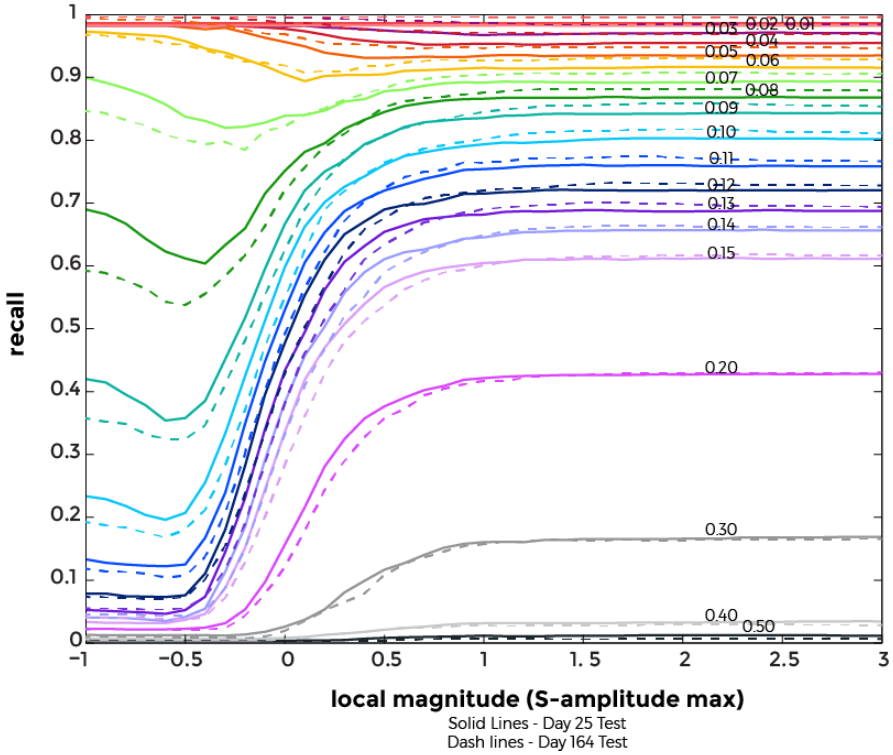

Figure 4-10. Recall performance tested on different time periods. The results of the two days shown in this plot (day 025 and 164) are largely similar except at very small magnitudes where type I errors dominate the results.

Another performance metric to consider is the false omission rate. This value is the ratio of false negatives (missed detections, type II errors) to the sum of the false and true negatives. In this study, the amount of detections (and true negatives) is limited by the window length of search (Figure 4-6). In 180 days, using a window length equal to the S-P time, there are 691,200 possible outcomes of the detection test. Less the number of positive detections there are 655,345 negative detections. We can estimate the false negative rate by using the number of RSNC catalog events that are detected using this method. For the final values (detection threshold 0.09, window length 22.5 seconds) we find that 92% of cataloged events are detected, yielding a false negative rate of 0.08 (or 290 events). If we apply this same rate of false negative to our 35,855 new detections, we expect an additional 2868 events are missed. The false omission rate for this distribution is then the missed detections / all negative outcomes or 0.0044.

Small Magnitude Earthquake Waveforms

The smallest local magnitude earthquakes as detected by the subspace method are m_L ~1.5. At these small magnitudes, it is difficult to distinguish seismic signal from the background noise level on unfiltered records (Figure 4-11). We can verify these events more clearly by imposing a bandpass filter of 1-5 Hz (Figure 4-12). When compared to the waveforms of synthetically inserted events, it seems that small magnitude events should be detected more frequently if present in the continuous section. Waveforms of a range of magnitudes (m_L 1.0 to 2.1) show clear waveforms of events at least until m_L 1.5 (Figure 4-13). The smallest events detected in the application are smaller than m_L 1.6. The waveforms of the synthetic tests in Figure 4-13 suggest that events a full magnitude unit lower than observed should be detected based on the recall performance and visual identification. We thereby suggest this is not a limit of our detection method and the Bucaramanga nest may be lacking in small magnitude earthquakes.

The Bucaramanga Nest is Deficient in Small Earthquakes

We can revise our modified Gutenberg-Richter relationship to account for these various sources of error (Figure 4-14). Even with the additional earthquakes added for deficiencies in the method, it is clear a substantial portion of small magnitude earthquakes is still absent. For example, for this distribution, we expect twice as many m_L 1.75 events than observed, over ~22,000 more magnitude 1.5 events, and ~85,000 magnitude 1.0 events.

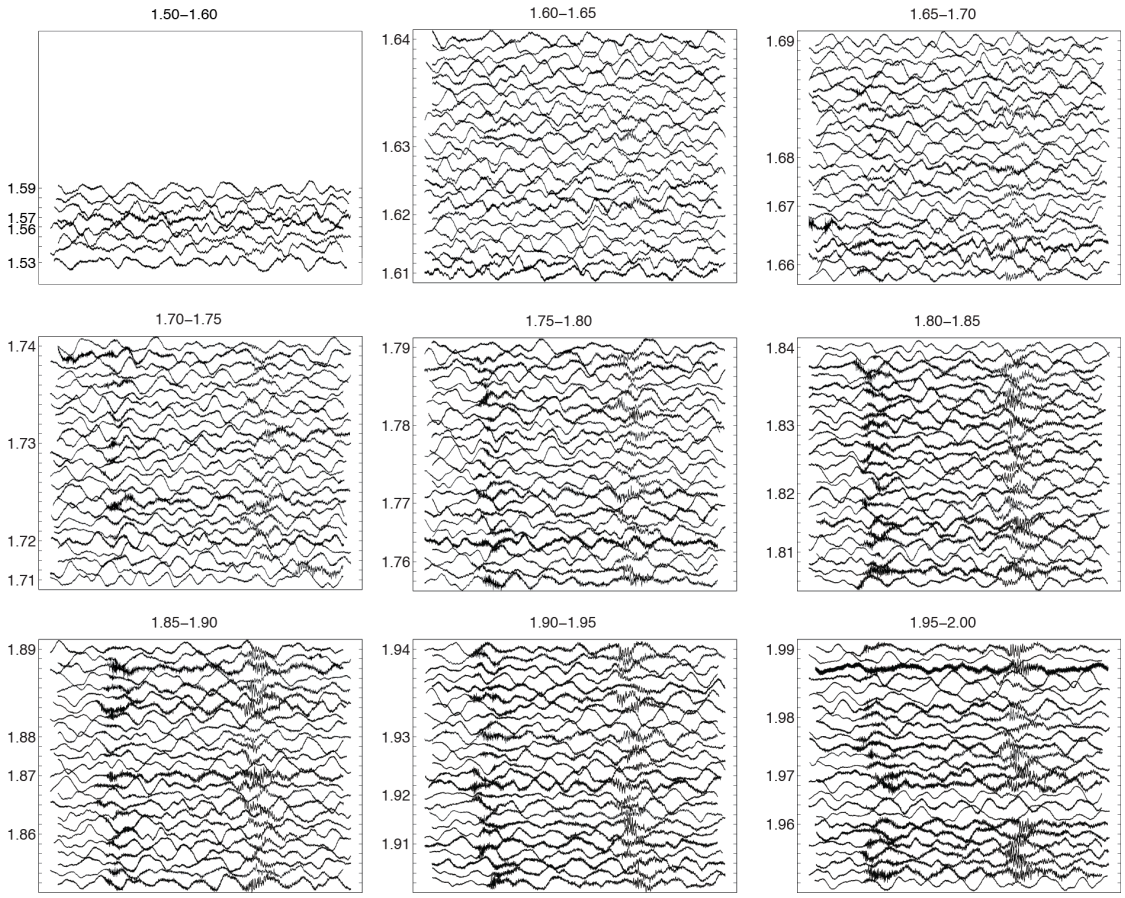

Figure 4-11. Unfiltered waveforms from Bucaramanga nest detections at various small local magnitude bins. Smaller magnitude events $m_L < 1.7$ are barely visible about the background noise threshold. The number of events per bin is limited to 25 events for clarity.

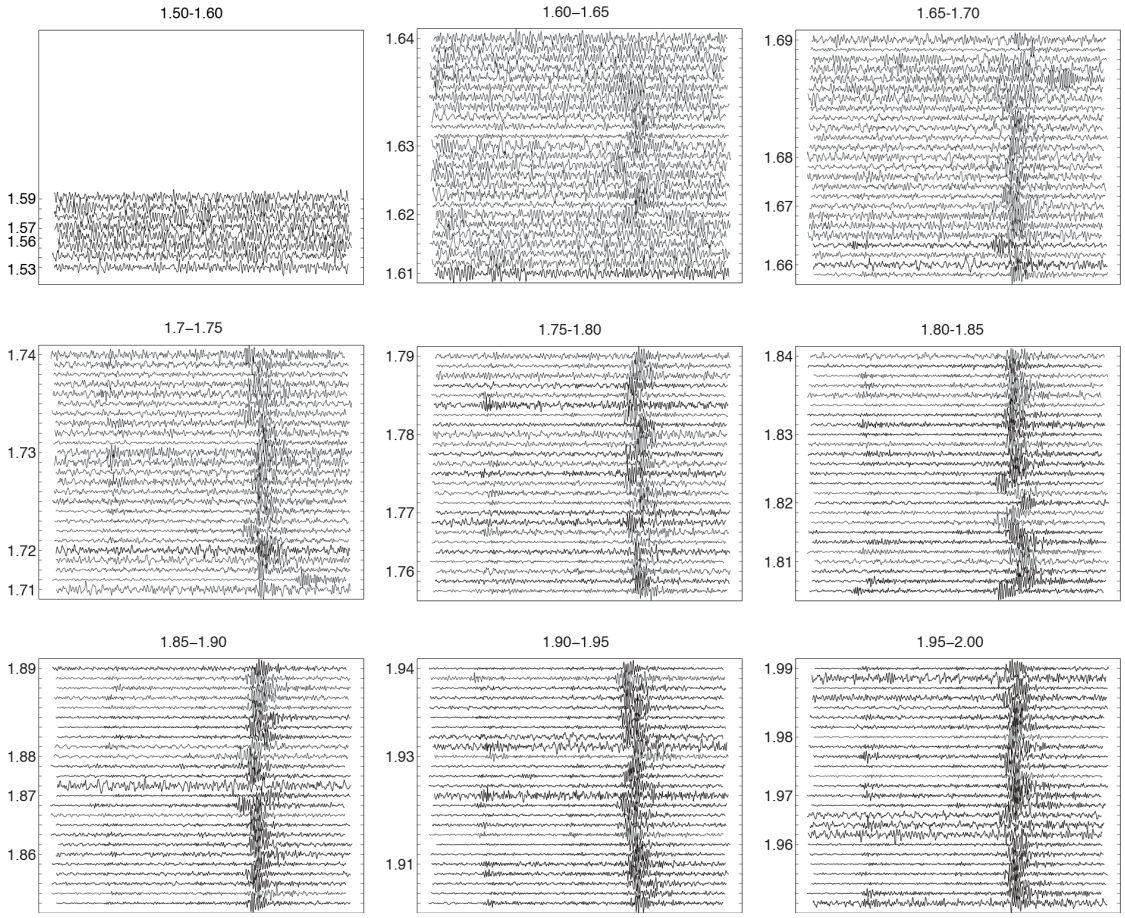

Figure 4-12. Bandpass (1-5Hz) filtered waveforms from Bucaramanga nest detections at various small local magnitude bins. Events are more clearly seen at most magnitude bins but are still difficult to detect at $m_L < 1.65$. The number of events per bin is limited to 25 events for clarity.

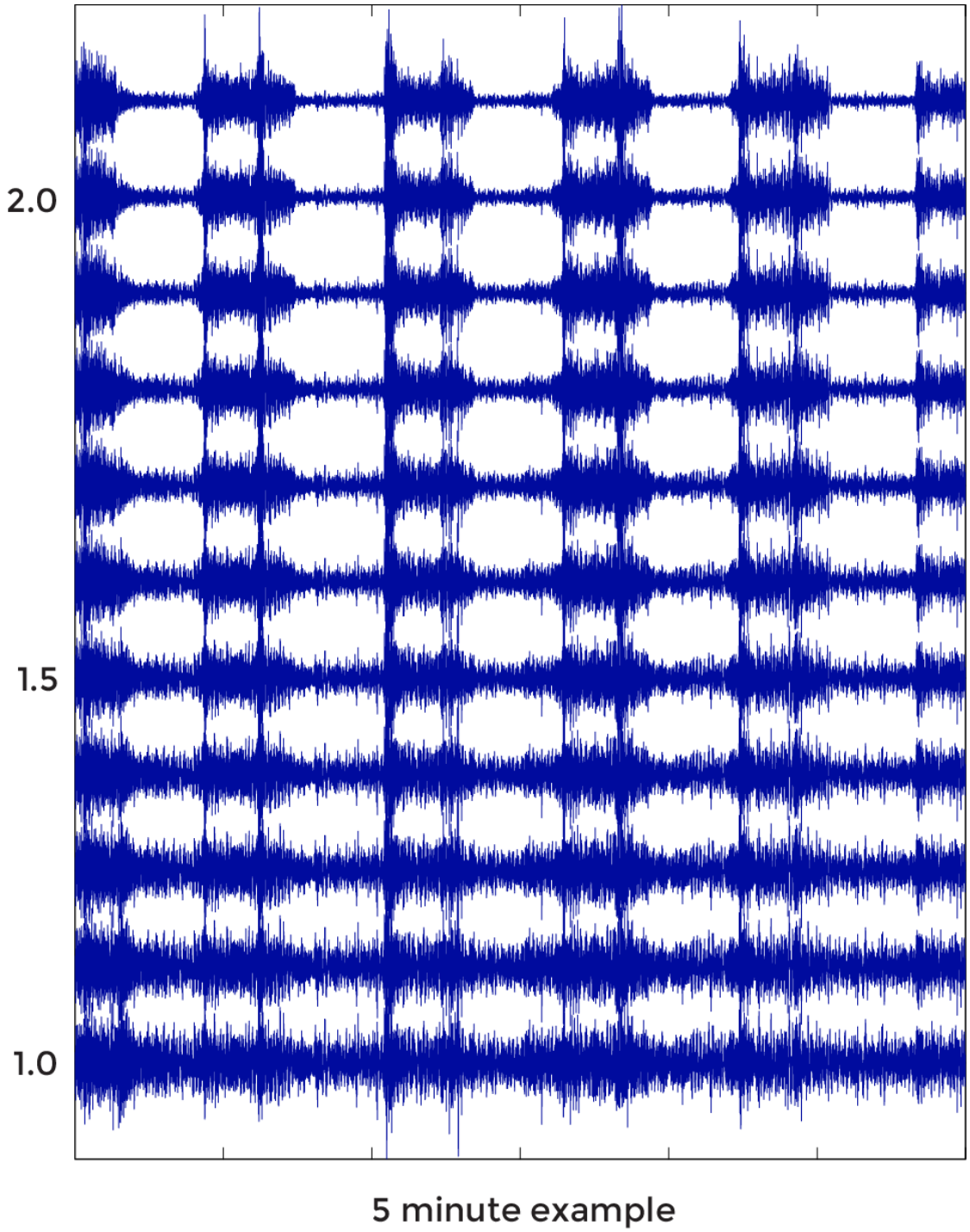

Figure 4-13. A five minute long example taken from the synthetic test sections. This shows five inserted waveforms (with their natural noise) into the continuous section on day 25, scaled according to local magnitude based on S-wave amplitude. This example suggests the detection method ought to detect smaller magnitude events than are present in the catalog, if they exist in the continuous record.

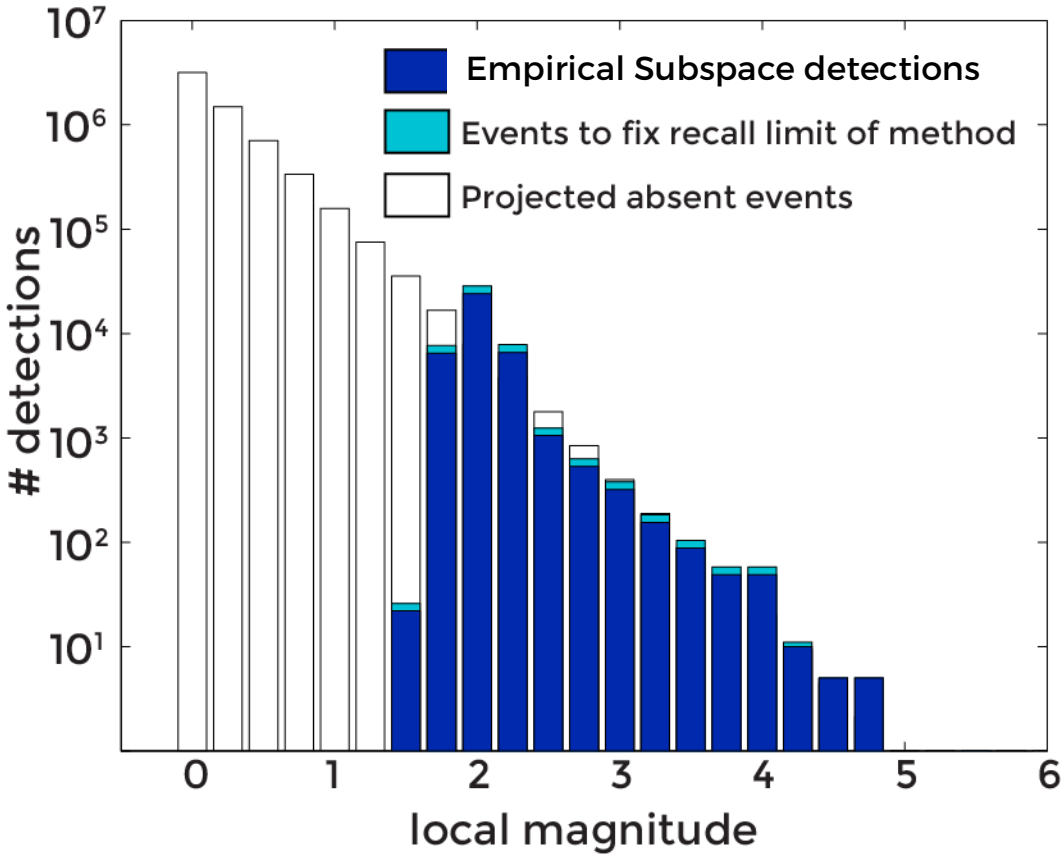

Figure 4-14. Modified GR distributions for: events detected by the empirical subspace method (dark blue), detections with compensation for limitation of the detection method as determined by the recall value for each magnitude (light blue), and the amount of expected events given a similar power law for all magnitudes (white).

Relationship between Detectability of an Event and Depth

For reasons that are not yet clear, there is a correlation between the ability of an event to be detected by a template and its depth (Figure 4-15). In general, events with greater event to station distances (deeper) ought to be more difficult to detect. This change in event detection performance does not correspond to a change in the velocity model structure within the Bucaramanga Nest.

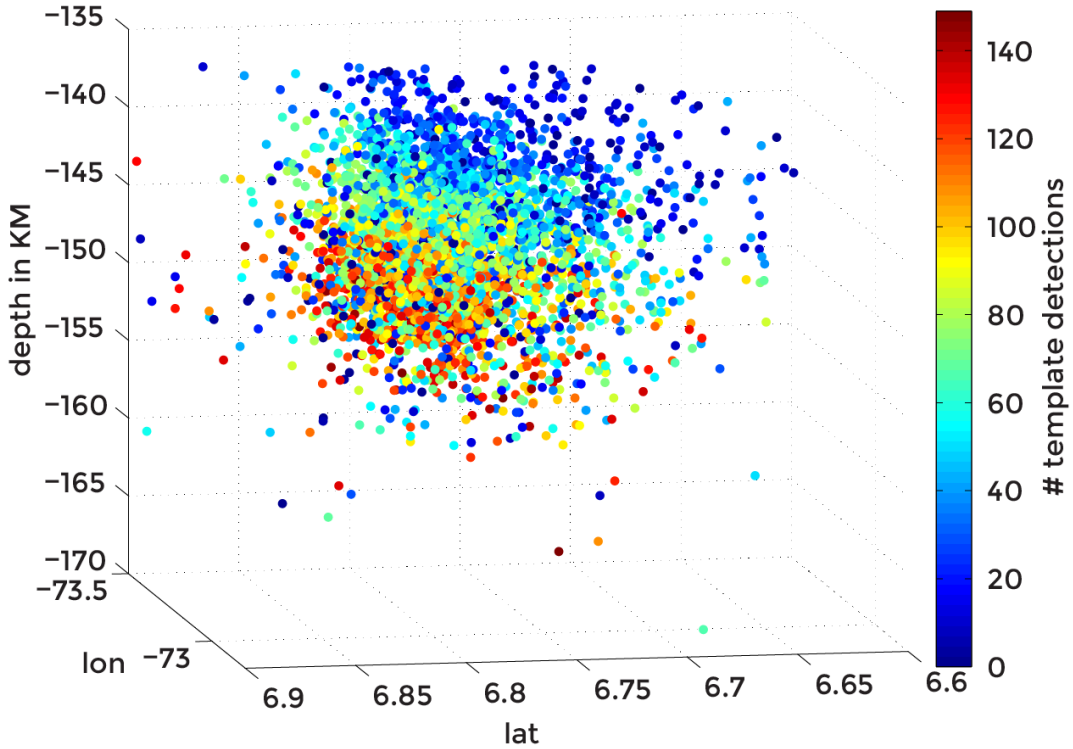

Figure 4-15. The ability of the 175 template events to detect an earthquake in the nest increases with depth. Each event is shown with its RSNC catalog location and colored by the number of templates that successfully detect it.

We test the hypothesis that deeper nest earthquakes might be more likely to repeat (Figure 4-16). We look at a subset of more shallow (<140 km) events and a set of deeper (> 145 km) events. Each group detects events of all depths, suggesting that the deeper population does not contain more repeating seismicity than the upper portion. We also look at the frequency content of a few of these subset events to see if the deeper events pass through a highly attenuating structure in the nest, and are effectively low pass filtered (Figure 4-17). Again, the results are inconclusive. If any trend is present, it is that the deep, higher performing template events have greater frequency content than their shallow counterparts.

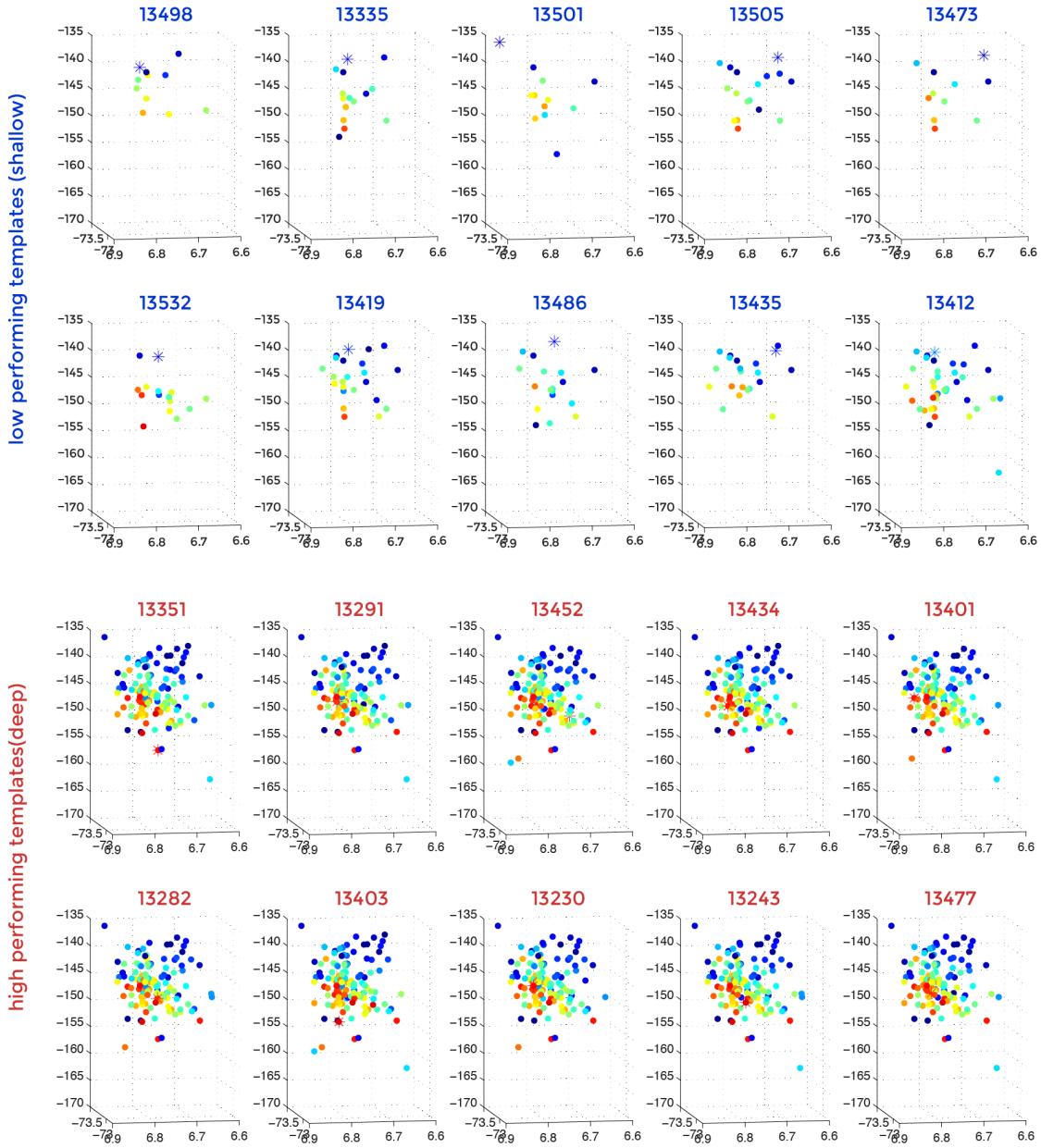

Figure 4-16. Subset populations of shallow infrequently detected events (blue, top) contrasted with deeper, frequently detected events (red, bottom). Various template events are shown with all events they detect. There is not a strong correlation between a template's depth an its ability to detect events of the same depth. Color scale is the same as in Figure 4-11.

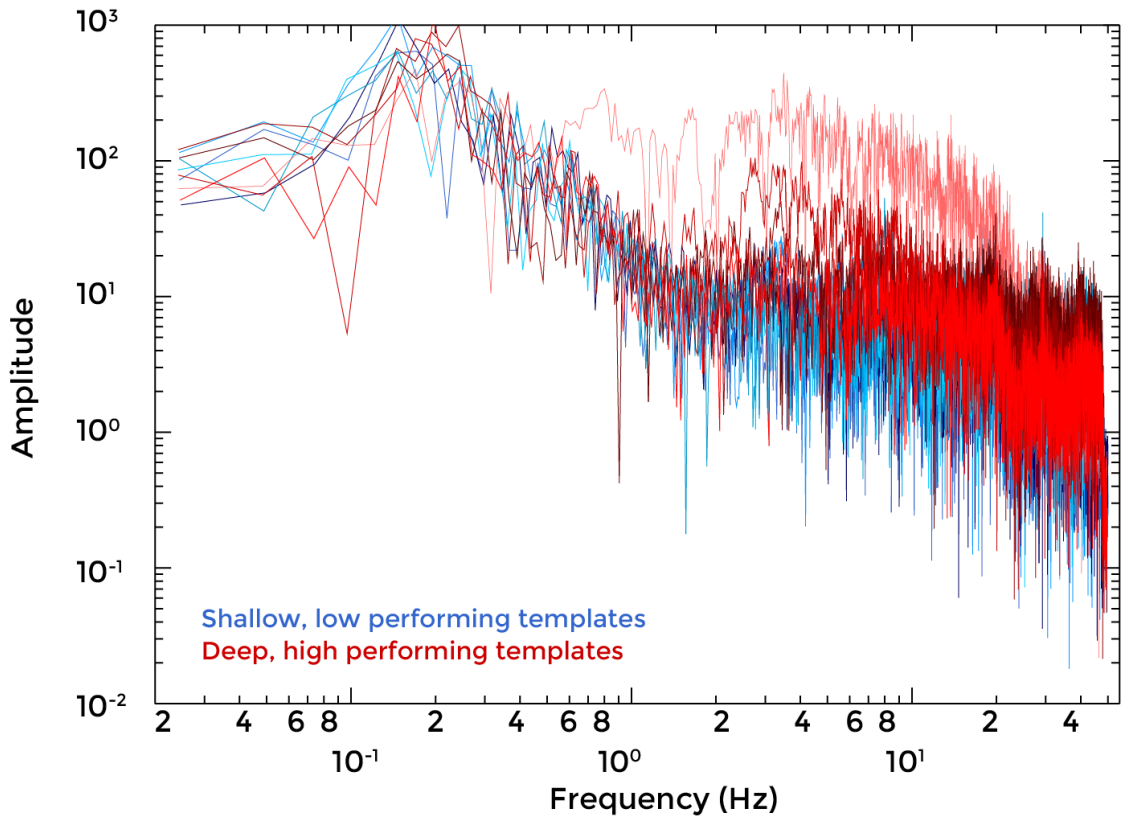

Figure 4-17. Frequency content of example events from the shallow, infrequently detected population (blues) and from the deeper, frequently detected population of seismicity (reds). There is not a strong correlation between deeper events and less high-frequency content.

Conclusions

Studies of shallow earthquakes find a power law relationship with the log of event frequency and magnitude. The falloff from this relationship is primarily limited by detection capabilities. We find through careful inspection that the Bucaramanga Nest does not produce the number of small magnitude earthquakes that is expected from a Gutenberg-Richter magnitude-frequency distribution, beyond what is resolved from testing the limitations of our detection method. A deficiency in small magnitude earthquakes might suggest an underlying failure process that requires a minimum amount of slip. Thermal shear instability failure requires a critical amount of slip for the runaway process to begin. It is possible the absence of small magnitude events is limited by the failure mechanism rather than the detection method.

References

Bachmann, C. E. (2011). *New approaches towards understanding and forecasting induced seismicity* (Doctoral dissertation). doi: 10.3929/etz-a-006715437.

Barrett, S. A. and G. C. Beroza (2014). An empirical approach to subspace detection, *Seismol. Res. Lett.*, **85**, (3), 594-600, doi: 10.1785/0220130152.

Frohlich, C. (2006), Deep Earthquakes, Cambridge Univ. Press, Cambridge.

Gutenberg, B. and C. F. Richter (1944). Frequency of earthquakes in California, *Bull. Seismol. Soc. Am.*, **34**, (4), 158-188.

Nanjo, K. Z., Schorlemmer, D., Woessner, J., Wiemer, S., and D. Giardini, (2010). Earthquake detection capability of the Swiss Seismic Network, *Geophys. J. Int.*, **181**, (3), 1713-1724, doi: 10.1111/j.1365-246X.2010.04593.x.

Schorlemmer, D. and J. Woessner (2008). Probability of detecting an earthquake, *Bull. Seismol. Soc. Am.*, **98**, (5), 2103-2117, doi: 10.1785/0120070105.

Woessner, J. and S. Wiemer, (2005). Assessing the quality of earthquake catalogues: estimating the magnitude of completeness and its uncertainty, *Bull. Seismol. Soc. Am.*, **95**, (2), 684-698, doi: 10.1785/0120040007.

Conclusions

This thesis develops new constraints from seismological observations on the mechanism of intermediate-depth earthquakes. The preponderance of my results point towards a scale-dependence of earthquake behavior that is not seen for shallow earthquakes, and is not expected for the dehydration-embrittlement mechanism. In particular, the lack of small intermediate-depth earthquakes supports the case for thermal shear instability failure because it would point to a minimum amount of slip being required to the instability to develop. This work seeks to add data from intermediate-depth earthquake nests, specifically the Bucaramanga Nest to a catalog of results from laboratory work, numerical modeling, geologic field observations and previous seismological observations.

In order to provide a complete picture of the seismicity in the Bucaramanga Nest, I have developed a new method for earthquake detection (Barrett and Beroza, 2014). This method suggests a slight modification to the existing popular method of template matching that provides additional generality to the template- earthquake search. It has been shown in both Southern California and the Bucaramanga Nest to increase detections without substantially increasing computation time. Additionally, we find it to work well in cases where the event-station distance is far, as in the case of intermediate-depth seismicity.

Within the catalog of Bucaramanga Nest seismicity I find families of repeating earthquakes. While this is an interesting observation itself, I observe that some families are nearly perfect negatives of each other, or reverse-polarity repeats. These reverse-polarity repeating earthquakes are a new observation and require a modification to existing cluster analysis methods to represent their differences. I develop a modified divisive hierarchical clustering method to cluster candidate earthquakes into their proper families by including the use of negative correlation coefficients as well as their more commonly used positive coefficients. These two distinctive populations are relocated on different structures with antithetic motion. Such a geometry can be interpreted to be a manifestation of shear failure in a region juxtaposed with ductile zones, as in boudin formation. Failure under these geologic conditions is consistent with thermal shear instability failure as it allows for a rapid failure process under ductile conditions.

When observing the entire population of earthquakes in the Bucaramanga Nest, I observe a departure from traditional Gutenberg-Richter magnitude-frequency distribution at small magnitudes beyond what can be attributed to limitations of the detection method. Through use of synthetically added earthquakes, I am able to test the performance of the empirical subspace detector and account for events that may be missed using our detection method. Even with these extra events included, we find a lack of small magnitude earthquakes in the Bucaramanga Nest. This absence of small events suggests earthquakes might require a minimum size for failure. Thermal shear instability requires a sufficient amount of slip (i.e. critical magnitude) for the runaway process to initiate.

It is known that the dehydration of hydrous minerals play a role in major subduction zone processes; however, we find the mechanism of dehydration embrittlement does not explain our findings as well a thermal shear instability failure. We find the arrangement of the opposing shear zones of the reverse polarity repeating earthquakes

fits well with a ductile shear process that is observable in outcrop (boudinage). We observe a lack of small magnitude earthquake suggests there might be insufficient slip for a runaway process to occur. If this failure occurred through dehydration embrittlement, we would might expect to observe earthquakes only in regions where dehydration reactions occur and small magnitude earthquakes to produce seismic radiation much in the way shallow earthquakes do. These earthquakes would be recorded at RSNC stations and their detection limited by methodology. We find a lack of small events even once we compensate for limits of the empirical subspace method

This thesis uses various observations of seismicity in the Bucaramanga Nest and through independent lines of evidence finds support for thermal shear instability as the failure mechanism of intermediate-depth earthquakes. Findings are consistent with previous work on the Bucaramanga Nest (e.g. Prieto et al., 2013), thermal shear instability models (e.g. John et al., 2009) and other intermediate-depth earthquake nests (e.g. Lister et al., 2008). While there is strong evidence for dehydration reactions at these depths, we find through numerous approaches the need for a thermal shear type failure. This work provides data that contributes to the knowledge of the mechanism by which intermediate-depth earthquakes failure, with an emphasis on the Bucaramanga Nest.

Appendix A:

A subset of Bucaramanga Nest earthquakes was used in Chapter 3 to assess intermediate-depth seismicity for repeating and reverse polarity earthquakes as they occur in space and time. The following table describes the basic catalog properties of these events. Group A events are colored in red, while group B events are indicated by blue Those events that do not strongly fit into one group or the other are black.

Year	Month	Day	Time	Latitude	Longitude	Depth	Event ID
2011	2	25	15:10:39	6.81	-73.13	144.3	11970
2011	2	26	3:23:53	6.80	-73.17	139.9	11985
2011	2	27	8:27:31	6.79	-73.18	139.4	12020
2011	2	28	2:41:08	6.81	-73.13	144.3	12041
2011	3	1	11:33:43	6.82	-73.18	142.2	12070
2011	3	7	17:35:17	6.82	-73.12	146.3	12212
2011	3	8	20:13:24	6.77	-73.18	132.8	12231
2011	3	16	8:38:54	6.79	-73.09	148.0	12430
2011	3	17	5:47:06	6.79	-73.15	149.3	12451
2011	3	21	14:36:33	6.81	-73.16	139.4	12560
2011	3	23	0:34:24	6.80	-73.16	145.8	12586
2011	3	28	1:24:08	6.80	-73.15	151.8	12706
2011	4	1	16:27:45	6.76	-73.16	151.2	12857
2011	4	2	17:30:08	6.81	-73.15	148.8	12898
2011	4	4	3:45:48	6.78	-73.13	139.9	12951
2011	4	4	20:56:18	6.77	-73.09	148.3	12975
2011	4	16	22:30:55	6.76	-73.12	148.6	13313
2011	4	28	2:29:24	6.80	-73.16	148.1	13608
2011	5	1	4:52:15	6.79	-73.12	152.4	13690

Year	Month	Day	Time	Latitude	Longitude	Depth	Event ID
2011	5	1	17:49:41	6.78	-73.12	146.1	13713
2011	5	2	23:55:54	6.78	-73.13	149.3	13750
2011	5	7	21:03:12	6.77	-73.11	152.5	13887
2011	5	13	15:18:25	6.78	-73.12	151.7	14122
2011	5	16	5:12:39	6.76	-73.11	141.9	14209
2011	5	18	4:13:06	6.77	-73.13	142.1	14287
2011	5	19	7:49:05	6.76	-73.12	146.5	14331
2011	5	19	12:22:32	6.77	-73.11	146.0	14338
2011	5	20	3:14:52	6.77	-73.13	141.9	14362
2011	5	20	23:18:57	6.77	-73.12	145.6	14405
2011	6	4	2:44:13	6.78	-73.10	150.1	14850
2011	6	14	17:55:15	6.79	-73.11	148.0	15165
2011	6	18	13:17:53	6.77	-73.09	142.0	15286
2011	6	22	16:51:42	6.78	-73.14	145.9	15429
2011	6	24	15:25:08	6.81	-73.14	147.5	15488
2011	6	28	9:02:07	6.78	-73.12	150.5	15646
2011	6	29	2:23:46	6.78	-73.15	150.6	15667
2011	7	6	2:23:00	6.80	-73.13	144.4	15943
2011	7	6	17:14:19	6.77	-73.12	143.5	15963
2011	7	8	16:41:37	6.77	-73.09	146.4	16023
2011	7	14	1:28:40	6.80	-73.11	145.4	16195
2011	7	28	1:58:14	6.78	-73.09	150.4	16619
2011	7	29	9:24:29	6.77	-73.10	150.5	16659
2011	8	3	21:33:56	6.78	-73.12	151.2	16847
2011	8	4	13:16:43	6.80	-73.11	150.7	16867
2011	8	8	7:12:56	6.77	-73.13	146.4	16954
2011	8	8	22:42:29	6.77	-73.11	148.2	16981
2011	8	10	1:36:36	6.74	-73.11	138.4	17015
2011	8	17	16:19:10	6.78	-73.09	142.6	17264
2011	8	20	7:39:12	6.92	-72.98	166.6	17326
2011	8	22	0:42:01	6.76	-73.11	141.0	17369
2011	8	23	16:52:05	6.82	-73.03	150.1	17417
2011	8	26	4:30:01	6.80	-73.13	151.5	17484
2011	8	26	6:23:40	6.79	-73.15	139.6	17490
2011	8	26	11:38:16	6.82	-73.10	143.0	17508
2011	8	26	12:36:25	6.80	-73.11	151.9	17510
2011	9	3	0:49:32	6.78	-73.09	139.9	17711

Year	Month	Day	Time	Latitude	Longitude	Depth	Event ID
2011	9	3	0:58:39	6.75	-73.12	148.0	17712
2011	9	5	8:21:03	6.80	-73.06	149.2	17800
2011	9	3	1:30:46	6.80	-73.06	146.4	17714
2011	9	3	1:32:55	6.77	-73.12	141.0	17715
2011	9	3	2:02:47	6.77	-73.10	144.0	17717
2011	9	5	17:12:14	6.77	-73.12	149.8	17818
2011	9	6	19:59:03	6.79	-73.11	143.7	17870
2011	9	6	19:59:16	6.79	-73.11	143.7	20
2011	9	6	20:01:35	6.75	-73.09	137.5	17871
2011	9	6	20:02:29	6.80	-73.13	147.2	17873
2011	9	6	21:34:10	6.79	-73.12	146.7	17877
2011	9	9	20:43:32	6.77	-73.11	146.9	17976
2011	9	20	16:32:40	6.79	-73.13	152.0	18336
2011	9	22	0:52:28	6.80	-73.17	141.6	18385
2011	9	27	14:10:25	6.78	-73.14	142.8	18580
2011	10	8	14:22:48	6.78	-73.16	141.3	19029
2011	10	11	20:54:53	6.79	-73.14	140.4	19149
2011	10	18	21:36:34	6.76	-73.13	152.0	19389
2011	10	20	1:11:53	6.80	-73.10	149.9	19434
2011	10	20	6:16:28	6.77	-73.11	152.6	19441
2011	10	23	8:03:28	6.82	-73.10	148.9	19542
2011	10	24	21:41:39	6.83	-73.13	144.0	19599
2011	10	26	7:26:03	6.79	-73.11	149.1	19645
2011	10	26	12:19:57	6.77	-73.14	148.6	19657
2011	10	30	1:18:25	6.82	-73.17	145.4	19800
2011	10	31	18:42:13	6.79	-73.12	152.9	19883
2011	11	7	15:55:24	6.81	-73.15	144.2	20133
2011	11	7	16:56:02	6.77	-73.10	140.0	20135
2011	11	7	17:36:32	6.77	-73.13	140.3	20136
2011	11	17	18:08:43	6.80	-73.14	146.6	20518
2011	11	21	13:34:58	6.80	-73.15	147.5	20647
2011	11	21	13:45:45	6.77	-73.13	144.6	20648
2012	2	24	3:05:43	6.77	-73.18	137.8	24536
2013	8	31	17:30:03	6.81	-73.12	164.0	2
2013	8	31	20:00:28	6.81	-73.13	155.7	3
2013	8	31	21:29:22	6.84	-73.15	147.9	9